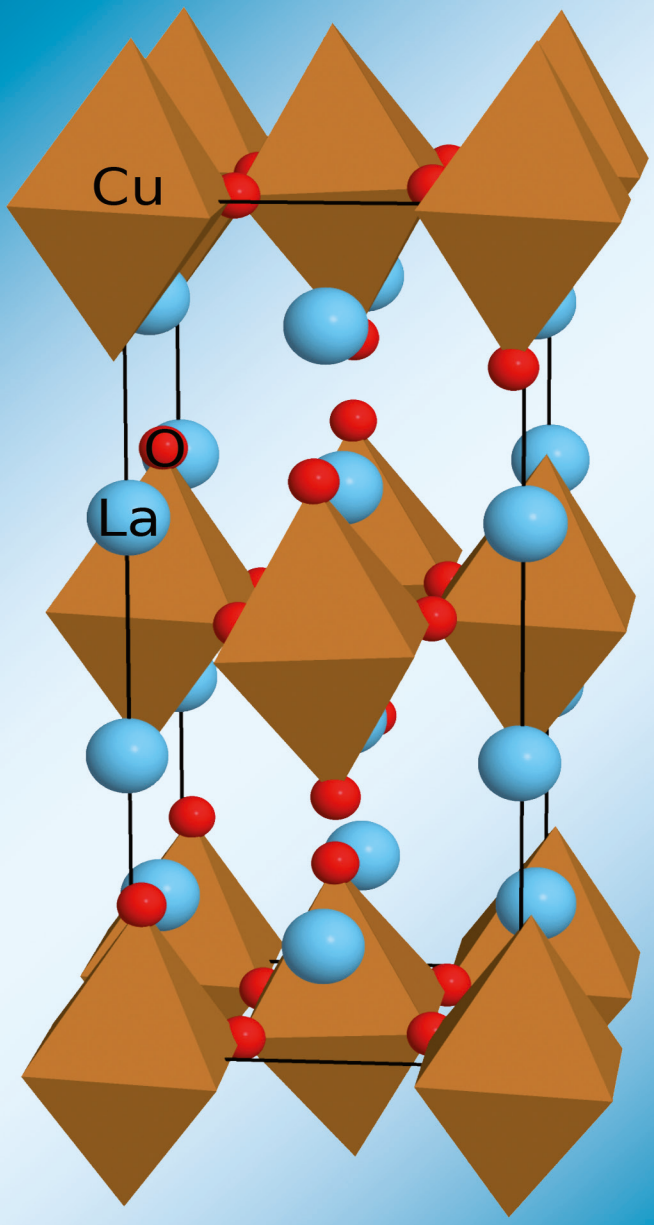


# Oxygen transport in thin oxide films at high field strength

Dieter Weber

Member of the Helmholtz Association

JÜLICH
FORSCHUNGSZENTRUM

Schriften des Forschungszentrums Jülich
Reihe Information / Information Band / Volume 33

Forschungszentrum Jülich GmbH
Peter Grünberg Institute (PGI)
Microstructure Research (PGI-5)

# Oxygen transport in thin oxide films at high field strength

Dieter Weber

Schriften des Forschungszentrums Jülich
Reihe Information / Information Band / Volume 33

ISSN 1866-1777 ISBN 978-3-89336-950-8

Bibliographic information published by the Deutsche Nationalbibliothek.
The Deutsche Nationalbibliothek lists this publication in the Deutsche Nationalbibliografie; detailed bibliographic data are available in the Internet at http://dnb.d-nb.de.

| | |
|---|---|
| Publisher and Distributor: | Forschungszentrum Jülich GmbH<br>Zentralbibliothek<br>52425 Jülich<br>Tel: +49 2461 61-5368<br>Fax: +49 2461 61-6103<br>Email: zb-publikation@fz-juelich.de<br>www.fz-juelich.de/zb |
| Cover Design: | Grafische Medien, Forschungszentrum Jülich GmbH |
| Printer: | Grafische Medien, Forschungszentrum Jülich GmbH |
| Copyright: | Forschungszentrum Jülich 2014 |

Schriften des Forschungszentrums Jülich
Reihe Information / Information, Band / Volume 33

D 82 (Diss., RWTH Aachen University, 2014)

ISSN 1866-1777
ISBN 978-3-89336-950-8

The complete volume is freely available on the Internet on the Jülicher Open Access Server (JUWEL) at www.fz-juelich.de/zb/juwel

**Abstract**

Ionic transport in nanostructures at high field strength has recently gained attention, because novel types of computer memory with potentially superior properties rely on such phenomena. The applied voltages are only moderate, but they drop over the distance of a few nanometers and lead to extreme field strengths in the MV/cm region. Such strong fields contributes significantly to the activation energy for ionic jump processes. This leads to an exponential increase of transport speed with voltage. Conventional high-temperature ionic conduction, in contrast, only relies on thermal activation for such jumps.

In this thesis, the transport of minute amounts of oxygen through a thin dielectric layer sandwiched between two thin conducting oxide electrodes was detected semi-quantitatively by measuring the conductance change of the electrodes after applying a current through the dielectric layer. The relative conductance change $\Delta G/G$ as a function of current $I$ and duration $t$ follows over several orders of magnitude a simple, empirical law of the form $\Delta G/G = CI^A t^B$ with fit parameters $C$, $A$ and $B$; $A, B \in [0, 1]$. This empirical law can be linked to a predicted exponential increase of the transport speed with voltage at high field strength. The behavior in the time domain can be explained with a spectrum of relaxation processes, similar to the relaxation of dielectrics. The influence of temperature on the transport is strong, but still much lower than expected. This contradicts a commonly used law for high-field ionic transport.

The different oxide layers are epitaxial with thicknesses between 5 and 70 nm. First large-scale test samples were fabricated using shadow masks. The general behavior of such devices was studied extensively. In an attempt to achieve quantitative results with defect-free, miniaturized devices, a lithographic manufacturing process that uses repeated steps of epitaxial deposition and structuring of the layers was developed. It employs newly developed and optimized wet chemical etching processes for the conducting electrodes. First high-quality devices could be manufactured with this process and confirmed that such devices suffer less from parasitic effects. The lithographically structured samples were made from different materials. The results from the first test samples and the lithographically structured samples are therefore not directly comparable. They do exhibit however in principle the same behavior. Further investigation of such lithographically structured samples appears promising.

**Kurzfassung**

Ionentransport in Nanostrukturen bei hoher Feldstärke ist in letzter Zeit mehr in den Fokus der Forschung gerückt, weil neuartige Speichertechnologien für Computer mit möglicherweise überlegenen Eigenschaften darauf beruhen. Die angelegten Spannungen sind moderat, aber sie fallen über eine Distanz von wenigen Nanometern ab und führen zu extremen Feldstärken im Bereich von MV/cm. Solch starke Felder tragen signifikant zur Aktivierungsenergie von ionischen Sprungprozessen bei. Dadurch steigt die Transportgeschwindigkeit exponentiell mit der Spannung an. Bei konventionelle Hochtemperatur-Ionenleitung erfolgt die Aktivierung im Kontrast dazu rein thermisch.

In dieser Arbeit wurde der Transport von kleinsten Sauerstoffmengen nach einem Strompuls durch eine dünne dielektrische Schicht, die zwischen zwei leitfähigen Oxidelektroden eingebettet war, semi-quantitativ über die Leitwertänderung dieser Elektroden untersucht. Die relative Änderung des Leitwerts $\Delta G/G$ als Funktion des Stroms $I$ und der Zeitdauer $t$ folgt über mehrere Größenordnungen einem einfachen, empirischen Gesetz der Form $\Delta G/G = CI^A t^B$ mit Fitparametern $C$, $A$ und $B$; $A, B \in [0, 1]$. Dieses empirische Gesetz kann mit einer vorhergesagten exponentiellen Beschleunigung des Transports bei hoher Feldstärke in Verbindung gebracht werden. Das zeitliche Verhalten lässt sich mit einem Spektrum von Relaxationsprozessen erklären, so ähnlich wie bei der Relaxation von Dielektrika. Der Einfluss der Temperatur auf den Transport ist groß, aber trotzdem weit geringer als erwartet. Dies widerspricht einem weit verbreiteten Gesetz für den Ionentransport bei hoher Feldstärke.

Die verschiedenen Oxidschichten sind epitaktisch mit Dicken zwischen 5 und 70 nm. Erste großflächige Testproben wurden mithilfe von Schattenmasken hergestellt. Das allgemeine Verhalten solcher Bauelemente konnte damit ausführlich untersucht werden. In einem Versuch, quantitative Ergebnisse an defektfreien, miniaturisierten Bauelementen zu erlangen, wurde ein lithografischer Herstellungsprozess mit wiederholten Schritten von epitktischer Schichtabscheidung und Strukturierung entwickelt. Dieser verwendet neu entwickelte und optimierte nasschemische Ätzprozesse für die leitfähigen Elektroden. Erste Proben konnten mit diesem Prozess in guter Qualität hergestellt werden und bestätigten, dass solche miniaturisierten Bauelemente weniger von parasitären Effekten betroffen sind. Da zunächst andere Materialien verwendet wurden, sind die Ergebnisse der beiden Probentypen nicht direkt vergleichbar. Es wurde gezeigt, dass die lithografisch hergestellten Proben ein im Prinzip ähnliches Verhalten zeigen wie die ersten Testproben. Weitere Untersuchungen an lithografisch strukturierten Proben erscheinen daher aussichtsreich.

# Contents

# List of Figures

# List of Tables

# List of Abbreviations

AFM Atomic force microscopy

BHF Ammonia-buffered hydrofluoric acid

CD Compact disc

CMOS Complementary metal–oxide–semiconductor

CMP Chemical-mechanical polishing

CPU Central processing unit

CVD Chemical vapor deposition

DC Direct current

DMSO Dimethyl sulfoxide

DRAM Dynamic random access memory

DVD Digital versatile disc

ECM Electrochemical metallization cell memory

EEPROM Electrically erasable programmable read-only memory

FET Field-effect transistor

GPIB General purpose interface bus

GUI Graphical user interface

ICP-OES Inductively coupled plasma optical emission spectrometry

ICS Institute of complex systems, Forschungszentrum Jülich

IKP Institute of nuclear physics, Forschungszentrum Jülich

IPC Institute of Physical Chemistry, RWTH Aachen university

JCNS Jülich Center for Neutron Science, Forschungszentrum Jülich

JSON JavaScript object notation

LAO $LaAlO_3$

LCO $La_2CuO_{4\pm x}$

LSGM $(La, Sr)(Ga, Mg)O_{3-x}$

LSMO $(La, Sr)MnO_3$

MIEC Mixed ionic-electronic conductors

MPI Max Planck Institute

NGO $NdGaO_3$

PCB Printed circuit board

PCM Phase-change memory

PGI Peter Grünberg Institute, Forschungszentrum Jülich

PMMA Poly(methyl methacrylate)

QCM Quartz crystal microbalance

RF Radio frequency

RHEED Reflection high-energy electron diffraction

SCPI Standard commands for programmable instruments

SOFC Solid oxide fuel cell

Sr:LCO $La_{1.85}Sr_{0.15}CuO_{4\pm x}$

SRAM Static random access memory

SRO $SrRuO_3$

SSDs Solid-state discs

STO $SrTiO_3$

TCM Thermochemical memory

TEM Transmission electron microscopy

TMAH Tetramethylammonium hydroxide

UHV Ultra high vacuum

USB Universal serial bus

UV Ultraviolet

VCM Valency change memory

XML Extensible markup language

XRD X-ray diffraction

XRR X-ray reflectivity

YBCO $YBa_2Cu_3O_{7-x}$

YSZ Y-doped $ZrO_2$

ZB Central library, Forschungszentrum Jülich

ZCH Central department for chemical analysis

ZEA Central institute for engineering, electronics and analytics, FZ Jülich

# Chapter 1

# Introduction

This work started with the goal to develop a three-terminal ionic switching device that is usable for memory applications. It turned out that the switching speed and switching amplitude of prototypes were way too low and that the devices did not retain their state for long enough. The focus was therefore moved to investigate the ionic transport in such devices on a more fundamental level, as explained in Section 2.6.

In principle, the devices that were investigated here are crossbar structures where a nanometer-thick oxide dielectric is sandwiched between two crossed electronically conducting oxide electrodes. They are described in detail in Section 3.1. When a voltage is applied between the two electrodes, a very strong electric field builds up inside the dielectric. Oxygen anions are transported in this field from one electrode to the other through the dielectric, in parallel to a much larger electronic current. This oxygen transport changes the oxygen content of the electrodes. The in-plane electronic conductance of the electrodes therefore changes due to the doping effect of oxygen. This change can easily be detected to a high precision with simple electrical measurements. The measured electronic conductance change of the electrodes is in first approximation proportional to the amount of transported oxygen. This allows to detect and investigate low-level oxygen transport through such ultra-thin oxide films semi-quantitatively[1].

Recently the interest in such systems has increased, because valency change memory (VCM) [2] and electrochemical metallization cell memory (ECM) [3] operate with high-field ionic transport in nanostructures[4]. The following quote on redox-based resistive switching memory is taken from the International Roadmap for Semiconductor Technology 2011 [5]:

> Many details of the mechanism of the reported phenomena are still unknown. Developing an understanding of the physical mechanisms governing switching of the redox memory is a key challenge for this technology.

Some theory has already been established [6, 7], but systematic experimental data on room-temperature ionic transport in nanometer-thick epitaxial thin film heterostructures at high field strength is hardly available. Furthermore, strong electronic and ionic interface effects should be expected in such dimensions [8]. Compared to

"conventional" solid-state ionic transport, like in fuel cells, certain batteries and some gas sensors, this is still a niche subject.

The transport of ions is accelerated exponentially when the electric field is so strong that it significantly lowers the energetic barrier for ionic jump processes [4, 6]. Experimental data on ionic transport at medium field strength in certain glasses and high-field ionic transport in anodic passivating films can be found in the literature (for example [9–11]). Such a field strength can be achieved with comparatively low absolute voltage if the layers are only nanometer-thick.

The amount of transported ionic species is so low and dimensions are so small that it can be difficult to detect the concentration changes directly. Especially oxygen is problematic, because the oxygen content of materials is easily altered, for example during argon ion milling for transmission electron microscopy (TEM) specimen preparation[1]. The necessary concentration change for physical effects is furthermore low compared to the total oxygen content of oxide materials. The technique described here can fill this niche, because very small changes in oxygen content can be detected non-destructively. Sample preparation is however difficult and time-consuming.

A huge technology background exists for semiconductor device fabrication with conventional materials, such as silicon or GaAs. Much less technology is available for functional oxides. A method to chemically etch certain resistant oxides selectively and a process to build up high-quality epitaxial oxide thin film structures with repeated deposition and lithographic patterning steps were developed in order to obtain samples of sufficient quality. The samples are among the most complex epitaxial oxide heterostructures that have been built to date. The general chemistry of oxides and fundamentals of chemical etching are introduced in Section 2.4. The etching protocols are described in Section 4.5.

Measurement data, software and designs are included in electronic form with this thesis or are available on request. Patent applications [12, 13] have been filed for some of the concepts and methods, and the results have partly been presented at conferences and published in scientific journals [1, 14].

## 1.1 Ionic three-terminal devices

Three-terminal devices where a gate controls the properties of a channel via ionic transport in and out of the channel region have been described a few times in literature, but are far less common than two-terminal devices, at least in the area of resistive switching. Ramesham et al. developed a solid-state device where the channel resistance can be changed by applying a gate voltage and moving ions in and out of the channel [15]. They assume that $OH^-$ is the mobile ion. The devices consist of rather thick films and need a high switching voltage for that reason. The device was proposed for artificial neuronal networks, but did not gain much attention. A device with a metallic channel based on ECM has been demonstrated by Sakamoto *et al.* [16] and Hasegawa *et al.* [17]. Xie et al. [18] presented a similar device with a liquid electrolyte. Thiel et al. [19] could tune the properties of a conducting oxide

[1] Several typical causes of oxygen loss come together in TEM specimen preparation: Vacuum environment, ion bombardment, very low film thickness, electrical charging, and moderate heating caused by the ion bombardment.

interface with a strong back gate voltage. Their time constants are in agreement with ionic transport processes.

Electrolytes are used as a gate for field-effect devices in many cases. Ion-sensitive field-effect transistors (FETs) are an example for this. A FET made of $SrTiO_3$ with a solid-state electrolyte as the gate has been demonstrated by Ohta [20].

Ionically doped transistors manufactured from organic semiconductors were patented by Armgath, Kugler *et al.* [21, 22]. This group demonstrated a humidity sensor based on the concept [23].

Combining ionic and electronic effects seems to be particularly easy for organic semiconductors: many publications on similar devices and concepts are available. For inorganic systems this is far less common. The low ion mobility at room temperature in most inorganic ionic conductors is the limiting factor. Superionic conductors like $(Rb, Ag)I$ are an exception from this and in principle it should be possible to build such devices with them.

## 1.2 Ionic transport at high field strength

Ionic transport in this regime occurs during anodization of certain metals like aluminum [10], generally in thin passive films on metals [11], during dielectric relaxation [24] or degradation [25–27] of dielectrics, and in other nanoionic systems, like previously mentioned memristive devices [3, 4]. An exponential decrease of lifetime with applied field strength and an Arrhenius-type temperature dependence was observed for CMOS gate dielectric degradation by Xu *et al.* [28]. Such a behavior is in perfect agreement with field-accelerated ionic transport (Section 2.5). Similar results were obtained by Lu *et al.* [29]. Certain glasses also show an exponential increase of transport with electrical field [30]. A solid oxide fuel cell (SOFC) can perhaps reach into this regime once the layers are only a few nanometer thick.

## 1.3 Distinction from other similar devices and measurement types

The method to study oxygen transport described here partially resembles a number of established methods and devices. The main similarities and differences will be lined out in the following sections.

### 1.3.1 FETs

FETs have a very similar structure (compare Section 3.1) and the operation principle is somewhat related: The carrier concentration in a thin channel layer is modulated with an electric field. In typical devices for practical application, the carrier density is actually inverted, that means for example that a weakly p-conducting channel is turned into an n-type conductor by a strong electric field. This can give a very high switching amplitude of the channel conductance by creating or removing two anti-parallel p-n junctions between source and drain. A weak field effect can be observed just from the modulation of carrier density: The higher the carrier density, the higher is the conductivity (see also Section 2.2). This effect is universal to all

electronic conductors and was also observed in one case for the devices in this thesis as a side effect. Later it was avoided by carefully discharging the devices before measurements.

The field effect is volatile: It follows almost instantaneously the applied gate voltage because electronic carriers are transported in and out of the channel region rapidly. In the devices described in this work, the carrier density in the channel is modulated as well with a gate electrode, which causes a measurable change of channel conductance. But the carrier density is not changed with the field effect, but by moving oxygen anions that act as dopants in and out of the channel region. The effect is therefore much slower (ionic transport compared to electronic transport) and not volatile: Without a gate voltage, the dopants mostly stay in place.

### 1.3.2 Polarization measurements with partially blocking electrodes

These types of measurements are used to investigate ionic and electronic currents in mixed ionic-electronic conductors. They work by applying electrodes to the material that are selectively blocking or reversible for electronic and/or ionic species. The current as a function of time with a constant applied voltage is measured. In the beginning of the experiment, the current will be a mixed ionic and electronic current. Over time, a counter potential of the blocked specie(s) will build up on the blocking electrode(s) and oppose this partial current flow. If the applied voltage is lower than the stability window of the material, the blocked current will stop at some point and the remaining current in the steady state is purely of the non-blocked species. If the applied voltage exceeds the stability window of the material, it can decompose. A more detailed description and mathematical treatment of such methods can be found in [8].

This method only makes sense if the ionic current is not small compared to the electronic current. It also relies on equilibration, i.e. on sufficiently fast ionic transport at low voltage. The samples are typically macroscopic, that means with thicknesses in the micrometer to centimeter region.

In this work, the electrodes are non-blocking, but have a much higher electronic partial conductivity than the dielectric. This means that ionic species are transported through the dielectric and enrich or deplete inside the electrodes, not in the dielectric itself like in the case of blocking electrodes. The ionic current is very small compared to the electronic current (Section 6.3). Furthermore, the applied voltages typically exceed the stability window by far, which means that only the kinetics limit the transport. That's why the devices degrade after too intense writing (Fig. 5.17). The devices here have layer thicknesses in the nanometer range, which allows to study transport at extremely high field strength. The ionic transport is not measured directly as a current, but only the effect of transport on the electrode conductance is detected.

### 1.3.3 Conductivity relaxation

This method is used to study the exchange kinetics of a species between a thin film and a surrounding medium. It is necessary that a change of the chemical potential of the exchanged species alters the electronic conductivity of the thin film. This is the case for oxygen in many oxides, because oxygen acts as a p-type dopant.

The conductivity of the thin film is measured continuously. The thin film is first equilibrated to a specific chemical potential by exposing it to a suitable medium (usually a gas atmosphere with defined oxygen partial pressure) for a sufficiently long time to be very close to equilibrium. Then, the chemical potential of the species of interest is changed abruptly in the surrounding medium. The thin film will consequently take up or release this species until the chemical potentials are equilibrated again. This induces a measurable change of conductivity. By studying the conductivity change as a function of time, one can learn about the exchange kinetics and transport speed within the thin film. Such information is very important for certain sensors and for fuel cells. An example for such measurements can be found in [31].

The method presented in this thesis is in principle similar, because here the change in electrical conductivity is used as well to detect a concentration change. But here, the change is induced by applying a gate voltage through a dielectric. Therefore, the solid-state transport at very high electrical field strength can be studied. This is not possible with the traditional conductivity relaxation.

### 1.3.4 Electrochemical loading

Oxides like $La_2CuO_{4\pm x}$ (LCO) can be loaded with oxygen by anodic oxidation, for example in a KOH solution [32–35]. This dopes the film and thus increases the conductivity. The process is irreversible: Decreasing the oxygen content is not possible with this method, at least in the case of LCO.

Electrochemical loading has some similarity to the work in this thesis, because an electronically insulating and ionically conducting electrolyte is used to insert oxygen into a thin conducting oxide film electrochemically. Here, however, an ultra-thin solid-state "electrolyte" (called dielectric in this work) is used. This allows to study oxygen transport in structures that are more related to redox memory cells than electrochemical cells with a liquid electrolyte. Furthermore, the process here is reversible, that means both loading and unloading are possible.

# Chapter 2

# Background

## 2.1 Metals, insulators, ionic conductors, semiconductors

Materials are generally grouped into four categories regarding their transport properties: Metals, which are good electronic conductors; insulators which do not conduct electrical current; ionic conductors where the current is carried by mobile ions and not electrons; and semiconductors that show more complex electronic transport properties. The definitions are however not as clear as it seems: Different disciplines group the materials in different ways, so a materials could for example be called a semiconductor or an insulator depending on the context. This thesis crosses several different fields of study. In order to avoid misunderstandings, a few common definitions are presented in the following and categories that are useful in the context of this thesis are defined.

### Magnetic materials, electronic correlation

The materials are grouped only into metals and insulators. *Metals* have a finite density of states at the Fermi level, and the electrons at the Fermi level are delocalized ("Fermi liquid"). *Insulators* have no states at the Fermi level, i.e. they have a bandgap. *Semiconductors* are also insulators in that sense, but they have a "relatively low" bandgap. The electronic transport properties are not relevant: For the magnetic properties it is only interesting which electronic states exist and how they are populated resp. how they interact and order. Insulators in the context of magnetic materials often have a sizable electronic conductivity, at least at room temperature.

### Conventional electronic and ionic transport in bulk materials

The definitions are mostly phenomenological. *Insulators* do not conduct electrical current. *Metals* conduct only electronically and are good conductors at low temperature. Their conductivity decreases with increasing temperature. *Ionic conductors* have prominent conductivity at the relevant temperature range for a given application, and the current is predominantly carried by ions. They usually have a higher conductivity at higher temperature. *Semiconductors* are "poor conductors" for electrons and their conductivity increases with temperature. Mixed ionic and electronic conductors can

carry both an ionic and an electronic current. These definitions are commonly used in research on batteries or fuel cells.

### Semiconductor devices

*Metals* have a very high density of mobile electrons in the range of one electron per atom in delocalized states at the Fermi level. *Semiconductors* naturally have a (very) low number of mobile electrons in delocalized electronic states, but the states can be populated by elevated temperature, doping, injecting currents or applying electrical fields. The electrons in these states have a high mobility. *Insulators* have no mobile electronic states that can in practice be populated with carriers. Materials with small, but non-zero carrier concentration and low carrier mobility don't have an application. They could maybe be called "poor insulators".

### Complex electronic transport and ordering phenomena

Examples would be research into superconductors or multiferroics. The simple band model does not apply well to such materials. Terms like metal, semiconductor or insulator fail to capture the complexity of the involved phenomena. The full, three-dimensional electronic and also ionic structure of these materials has to be considered. LCO would be an example material for a high-temperature superconductor that has a layered structure and therefore an anisotropic electronic and ionic behavior. This is now for many years an active field of research and no conclusive theory has been established yet. A full solution of the Schrödinger equation with both electronic and nuclear degrees of freedom for larger blocks of material, i.e. many electrons and nuclei, could capture the complex electronic and phononic interactions, but that is still out of reach due to the computational complexity.

### This thesis: Ionic and electronic transport on the nanoscale

It turned out that the devices here behave as semiconductor heterostructures from an electronic point of view. Some materials are as well ionic conductors under the right conditions. Nanometer-thick films of some materials that are conventionally regarded as insulators, such as $SrTiO_3$ (STO), can exhibit semiconducting behavior. These terms are used within this thesis:

**Noble metal:** The material has a high work function and a high density of states at the Fermi level. It does therefore form ohmic contacts with all other metals and with p-type semiconductors. It forms Schottky barriers with n-type semiconductors. Examples: Ag, Au, Pt, $SrRuO_3$ (SRO)

**Base metal:** Has a low work function and a high density of states at the Fermi level. It does therefore form ohmic contacts with all other metals and n-type semiconductors. It forms Schottky barriers with p-type semiconductors. Examples: Ti, Al, In, Cr

**Narrow-bandgap semiconductor:** Has no density of states at the Fermi level in pure form, but sizable electronic conductivity at room temperature due to impurities or thermal excitation without specific doping. Forms Schottky junctions or p-n junctions. Examples: LCO

**Wide-bandgap semiconductor:** Has no density of states at the Fermi level and virtually no electronic conductivity if undoped. It can however be made conducting by doping, field effect [20] or carrier injection. The mobility is high and it forms Schottky junctions or p-n junctions. Examples: STO

**Insulator:** Cannot be turned into an electronic conductor by doping or carrier injection. Electronic carriers can only pass by tunneling or low-level defect hopping mechanisms. The mobility is very low. Examples: $LaAlO_3$ (LAO), $SiO_2$

**Ionic conductor:** Exhibits non-destructive mass transport under the influence of an electric field or generally a gradient of electrochemical potential of a mobile ionic species. In the context of this thesis, the field can be very strong and the transport can be very slow or only transient compared to a parallel electronic current. Examples: LCO, STO, $(La, Sr)(Ga, Mg)O_{3-x}$ (LSGM)

## 2.2 Conductivity change of semiconductors

The conductivity $\sigma$ of all kinds of conductors can be expressed as

$$\sigma = \sum_i n_i |q_i| \mu_i, \tag{2.1}$$

with $i$ enumerating the different kinds of charge carriers present, $n$ being the charge carrier density, $q$ the charge of one carrier and $\mu_i$ the mobility. In many cases the electrical conductivity is dominated by one kind of carrier, like electrons or holes.

The conductivity of semiconductors can be influenced by changing the mobility or the carrier density, as the charge of carriers is fixed. In Table 2.1, an overview over different mechanisms is given, along with typical time scales for LCO as an example.

Changes in oxygen stoichiometry will probably not only change the carrier density via the doping effect, but can also affect the mobility, perhaps destroy domains of oxygen sublattice order [33, 37], change the lattice constant, or even trigger phase transitions.

## 2.3 Functional oxides

Oxides and oxide nanostructures and interfaces have recently gained a lot of attention from solid state physicists and materials scientists. They lie somewhere between ionic crystals and covalently bonded semiconductors, depending on the partners involved. They combine an unusual wealth of physical and chemical phenomena that cross the boundaries between traditional scientific and engineering disciplines. This is only a short and incomplete list:

- Metallic conduction, for example $(La, Sr)MnO_3$ (LSMO) and SRO.
- Ferromagnetism and other, sometimes exotic, forms of spin ordering, for example LSMO.
- Semiconductor behavior, for example Nb-doped STO and $TiO_2$.

Table 2.1: Influences on electronic carrier mobility and density

| Change | Influence | Time scale in LCO | Magnitude in LCO | Description |
|---|---|---|---|---|
| Increasing temperature | Lowers mobility. | Depends on power density and thermal conductivity, nanoseconds to seconds range, also changes of ambient temperature. | About $-0.002K^{-1}$. | Increased temperature leads to thermal disorder of lattice atoms and therefore increased scattering. |
| | Increases carrier density. | | About $0.02K^{-1}$. | The carrier density of intrinsic semiconductors increases exponentially with temperature. There can be several "sources" of carriers present like differnt types of dopant atoms, that have different activation energies and lead to more complex behavior. |
| Additional dopants | Lower mobility. | Depends on diffusion constants, depending on temperature. | Can be huge, depends on the dopant [36]. | Dopants disturb the regular lattice and lead to increased scattering. It can also shift and localize electronic states [36]. Doping can be substitutional or intercalated, like oxygen in LCO. |
| | Usually increase carrier density. | | Many orders of magnitude. | n-type and p-type dopants cancel out each other: p-type doping of an n-type semiconductor lowers carrier density, for example. The dopants need to be ionized, which depends on temperature. Each dopant atom brings a characteristic amount of charge carriers. |
| Stoichiometry changes | Decrease mobility. | Similar to substitutional dopants. | Limited by material stability. | Crystal imperfections increase scattering. |
| | Usually increase carrier density. | | | Similar to substitutional dopants. |
| Isovalent substitution | Decrease mobility. | Similar to substitutional dopants. | Depends on the dopant, can be huge [36]. | Crystal imperfections increase scattering or change electronic structure [36]. |
| Electric field | Alters carrier density. | Picoseconds to nanoseconds. | Percent range unless combined with other effects, like in FET. | Electrostatic attraction or repulsion of charge carriers, known as field effect. |
| Strain | Alters mobility. | Usually does not change over time, exception: Strain gauges etc. | No data found. | Strain alters the band structure anisotropically and can modify mobility, at least in the case of silicon. |
| Interface states | Decrease mobility. | Reactions with ambient, interdiffusion. | Can be a lot in thin films. | Increased scattering. |
| Ordering, superstructure formation | Increase mobility. | Seconds [33] to hours or months [37], depends also on temperature. | No data found. | Less scattering. |
| Phase transition | Everything | Sound velocity (martensitic transformation) to very slow (chemical reactions, precipitation of impurities). | Complete change of properties. | It becomes a completely new material. |

- High-temperature superconductivity, for example Sr-doped LCO and $YBa_2Cu_3O_{7-x}$ (YBCO) .
- Fast oxygen anion conduction, for example LSGM.
- Proton conduction, for example $Ba(Y, Zr)O_{3-x}$.
- Ferroelectricity and other unusual dielectric behavior, for example $Pb(Zr, Ti)O_3$ or STO.

From this list it is already apparent that many oxides can exhibit several phenomena at once. Often the properties can be modulated by doping, which introduces ionic or electronic point defects. Many oxides also tolerate off-stoichiometry of some or all the components in a wide range without precipitation of secondary phases if they are prepared in the form of epitaxial thin films under the right conditions. This often corresponds to a heavy doping of the film and can alter the film properties. The low cation diffusivity in the bulk at the typical deposition temperature and the high nucleation barrier for new phases in single-crystal systems stabilize metastable states. Epitaxial strain from a lattice mismatch between single-crystal substrate and epitaxial thin film can also modulate properties. Strain can have a particularly strong influence on the ferroelectric behavior of oxides [38].

Oxygen as the defining component of oxides acts as a p-type dopant in excess, and n-type dopant in case of deficiency. It is at least to some degree mobile at elevated temperature and can be exchanged between the material and a gas atmosphere, or between adjacent layers. At room temperature, it is (largely) immobile, but can be "activated" by very strong electrical fields that contribute to the activation energy of ionic jump processes. Many oxides show a prominent transition in electronic properties when the oxygen partial pressure is varied[1], from n-type conduction under reducing conditions, over intrinsic behavior at intermediate partial pressure, to p-type conduction under oxidizing conditions. The partial pressure range where this occurs depends strongly on the chemical properties of the oxide. Some are easily oxidized, like LCO, because they can accommodate the excess anions in interstitial lattice sites with comparatively low energy and the holes in the valence band because of the material's low bandgap. Others are quite easily reduced, like stoichiometric STO: It can accommodate oxygen vacancies as well as conduction band electrons.

The effect of doping on an oxide depends on the interaction of dopant and material. In general, it can be understood in the context of defect chemistry and thermodynamics. The book "Festkörper – Fehler und Funktion" by Joachim Maier [8] treats this subject extensively. This chapter is partly based on this book. "Defect" refers to a deviation from a hypothetical state that is defined as "perfect". The Schottky notation for defects follows this definition. The concept of chemical reactions and chemical equilibrium can be extended to defects that are defined relative to a perfect crystal, just like chemical species solved in water at a low concentration. The perfect crystal corresponds to the solvent in this picture. Mixed oxides can be so flexible in their composition that it is possible to define different "perfect" states for the same material. LSMO is one such example: La and Sr are completely miscible, and over the range of mixing ratios a complex electronic and structural, temperature-dependent

[1]The partial pressure can be varied through changing the actual oxygen pressure, by mixing oxygen with an inert gas, by chemical reaction equilibria to achieve very low partial pressures, or by electrochemical methods.

phase diagram of different spin ordering and electronic conduction is traversed [39]. It is now possible to define $SrMnO_3$, $LaMnO_3$ or, for example, $La_{2/3}Sr_{1/3}MnO_3$ as "perfect". Which one is best to choose depends on the circumstances.

Charge neutrality has to be preserved in bulk systems, that means all charged defects have to be balanced by other charged defects. These balancing defects can be ionic (oxygen vacancies or interstitials, cation vacancies or interstitials, or cations of different valence) or electronic (electrons or holes). The ratio between the different cations is usually defined upon growth, because they are usually not exchanged with the environment. It is however possible that secondary phases with different composition can accommodate stoichiometric differences. This is often unwanted, but is used to an advantage in YBCO [40]. Oxygen is in contrast to cations exchanged with the environment under typical growth conditions. In some materials, it is therefore possible to introduce a big amount of oxygen vacancies by doping. The most prominent example is Y-doped $ZrO_2$ (YSZ), where negatively charged $Y|Zr|^{'}$ defects are balanced with positively charged $|O|^{\cdot\cdot}$ defects. Which defect type is finally balancing how much of the charges depends heavily on the different defect's free enthalpy of formation. Seemingly small differences in the free enthalpy of formation can lead to huge differences in concentration due to the exponential nature of the thermodynamic laws involved, which strongly favors defects with lower free enthalpy of formation. More details can be found in [8].

Charge neutrality can locally be violated around interfaces or other extended defects. It can be thermodynamically favorable for charged defects to cross an interface or "adsorb" to an extended defect and form a space-charge region. Such effects are well-known both for the case of mobile electronic carriers (p-n junctions) or ionic carriers (electrochemical double layer). In oxide interfaces, both are possible and probably a complex ionic-electronic space charge region can be formed under some circumstances [41]. Domain walls in ferroelectric materials can be conducting [42] when the spontaneous polarization of the material is compensated by free electronic charge carriers.

Coupling effects from mobile electronic and mobile ionic defects are known for semiconducting polymers, where the diffusion of counterions destabilizes p-n junctions [43]. Rectifying ionic transport is also thinkable. It has been shown already experimentally for cell membranes and can be explained in close analogy to semiconductor junctions by fixed charges and mobile counterions [44]. This is probably also applicable for certain types of oxygen anion conductors: If an interstitial oxygen anion conductor is in contact with a vacancy oxygen anion conductor, one can expect that some interstitials cross the interface and recombine with vacancies. This leads to a depletion zone with an electric field around the interface, just like in a p-n junction. If the interstitial conductor is put to a positive electrical potential, the depletion zone will grow and the ionic current will be low: A regular oxygen in the vacancy conductor would have to dissociate into a vacancy and an interstitial for transport across the interface (similar to thermionic emission in the case of electrons). In the opposite direction, vacancies and interstitials would be "pushed together" into the interface region and recombine there to regular lattice oxygen. Ionic transport is not hindered in that case. In fact, indications of asymmetric oxygen transport across a $La_2NiO_4$/STO interface have been presented at the E-MRS Spring Meeting 2012 in Strasbourg by J. Roqueta *et al.* [45], but has not been published as of now. $La_2NiO_4$ has the same crystal structure as LCO and is an interstitial oxygen conductor. Maier

and Schwitzgebel [46] hinted at such an ionic diode at a PbO—$ZrO_2$ interface as well.

From a chemical point of view, the transfer of electrons in a p-n junction corresponds to oxidation and reduction, and the Fermi level corresponds to the redox potential. Solid state physicists plot band diagrams with a reverse energy scale compared to chemists: Physicists plot low binding energies higher on the scale, and chemists plot low binding energies (meaning easily oxidable species) lower on the scale.

The interaction of oxygen interstitials with oxygen vacancies can be described as the reaction of a Lewis base (oxygen interstitial, electron pair donator) with a Lewis acid (oxygen vacancy, electron pair acceptor) in chemical terminology [8].[2] Protons would only take part in the reaction if water was added to the oxygen interstitials or vacancies: The interstitial $O^{2-}$ would accept a proton and form $OH^-$, which would make an aqueous solution more basic. The oxygen interstitial would accept $OH^-$ from water and leave a proton behind, which would make an aqueous solution more acidic. This is in fact how proton-conducting oxides like $Ba(Zr,Y)O_3$ work: The interstitials are filled with $OH^-$ and the proton can then jump from the $OH^-$ to the next $O^{2-}$. Ionic transport is in this picture always an interaction of Lewis acids (metal cations, protons, oxygen vacancies) with Lewis bases (oxygen anions, other acid anions, ...). If water is present, a Lewis acid is usually also a Brønsted acid and a Lewis base is also a Brønsted base.

If the dimensions of a system approach the size of the interface regions, the entire material does not behave anymore like in the bulk. The electrical field strength in thin films can be enormous even at low voltage due to the low thickness. This leads to nonlinear behavior and strong modulation of the defect structure across the film. Such conditions can, for example, be found in thin oxidic passivation films on metals. Bojinov *et al.* [11] published a treatment of such systems that can serve as an example for the complications that have to be expected in nanoionic systems: The electrical potential drop across the thin film is so large that the entire defect chemistry changes from heavily oxidized, over intermediate, to heavily reduced over a very short length scale. At the same time, the strong field drives non-linear electronic *and* ionic transport processes. The transport leads to chemical reactions at both film surfaces. At the end, all these things couple to each other (potential to partial conductivities through defect equilibria, total conductivity to field strength through Maxwell equations, gradients of the partial conductivities to concentration changes through mass preservation laws, and so on).

Understanding the properties of oxide materials where electronic and ionic point defects work together and interact on interfaces can be difficult, because the system has so many components and degrees of freedom [41, 47]. Silicon and classical compound semiconductors appear to be relatively simple compared to functional oxides, but also do not show such a wealth of properties and physical effects.

Certain oxides, like STO and LAO, are very stable or even thermodynamically stable under ambient conditions and at high temperature over a wide range of oxygen partial pressures. This opens the door for interesting applications, for example electronics

[2] The more common definition of acids as proton donators was developed by Brønsted. The Lewis definition expands this to systems where no actual protons are involved, like in this case. A simpler example of a Lewis acid-base reaction is $BF_3$ (Lewis acid) with $NH_3$ (Lewis base): The two molecules form an adduct because the boron and nitrogen "share" the free electron pair of nitrogen in $NH_3$.

that operate without encapsulation in some environments that are aggressive for silicon. Examples would be implanted devices, like chemical sensors, or electronics and sensors for high-temperature environments. In contrast to silicon, no oxide passivation layer would be formed and functional parts of the device could directly interact with the environment. Field-effect transistors based on STO-LAO interfaces have already been demonstrated by Förg *et al.* [48]. Circuits based on such transistors were presented by J. Mannhart at the conference "Frontiers in Electronic Materials"[49].

### 2.3.1 Perovskites

A widely studied class of mixed oxides with interesting properties are the perovskites "$ABO_3$" (Fig. 2.1a) and related compounds such as LCO (Fig. 2.1b). The defining motif is the combination of small metal cations "B" that are octahedrally coordinated by oxygen with larger cations "A" that fill the gaps between the corner-shared octahedra and balance the electric charges of the ions (compare Fig. 2.1). The bonding situation of A and B is different: The A-site cation has 12 oxygen anions as nearest neighbors and is usually bonded ionically, while the B-site cation forms directional bonds with the six oxygen anions around it. The A-site cation can be much larger (radius around 110 pm to 150 pm) than the B-site cation (radius around 55 pm to 65 pm). In most cases, the A-site cation is correspondingly an alkali, alkaline earth or rare earth metal, while the B-site cation is often a transition metal. The B-site cation has usually the largest impact on the electronic band structure. The unoccupied d-orbitals of the B-site metal become the conduction band of the oxide, simply speaking. The valence band is formed by the occupied p-orbitals of the oxygen that hybridize with the unoccupied B-site d-orbitals. The A-site usually does not contribute to the band structure around the Fermi level. $BiFeO_3$ is one of the very few exceptions from that rule. For this reason, it is currently studied intensively. It is one of the rare cases where magnetic properties couple to electrical fields at room temperature [53].

In oxides, the overlap between the d-orbitals can be somewhere between strong overlap, forming a band just like in classical semiconductors or metals ($SnO_2$, SRO, ...), and nearly complete localization like in ionic crystals ($Al_2O_3$, $LaGaO_3$, ...). If the resulting bandgap is small enough to favor electronic defects over ionic defects, the Fermi level and hence the occupancy of the resulting band structure can be changed over a wide range by varying the type of the large cation, for example by mixing $Sr^{2+}$ and $La^{3+}$, which have very similar ionic radii and show appreciable mutual solubility in many oxides. Exchanging the A-site cations with cations of the same charge can slightly modify the crystal structure due to the different ion radii. This is used to tune ferroelectric oxides where such distortions play an important role. Materials where the cation(s) have a spin, like manganese-based materials, can show a wealth of spin ordering phenomena that are introduced by the coupling between neighboring sites and can be modulated by varying the Fermi level (doping) and orbital overlap (lattice distortions).

The perovskite is often chemically and physically similar to the corresponding pure B-site oxide (Table 2.2). The B-site cation is usually coordinated octahedrally by oxygen in the pure B-site oxide as well. The rutile structure of $TiO_2$ (Fig. 2.1c) is an example for this. These oxygen-metal octahedra define the physical and the chemical properties of the oxide. From a chemical point of view, these octahedra

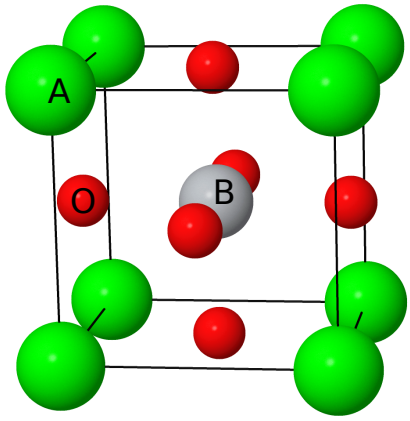


(a) Perovskite $ABO_3$, based on [50]. Many perovskite-type oxides, like LSMO, have a lattice structure with a larger crystallographic unit cell that is based on a distortion of this motif. They consequently have a lower symmetry.

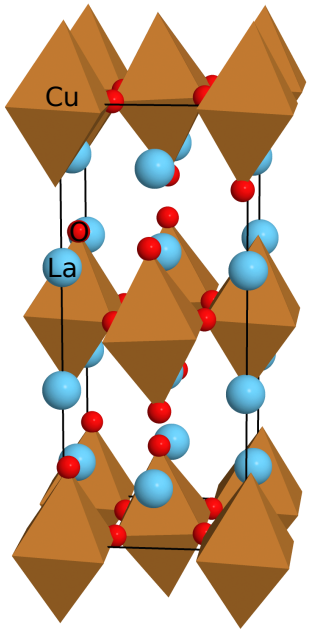


(b) $La_2CuO_4$, based on [51].

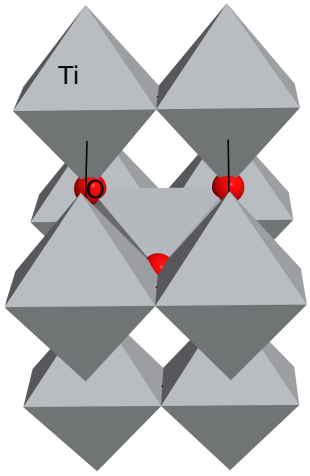


(c) Rutile $TiO_2$, based on [52].

Figure 2.1: Crystal structure of various oxides.

Table 2.2: Comparison between perovskites and corresponding pure B-site oxide

| Oxide | Physical | Chemical |
|---|---|---|
| $SrTiO_3$ | Indirect wide-bandgap (3.3 eV) semiconductor [54] | Stable in acids and bases |
| $TiO_2$ | Direct wide-bandgap (3.0 eV [55]) semiconductor | Stable in acids and bases |
| $SrRuO_3$ | Metal with high work function | Ru(IV) can be oxidized to Ru(VIII), inert in acids and bases |
| $RuO_2$ | Metal with high work function | Ru(IV) can be oxidized to Ru(VIII), inert in acids and bases |
| $SrMnO_3$ | Antiferromagnet [56] | Can be etched by reducing Mn(IV) to Mn(II) with conc. HCl |
| $MnO_2$ | Screw-type magnetic ordering [57] | Can be etched by reducing Mn(IV) to Mn(II) with conc. HCl |
| $La_2CuO_4$ | Complex electronic structure, antiferromagnet, narrow-bandgap p-type semiconductor [58] | Attacked by acids |
| CuO | Antiferromagnet [59], narrow-gap (1.35 eV) p-type semiconductor [60] | Attacked by acids |
| $LaAlO_3$ | Insulator | Inert in acids and bases |
| $Al_2O_3$ | Insulator | Inert in acids and bases |

resemble complexes where the transition metal as an electron acceptor is surrounded by ligands that are electron donors.

### 2.3.2 Oxygen anion conductors

Conventional oxygen conduction in oxides relies on temperature-activated jump processes of the oxygen anions. The random jumps can be biased by a gradient of the electrochemical potential, which results in a total drift current that is proportional to the applied potential gradient when it is not too large. The conductivity increases strongly with temperature. The influence of driving force and temperature are described quantitatively and in more detail in the following Section 2.5.

The ionic conductivity of most oxides is rather low, because the activation energy for a jump is too high and because usually there are virtually no empty lattice sites into which an oxygen anion could jump. In some oxides, however, oxygen vacancies can be introduced by doping, as described previously. A few also allow oxygen interstitials, namely LCO and $La_2NiO_4$. If the activation energy is low enough, in the region of 1 eV, the material can exhibit a high conductivity up to about 1 S/cm at temperatures above 800 °C [61]. At room temperature, the ionic conductivity of such materials is usually unmeasurably low.

The activation energy for ionic jumps in a material can be calculated with numerical models [62], but is usually determined experimentally by fitting the slope of the conductivity as a function of temperature in an Arrhenius plot.

Most ionic conductors in application are not single crystals, but polycrystalline ceramics. Here, grain boundaries and impurities often play a decisive role. Even a single crystal is not free of defects, but usually contains dislocations, stacking faults and impurities or vacancies. Such defects can influence the ionic conduction profoundly in various ways. A short, incomplete overview will be given in the following.

#### Point defects

Point defects, such as vacancies or wanted and unwanted impurities, can form associates with oxygen vacancies or interstitials. In that case they reduce the mobility of the oxygen and hence the ionic conductivity. Dopants for ionic conductors have therefore to be chosen carefully. In practice, many different dopants and concentrations are tried out experimentally for a prospecting host material until an ideal doping recipe is found. The purity of the starting materials is of importance as well. Zirconia, for example, usually contains a certain amount of the chemically similar hafnia. Hafnium doping however reduces the ionic conductivity of zirconia by increasing the activation energy [63]. Results will therefore be influenced by such impurities.

#### Dislocations

In some materials, namely STO [64], dislocations can provide diffusion parts with lower activation energy. The bulk conduction with somewhat higher activation energy and higher cross-section dominates at high temperature. At low temperature, the dislocations with their lower cross-section and lower activation energy are responsible for most ionic transport. In effect, two different conduction regimes can be observed in a conductivity vs. temperature plot. In STO, dislocation cores can easily be made conducting by chemical reduction at elevated temperature [65].

#### Two-dimensional defects

Grain boundaries and interfaces belong to this defect class. A separate contribution from bulk and from grain boundaries can be seen in impedance spectroscopy, like for example in [66]. In this case, grain boundaries reduce the ionic conductivity. Grain boundaries and other interfaces can be accompanied by a space charge region that locally changes the defect chemistry [8]. This can influence both the ionic and the electronic transport properties. In nanostructured ceramics and thin films, the interface regions may span the entire material. This is namely the case in this thesis, where the dielectric is between 10 nm and 40 nm thick. A deviation from bulk properties can therefore be expected. The size of such space charge regions depends on the Debye length $\lambda$ [67] and therefore the free carrier density $N$ via $\lambda = \sqrt{\frac{\epsilon\epsilon_0 k_B T}{q^2 N}}$ ($\epsilon\epsilon_0$: dielectric constant).

In essence, there are many factors that influence the ionic and also the electronic transport properties of an oxide. Real samples always contain all the different defect

types. It is in practice very difficult to analyze the exact structure of a sample and to figure out which factors contribute to the observed overall transport behavior. This is even more so the case for nanoionic systems, where minute amounts are transported over distances in the nanometer region in a very small volume. In this thesis, no conclusive statements about the role of defects and the exact transport mechanisms can be made for this reason.

## 2.4 Chemistry and chemical etching of oxides

In Chemistry, oxides are classically grouped into three categories:

**Basic oxides** form salts with acids. Examples are oxides of alkali metals, alkaline earth metals and rare earth metals.

**Acidic oxides** form salts with bases. Examples are $CrO_3$, $WO_3$ and $Mn_2O_7$

**Amphoteric oxides** react both with acids and with bases. ZnO, $TiO_2$ and $Al_2O_3$ belong to that group.

Two metal oxides, $RuO_4$ and $OsO_4$, do not fit this scheme. They act neither as acids nor as base and are more soluble in non-polar media than in aqueous media.

Some oxides are classified as acidic, amphoteric or basic oxides, but only react in extremely strong acids or bases, or with very strong complexing agents. Under milder conditions they are practically inert. Examples are $\alpha$-alumina (corundum), titania, manganese dioxide or zirconia. The stability is often of advantage for processing and application, but at the same time they can be hard to etch chemically.

Many metals, namely transition metals, can occur in several different oxidation states, meaning that they can form oxides with different stoichiometry and radically different chemical and physical behavior. One important and well-known example is manganese: MnO is a basic oxide; $MnO_2$ is amphoteric, but mostly inert towards acids and bases; and $Mn_2O_7$ reacts as an acid with water to form soluble permanganate anions $MnO_4^-$ and $H^+$. The metal can be transformed between the different oxidation states by oxidation or reduction.

### 2.4.1 Mixed metal oxides

A lot of technologically relevant oxides contain more than one type of metal cation. In some cases, like in cubic zirconia that is doped with yttrium, a solid solution is formed. But in many other cases new phases with novel properties emerge. In mixed oxides of a basic oxide and an inert oxide, the inert oxide often provides a stable "backbone" in which the cations of the basic oxide are embedded. The mixed oxide has therefore usually a chemical behavior similar to the more stable component.

In this work, most oxides belonged to the perovskite family $ABO_3$ or related structures like the layered LCO. They have been described previously in Section 2.3.1.

### 2.4.2 Etching of oxides

These considerations were the guide by which attack routes, potential candidates and then the final optimum etchant were found for various oxides in Section 4.5.

Crystal surfaces need to be clean on an atomic level in order to grow epitaxial layers on them. This is challenging if epitaxial device structures are to be grown, because lithography processes, chemical or ion beam etching, or even exposure to ambient can damage a surface sufficiently to disturb the growth of subsequent layers. On top of that it is sometimes necessary to achieve a specific surface termination.

Chemical etching is the only pattern transfer method that can leave surfaces atomically clean under the right conditions [14, 68, 69]. Other methods, like ion beam etching, damage the surface irreversibly. But the chemical etching process has to be designed carefully for that purpose.

Four processes need to be considered when etching a metal oxide: Protonation of the oxygen anion to form water, dissolution/removal of the different metal cations and the water, (unwanted) formation of insoluble reaction products, and optionally oxidation or reduction of some metal cations. The etch rate is usually limited by only one of these processes. In the case of mixed oxides with a component that is inert towards water, this is usually the protonation and dissolution of the inert component. Here the oxidation or reduction can come into play: It allows for a number of metals to transform the insoluble inert form into a more soluble form. Details can be found in the corresponding patent application [13].

A practical etchant has to be selective: It should not attack other materials, for example the substrate or other films on the sample, and it should leave a suitable etch mask intact. That etch mask is photoresist in the most simple cases, but so-called hard masks, like chromium, are used for etching processes that destroy photoresist. This hard mask then has to be stripped after etching with yet another chemical etching process. Most organic solvents attack photoresist. Water-based etchants are therefore preferable wherever possible.

The etching rate should not be limited by transport processes, like diffusion of the etchant or the product(s). Transport limitation would give an uneven etch rate with faster attack at the edges where diffusion is faster (2D diffusion vs. 1D diffusion). The etch rate then also increases if the etchant is agitated, which makes it harder to control. The etch rate should instead be limited by the surface reaction rate. High etchant concentrations are therefore preferable. A complexing agent may help to drive a reaction[3] or prevent the precipitation of products. The pH and redox potential can be stabilized with a chemical equilibrium, i.e. a pH buffer or redox buffer, to get constant etching conditions even if the etchant is partially used up. This stabilization is important for etchants that work at near-neutral pH, because oxide dissolution consumes protons and thus increases the pH in the reaction zone unless a pH buffer resupplies the protons.

The etching rate has to be high enough so that the process is finished after a few minutes. Otherwise the etchant may slowly creep under the photoresist on the edges. It also has to be slow enough so that the process takes more than about 10 seconds, so that it can be controlled. Thicker films therefore need faster etchants and thinner

[3] Example: $CN^-$ drives the oxidation of gold by atmospheric oxygen through the extremely stable $[Au(CN)_2]^-$ complex

films slower ones. In an ideal case, the etch rate of an etchant can be tuned, for example by varying the pH. Slowing down a reaction by diluting the etchant is not viable, as explained in the previous paragraph. Heating may speed up a sluggish reaction, but requires agitation and precise temperature control.

In order to achieve a good etching result and selectivity towards photoresist and other oxides, all aspects of the etchant need to be carefully designed. Using "strong" chemicals like concentrated mineral acids to drive the dissolution of relatively inert oxide components is not such a good idea because they drive the dissolution of the more soluble component to such a level that it is leached from the crystal structure, leaving the less soluble component behind in form of precipitates on the surface. This is for example an issue with the etching of LSMO by concentrated hydrochloric acid on an STO substrate, which leaches Sr from the STO and leaves precipitates of (presumably) $TiO_2$ on the surface. Water in the etching medium can also be a problem because of it's strong tendency to form hydroxides. In organic media, in turn, the protonation and the dissolution of ionic species can be a limiting factor, and photoresist is usually not suitable as an etch mask because it dissolves. The combination of PMMA resist and ethanol or isopropanol as solvents is a rare exception from this.

A chemical etchant that is based on bromine reacting with ethanol and traces of water is known for the sensitive copper-based oxide superconductors. In order to be effective, the bromine has to oxidize the ethanol and form, among other products, hydrobromic acid and acetic acid [70]. Due to the low activity of water, the formation of hydroxides is inhibited and the etchant shows a slow, even attack with very good surface quality and good selectivity towards PMMA resists and substrate materials [68].

In practice, a good etchant should

- be as selective and mild as possible,
- have a controllable etch rate within a narrow corridor,
- be limited by the surface reaction rate,
- be buffered or stabilized for stable operation,
- not form precipitates or leave residues,
- be stable over a long time for storage,
- be cheap and safe to use and dispose of.

### 2.4.3 Rinsing

Care should also be taken when samples are rinsed after the etching process. For water-based etchants, deionized water is a natural choice to wash off any remaining etchant and stop the etching process. A sample should be rinsed several times in water or under flowing water to remove any traces of the etchants. Water is however an aggressive chemical for many oxides because it can protonate or hydrate them. The oxide is then dissolved or turned into a hydroxide. For water-free etchants, the solvent for rinsing should therefore be free of water as well. In this case the

rinse should be a good solvent for all the components of the etchant (solvent, active components and impurities) and for all the reaction products of the etching process. Otherwise a second phase (liquid or solid) may form due to limited mutual solubility of some of the components. Such effects would be detrimental for etching because it would leave residues of the etchant or the products on the sample. The rinse should leave the etch mask intact in order to protect the film from etchant carryover during rinsing. The mask is then removed in a following step.

In conclusion, a good chemical etching process needs quite a bit of development work. It requires a good understanding of the underlying processes and driving forces to find suitable etchants and formulate them for a given application. Knowledge of inorganic chemistry [71] and thermodynamics is invaluable for work in this field.

## 2.5 Linear and non-linear conductance

For understanding nanoionic systems it is necessary to combine solid state physics (electronic effects) with solid-state ionics (mobile ions). It turns out that the governing laws and principles are often the same: The Shockley equation Eq. (2.2) [72] for the current $I$ of a diode is equivalent to the Butler-Volmer equation Eq. (2.3) [73, 74] for the current $I$ of an electrode in electrochemistry. The '-1' term in Eq. (2.2) means that the second exponential term in Eq. (2.3) is ignored, i.e. one of the charge transfer coefficients in Eq. (2.3) is nearly 0.

$$I = I_s \cdot \left( \exp\left( \frac{V_D}{\nu \cdot V_T} \right) - 1 \right) \tag{2.2}$$

$$I = A \cdot i_0 \cdot \left( \exp\left( \frac{\alpha_a n F}{RT} (\Phi - \Phi_{eq}) \right) - \exp\left( -\frac{\alpha_c n F}{RT} (\Phi - \Phi_{eq}) \right) \right) \tag{2.3}$$

$I_s$ Scale current, dependent on temperature

$V_D$ Diode voltage

$V_T$ "Thermal voltage", $V_T = \frac{k_B T}{e}$, with $k_B$: Boltzmann constant; $T$: Absolute temperature; $e$: unit charge;

$\nu$ Ideality factor

$A$ Electrode surface area

$i_0$ Exchange current density, dependent on temperature

$F$ Faraday constant, $F = eN_A$, with $N_A$: Avogadro constant

$R$ Ideal gas constant, $R = N_A k_B$

$\Phi$ Electrode potential

$\Phi_{eq}$ Equilibrium electrode potential

$n$ Number of electrons in the electrode reaction

$\alpha_a$ Anodic charge transfer coefficient

$\alpha_c$ Cathodic charge transfer coefficient

How the different variables are named depends on the field of study, but the structure of these two equations is identical. The subject of both these formulae is the transport of charged species with the help of thermal activation as a function of required activation energy, temperature and external electrical driving force. The scale current $I_s$ and exchange current $i_0$ are both proportional to $\exp(-\Delta H_a/k_B T)$, with $\Delta H_a$: activation enthalpy. In both cases, the amount of transported species is limited by the probability that a state with the necessary energy is occupied. That can be a vibrational state of an ion in a crystal lattice, or the concentration of minority carriers in a semiconductor, like in the space charge region of a p-n junction which limits the diode current. At sufficiently high temperature and low occupancy of the respective state, like in these examples, for both cases the Maxwell-Boltzmann statistics describes the occupancy of a state as a function of energy and temperature, and the resulting function for transport as a function of activation energy, temperature and electrical driving force is the same. In essence, the resulting formula has the following structure:

$$I = X \cdot \exp\left(\frac{-\Delta H_a}{k_B T}\right) \cdot \left[\exp\left(\frac{a_1 q U}{k_B T}\right) - \exp\left(-\frac{a_2 q U}{k_B T}\right)\right] \tag{2.4}$$

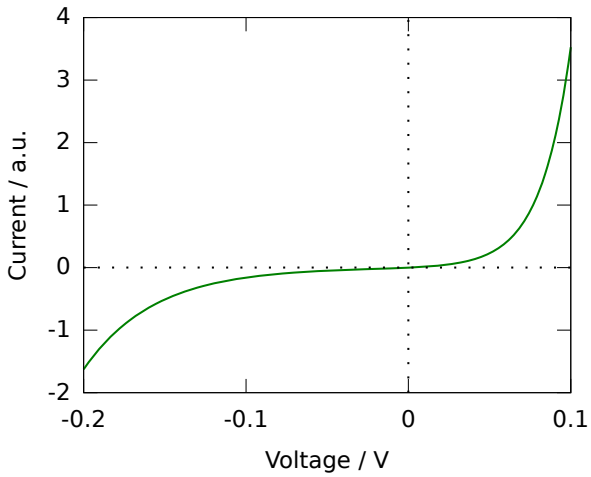


Figure 2.2: Plot of Eq. (2.4) with $X = 10^{15}$, $T = 300\,\mathrm{K}$, $\Delta H_a = 1\,\mathrm{eV}$, $a_1 = 0.7$, $a_2 = 0.3$, $q = 2e$. Note the nearly linear behavior around 0 V and the exponential increase at higher voltage. The asymmetry results from $a_1 \neq a_2$.

It is split into three parts: A pre-factor $X$ that is independent on temperature and potential, and contains, for example, geometrical factors and entropic contributions; a temperature-dependent Arrhenius term that contains the activation enthalpy; and a difference of exponential terms that contains the influence of potential difference $U$ on the carriers with charge $q$, including asymmetry factors $a_1$ and $a_2$. In the case of the Shockley equation for diodes, the behavior is very asymmetric and the second

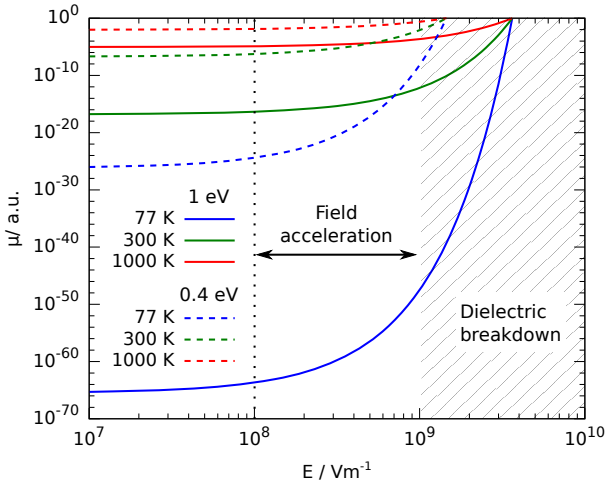


Figure 2.3: Calculated relative mobility as a function of field strength at liquid nitrogen temperature, room temperature and solid oxide fuel cell operating temperature for an activation energy of 1 eV (typical for good oxygen anion conductors) and 0.4 eV (very low activation energy, for example in dislocation cores). The curves are calculated with Eq. (2.5) following [6, 7]

.

term in the difference becomes $\approx 1$ for moderate voltages. A plot of this equation is shown in Fig. 2.2.

This formula can be made plausible with the following picture: In equilibrium, there is no *net* charge transport, but still a random, thermally activated exchange between the two sides of the barrier. This corresponds to an equal forward and backward exchange current. When an external driving force is applied, the activation enthalpy for one of the directions is slightly lowered, while the other one is slightly increased. With $\exp(x+y) = \exp(x)\exp(y)$, the difference between forward and backward current with lowered and increased barrier can be split into a term for the exchange current, containing only the activation enthalpy, and a difference of exponential terms that contains the influence of the external driving force. This is then Eq. (2.4) above.

The exponential function can be defined as $\exp(x) := \sum_{n=0}^{\infty} \frac{x^n}{n!}$. From this it follows directly that $\exp(x) \approx 1 + x$ for $|x| \ll 1$[4]. That means for $a_i qU \ll k_B T$, the well-known Ohmic behavior results where the current is proportional to voltage. But when this condition is not fulfilled, i.e. at high potential differences or low temperature, the transport will become non-linear. One of the terms increases exponentially with voltage while the other one converges to 0.

The same formula applies to ionic transport in solids [7]. The ions perform random temperature-activated jump processes from occupied sites into neighboring vacancy sites. For each jump from one site to the other, they need to have the necessary activation enthalpy $\Delta H_a$ – close to 1 eV for good oxygen anion conductors. In order

[4]The higher-order terms in the sum converge quickly to 0 when $|x| \ll 1$.

to estimate at which electrical field strength the transport transitions from linear to non-linear, one can approximate the jump distance of an oxygen anion in a perovskite as the length of an oxygen octahedron edge $a$. This distance is in the range of 275 pm. The potential barrier is lowered by half the potential difference between start and end of the jump[6]. A field strength $E$ of 1 MV/cm therefore lowers the activation energy barrier by 0.0275 eV for doubly charged oxygen ($q = 2e$). This is not small anymore compared to the total activation energy and is roughly the same as $k_BT$ at room temperature: $k_BT = 8.617 \cdot 10^{-5}\,\mathrm{eV/K} \times 295\,\mathrm{K} = 0.02542\,\mathrm{eV}$. Starting form this range of electrical field strength, the transport is therefore accelerated exponentially (Fig. 2.3). A relative value for the mobility $\mu$ as a function of temperature $T$ and field strength $E$ can be derived from Eq. (2.4) following refs. [6, 7]:

$$\mu \propto \exp\left(-\frac{(\Delta H_a - 0.5aqE)}{k_BT}\right). \tag{2.5}$$

The general behavior and the order of magnitude for the field strength where non-linear effects occur were confirmed with the work for this thesis (Section 6.6).

The formula does not apply anymore when there is no temperature contribution to the transport process. This would be the case when the field contribution exceeds the activation energy. This is discussed in more detail in Section 6.10.

## 2.6 Development of memory technologies

To date, there are five ruling memory or storage technologies in the market. These are optical media, like CD or DVD; magnetic storage, like in hard drives; EEPROM ("Flash") like in memory cards for cameras, USB sticks or solid-state discs (SSDs); DRAM as working memory for computers; and SRAM for CPU caches. These technologies have all been in a leadership position for roughly 20 to 30 years by the time of writing. The work in this thesis is less related to magnetic recording or optical media and more to solid-state memory.

The important performance characteristics to compare memory technologies are write and read speed, latency, price per storage capacity, size per storage capacity, price per unit or price scaling, energy consumption on standby and during data transfer, robustness and retention, cyclability, and environmental impact. Each of the five ruling technologies offers a favorable combination of these characteristics that allows them to remain in the market for specific applications. Those characteristics have improved dramatically for each of the technologies over the past years, following exponential scaling laws ("Moore's law" and others).

The ongoing race for higher and higher performance and density has been driven by simple geometrical downscaling and also so-called "equivalent scaling" [5], which means that aspects of a technology, like materials or cell layout, have been improved for better performance. It is believed that further improvements through scaling are getting more and more difficult [5, 75] as physical limits are being approached. Some alternative concepts may fill that gap. The details are laid out in the parts "Emerging Research Devices" (ERD) and "Emerging Research Materials" (ERM) of the "International Roadmap for Semiconductor Technology" 2011 (ITRS2011) [5].

The three most important characteristics are density per area, which governs the manufacturing price; write and read energy, which governs power consumption; and

durability/cyclability. A comparison of these factors between mainstream technology, prototypes, research devices and targets for future devices can be found in tables 3, 5, and 9 of the ITRS2011, section ERD [5]. Only for phase-change memory (PCM) and so-called "redox memory" (ECM, VCM, and thermochemical memory (TCM)) could potentially competitive properties be demonstrated so far.

In order to do research with relevance for application in this field, it is important to keep an eye on these values. A newly proposed memory should have the potential for a superior combination of *all* the relevant characteristics for a specific use case. Application-directed research activity should lead to an improvement of at least one of the characteristics for a mainstream or emerging technology. The devices that were manufactured during work for this thesis did not have competitive properties in *any* of the important characteristics. Pursuing a direct application is therefore not promising. They did however improve the understanding of the fundamental transport processes in oxide nanostructures, which will hopefully help to design better memory elements in the future.

## 2.7 Physical vapor deposition of epitaxial oxide films

Common methods for oxide epitaxy work with an intermediate gas phase[5]. These methods are classified into chemical and physical methods. Chemical methods have to be developed and optimized individually for each compound and get more and more difficult with the amount of species used. Chemical vapor deposition (CVD) of metal oxides is especially tricky because volatile precursors have to be found. Often, those are highly reactive metal-organic compounds, such as alkoxides or alkyls that are sensitive to water or (moist) air.

Physical methods are more established. In practice, PLD, MBE, sputtering and reactive sputtering are used. Each method has its advantages and disadvantages. All methods operate in a low-pressure environment. In the following sections they will be briefly introduced. The substrate is heated to a temperature of several hundred degree centigrade to obtain epitaxial films. The films are polycrystalline or amorphous at low deposition temperature.

### 2.7.1 Substrate preparation

Single-crystalline oxide substrates for epitaxy need to be clean, flat and perfectly ordered on an atomic level. Commercially they are first ground and polished with hard abrasives of decreasing grain size. This damages the crystal superficially. Chemical-mechanical polishing (CMP) is used as a last step to remove this damaged layer completely with a combined chemical and mechanical attack – hence the name. The polishing medium is typically a colloidal $SiO_2$ slurry with a pH and composition that is adapted semi-empirically for each substrate type. Ceria- and alumina-based slurries are sometimes used as well, depending on the circumstances. It is used on a polishing pad with defined hardness and stiffness. The colloid particles are very small and not hard enough to scratch the crystal surface. The polishing medium first softens the very surface of the crystal with a chemical attack, for example hydrolyzation and leaching of the outermost atomic layer. Only this softened layer is

[5]Liquid phase epitaxy exists as well, but is far less common

then abraded by the colloidal particles, preferentially at protruding sites because of higher local pressure. In effect, this flattens the surface down to an atomic level and removes the mechanically damaged surface layer without introducing new damage. The process has to be stopped at the right time, because overpolishing may introduce dimples: CMP is not good at global planarization, but only at local planarization on an atomic level. A detailed description of CMP can be found in [76].

The polishing medium has to be removed immediately and completely once the process is finished. This is done with several rinsing steps and ultrasonication. Remaining particles harden by eliminating water from the silicic acid until only hard $SiO_2$ remains. They can also crosslink chemically with $-OH$ groups on the crystal surface via the same mechanism, attaching them very firmly.

### 2.7.2 Film growth

Epitaxial films are on the way to thermodynamic equilibrium during deposition. A complicate interaction of kinetics and thermodynamics leads to the final film structure after cooling. The growth temperature has a particularly strong influence.

Arriving atoms or ions first diffuse relatively freely on the surface. They attach themselves to preferential binding sites when they come across them on their random walk. Such sites can be steps, kinks or islands. As soon as an attached species is surrounded by other newly arriving species, it usually does not have enough activation energy to leave that place within the time frame relevant for layer growth.

Usually, the growing film is different from the substrate (heteroepitaxy). Homoepitaxy is sometimes used to form a surface layer with better defined properties compared to the crystal bulk. Such techniques are common for silicon epitaxy, for example.

If steps and kinks are the only preferred sites, regardless of material type, and if the terraces from a slight miscut of the substrate are within reach for surface diffusion, the new layer will grow in the so-called step-flow or layer-by-layer mode. The atomic steps or terraces that are present on all polished high-symmetry crystal planes just move forward collectively and build up the film layer-by-layer, hence the name. The resulting layers are almost as flat and perfect as the substrate, which makes this the preferred growth mode.

If the diffusion length is lower than the terrace width, the growing film will nucleate in the form of islands. Mechanical stress between substrate and growing film builds up if the lattice constants don't match very closely. Such stresses lower the binding energy at the edge of a growing terrace and slow down the growth. This can lead to island growth or Stranski-Krastanov growth. The result is a rougher film with columnar, slightly misoriented grains that are separated by low-angle grain boundaries. For this thesis, such a layer quality was acceptable as long as there were no larger precipitates.

If the substrate and film are incompatible, the film will grow in the form of larger grains that try to minimize the contact area with the substrate. Very rough, polycrystalline films with poor adhesion are usually the result. This was observed when evaporating $RuO_2$ from hot oven parts condensated on substrates and severely inhibited epitaxy. The resulting films had macroscopic grains and a milky appearance. Such layers were unusable.

Very small particles on the surface can dissolve inside the substrate or the growing film. Larger particles remain and cause problems. The substrates have to be very

clean for this reason. AFM (Section 4.2) is the tool of choice to observe the surface morphology of a substrate or film. The thickness and crystal parameters (phases, orientation, strain) can be determined with X-ray reflectivity and X-ray diffraction (Section 4.3).

### 2.7.3 Pulsed laser deposition

Ultrashort excimer laser pulses are focused on a ceramic target. This atomizes a small volume of material at the focus point and emits it in the form of a plasma plume normal to the target surface. The plume interacts eventually with a gas atmosphere (usually oxygen at different pressures) and then reaches the substrate where the material is deposited. The deposition rate can be significantly higher than for high-pressure oxygen sputtering, depending on the parameters.

In a first approximation, the stoichiometry of the deposited film is the same as the target, but in practice there are relevant deviations from different atomic masses of the components [77]. Gas background pressure, pulse energy and target-substrate distance play an important role. The particles in the plasma plume have originally a high energy of several hundred eV. They are moderated by collisions with the background gas at sufficient pressure. The variable stoichiometry of PLD-deposited films can both be an advantage or disadvantage, depending on what kind of investigations are supposed to be performed. High-energy bombardment can have unwanted side effects and lead to intermixing or even introduces conductivity [78]. A sufficient background pressure should therefore be maintained.

The deposition process can be monitored with reflection high-energy electron diffraction (RHEED).

### 2.7.4 Molecular beam epitaxy

MBE is in principle an elaborate form of evaporation under UHV conditions on a heated substrate and with low deposition rate. A separate evaporation source has to be used for each evaporated component. Usually pure metals are used. An oxygen, ozone or nitrous oxide jet is used to supply oxygen to the growing oxide film.

The deposition rate is usually fairly low, in the nm/min region. Films can be grown as an alloy by operating several sources at once or separately layer-by-layer by opening the source shutters sequentially while monitoring the growth with RHEED.

Typical problems are source stability, maintaining background pressure and evaporation of contaminants from hot components of the source.

### 2.7.5 Sputtering

A glow discharge is ignited on the target that acts as the cathode. Positively charged ions from the plasma are accelerated towards the target and eject ions or neutral atoms from the surface. These diffuse towards the substrate that is placed close to the plasma and form a film. The stoichiometry of the target is transmitted rather precisely to the substrate after an initial equilibration phase during pre-sputtering. Deviations may result from ion bombardment of the growing film or evaporation of volatile components. Some metal oxides, namely $RuO_2$ and $Bi_2O_3$, have a relatively

high vapor pressure. Oxides that contain Ru or Bi can therefore only be deposited at sufficiently low temperature or from targets with Ru or Bi excess.

Reactive sputtering is often used to deposit oxides or nitrides of materials like Al, Zn, Zr and Ti. In these cases, a metal target is used and oxygen or nitrogen are added to the sputter gas. The oxygen or nitrogen reacts with the sputtered metal and the growing film. This is less practical for metals that are unstable in air, such as alkali, alkaline earth or rare earth metals. It is therefore not used for mixed oxides that contain such elements in large amounts.

Oxygen can form negative ions in a plasma, as opposed to noble gases. Such negative ions are accelerated away from the target and towards the substrate, where they may lead to damage. High-pressure oxygen sputtering was developed to moderate the energy of negative ions by numerous collisions with gas atoms before they can reach the substrate and to achieve the highest oxygen partial pressure possible during growth [79]. Some materials, namely YBCO, have to be deposited at very high oxygen partial pressure. High-pressure oxygen sputtering is the method of choice for such materials.

The plasma can be ignited either from DC power or from RF power. The sputter voltage in the case of DC sputtering is just the applied voltage. In the case of RF sputtering, the sputter voltage, called DC bias, results from interactions of the plasma with chamber walls and target that put the target to a negative potential relative to the plasma.

DC sputtering only works with conducting targets, while RF sputtering also works for insulators if the target disc is thin enough. The conducting target holder, insulating target disc and conducting plasma act as a plate capacitor and allow transfer of power from the source through the target into the plasma.

The deposition rate of high-pressure oxygen sputtering is low, in the nm/min region for DC or in the 10nm/h region for RF sputtering. RHEED during growth is not possible due to strong electrical fields and high gas pressure. Ellipsometry or a quartz crystal microbalance (QCM) could potentially monitor the film growth.

# Chapter 3

# Concepts

The objective for this work was to measure the change of electrode conductance in a crossbar structure. Such a structure needs to fulfill a number of criteria for this purpose. A crossbar is furthermore probably not the ideal configuration. This will be analyzed in this chapter, and design requirements and suitable materials will be derived. Some preliminary analysis and calculations were performed for the manufacturing process, the intended measurements, and the control and data processing software as well.

## 3.1 Device layout and scaling behavior

In the exposé for this thesis by U. Poppe [80], the device was envisioned as similar to a FET (Fig. 3.1).

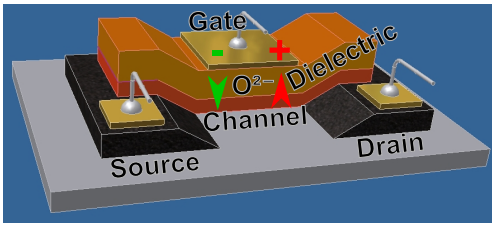


Figure 3.1: Conceptual drawing of the envisioned device (R. Speen, modified).

A comparatively large and simple crossbar structure to be created with shadow masks (see Chapter 4 for details) was developed by U. Poppe before work for this thesis begun. The shapes and the layer sequence are depicted in Fig. 3.2. Two identical devices were made in one process on a sample to get an idea how the properties spread. They should have identical properties if no defects are present and the manufacturing process is completely understood and under control.

The proposed crossbar device can be described, in a first approximation, as a network of various resistors, varistors and capacitors (Fig. 3.3). The electrodes have a significant resistance so that they cannot be treated as surfaces of equal potential if a significant current is flowing.

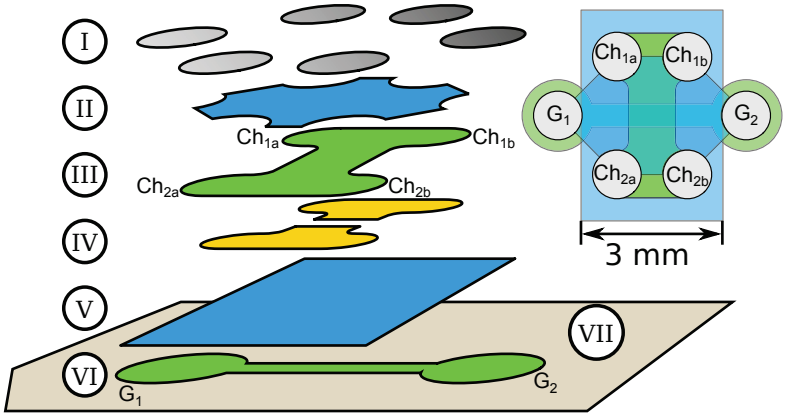


Figure 3.2: Sketch of the shadow masks used for the first batch of devices. The contact labels correspond to the terminals of the equivalent circuit (Fig. 3.3). (I) silver contacts; (II) STO passivation; (III) LCO channel; (IV) Sr:LCO channel contacts; (V) STO dielectric; (VI) Sr:LCO gate; (VII) STO substrate.

First experiments revealed that the current through the dielectric increases exponentially with the applied voltage (see Section 5.3). This corresponds to the characteristic curve of a varistor. The crossover area is furthermore a plate capacitor. Depending on the oxide that is used as a dielectric, the capacity may depend on the applied voltage. This should be the case for a ferroelectric or paraelectric material like for example STO.

The dielectric needs to have a sufficiently small conductance compared to the channel, at least in the low-voltage regime, so that the channel is not shunted by the conducting gate through the dielectric (Fig. 3.4). During writing, the write current is non-uniform across the dielectric because of the voltage drop inside the electrodes across the crossover area (Fig. 3.5). The non-linear characteristic curve of the dielectric enhances this effect. This localized writing effect has been demonstrated for larger devices that were produced with shadow masks [1].

In cases where the voltage drop in the electrodes dominates over the voltage drop in the dielectric, the measured conductance in four-point geometry can become negative (Fig. 3.6). This is a side effect of the crossbar structure. A device layout without this effect has been designed (Fig. 3.8).

The conductance of the dielectric scales with the area of the crossover. The conductance of channel and gate across the crossover is constant with respect to proportional lateral scaling: width and length change by the same factor and the effects on conductance cancel each other exactly. This means that smaller devices allow higher write current densities through the dielectric and suffer less from channel or gate shunting or localized writing [14]. A crossbar with smaller dimensions is shown in Fig. 3.7. This layout was developed to first verify the lithographic manufacturing process before adapting the measurement setup and programs for the measurements in van-der-Pauw geometry. This design (Fig. 3.8) has not been tested because there was not enough time left after the manufacturing process was ready.

It is generally not possible to estimate the crossover conductance just from material

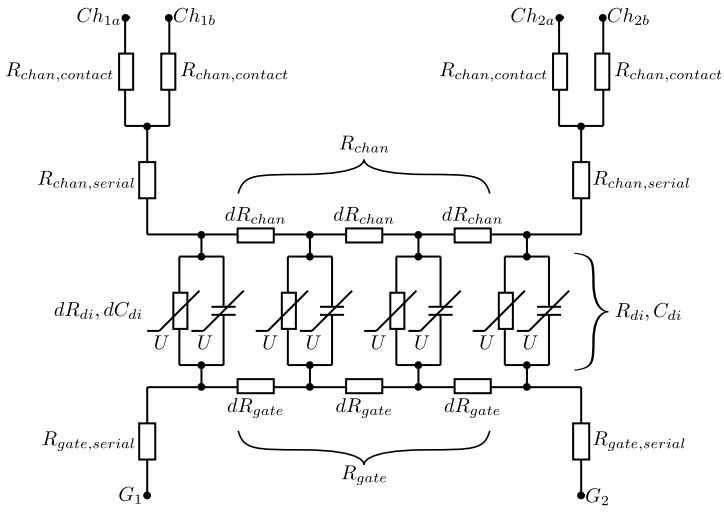


Figure 3.3: Equivalent circuit to explain material constraints and scaling behavior. The series of elements in the crossover area is to be understood as a network of differentially small resistors, capacitors and varistors over the crossover area between channel and gate.

conductivity data: Interface effects, like Schottky junctions or p-n junctions dominate the conductance. The device has to be understood as a metal-semiconductor or semiconductor-semiconductor heterostructure from an electronic point of view. From a chemical point of view it is an electrochemical cell where the dielectric is the electrolyte.

The channel and the dielectric should be made as thin as possible. A thinner dielectric needs a lower voltage to achieve the necessary field strength. A thinner channel gives a stronger relative conductance change for the same amount of transported oxygen. Ideally, the thickness of the channel should be in the range of the Debye length to allow the electric field to drive oxygen into the entire depth of the channel layer.

## 3.2 Choice of materials

The electrodes should be good electronic conductors and change their conductivity as a function of oxygen content. They should furthermore allow oxygen anion transport. Mixed ionic-electronic conductors (MIEC) like they are used for SOFC cathodes are good candidate materials. The material should furthermore grow as high-quality epitaxial film on suitable substrates and be compatible with other materials on the sample. It is advantageous if a material becomes very insulating when a lot of oxygen is removed or introduced. The transport is in that case self-limiting, because a fast transport channel is automatically disconnected once the electrode(s) have been saturated and become insulating at that location. Otherwise the device might form a shortcut from excessive localized transport, like in filamentary resistive switching [2]. A material with high mobility can achieve a sufficient conductivity at relatively low

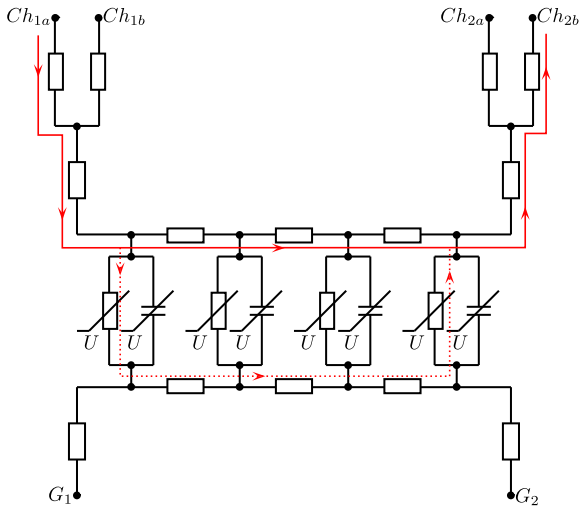


Figure 3.4: The current is supposed to follow the solid path along the channel, but it can bypass the channel and take the dotted path if the channel conductance is too low compared to the dielectric and gate conductance. The same holds for the gate.

absolute carrier density. The relative effect of varied oxygen doping is in this case larger for the same amount of transported oxygen, which improves the sensitivity. Such a material has also a larger Debye length due to the lower carrier density, which makes the electric field penetrate deeper into the layer and helps to incorporate the oxygen.

The dielectric should be a bad electronic conductor. It should allow ionic transport. It is not quite clear if it should be a dedicated ionic conductor like typical SOFC materials or if it can be any oxide and conductivity is enforced by the strong field[1]. The materials should grow epitaxially with high quality on the bottom electrode and allow epitaxial deposition of the top electrode.

The materials have to be stable in air, water and alkaline solutions (developer) in order to be suitable for standard optical lithography. LCO cannot be used for standard photolithography because it is too sensitive to water. PMMA-based resists for electron beam lithography are suitable for this material because they are processed exclusively with organic solvents. PMMA can be exposed with hard UV light in specialized mask aligners as well.

The material should not be toxic or otherwise problematic to not contaminate the sputter chamber or create additional trouble during target mounting and preparation. The targets should be sufficiently stable on moist air, which excludes materials that contain, for example, Co(III).

To check if ionic diode effects play a role it is interesting to investigate both interstitial oxygen conductors and vacancy oxygen conductors. LCO and the isostructural

[1] Amorphous alumina is a pretty bad ionic conductor. However, when aluminum is anodized, the extremely strong electric field forces oxygen through the amorphous alumina at an appreciable speed.

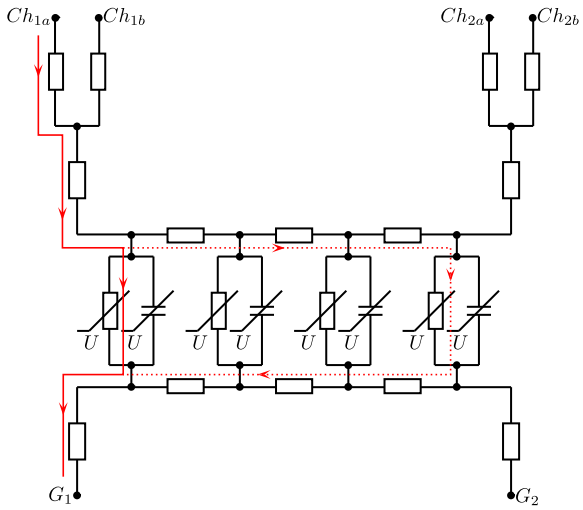


Figure 3.5: The current that flows along the dotted path has to pass the serial resistance of the electrodes in the crossover area. The current will therefore flow preferentially along the shorter path drawn with a solid line.

$La_2NiO_4$ [81] are interstitial oxygen conductors, but nickel oxides are unfortunately regarded as carcinogenic.

Choosing well-characterized, popular materials is in my opinion a good idea because a lot of reference data is available from the literature.

LCO and LSMO were used as electrode materials. Both change the conductivity as a function of oxygen content [34, 82] and are relatively good conductors. LSMO is a standard MIEC cathode material for SOFC. It is also a room-temperature ferromagnet that has been studied extensively. Doped LCO is investigated as an alternative SOFC cathode material for lower temperatures [83]. This material is furthermore the first known copper-based high-temperature superconductor, and electronic structure and properties have been investigated in great depth. Both materials can be grown epitaxially with good quality on perovskite substrates, namely STO. LCO can be oxidized electrochemically at room temperature [32, 34, 35], which dopes the film and turns it into a good conductor and a high-temperature superconductor.

STO was used as a dielectric because it is one of the most studied perovskites. It does show ionic as well as electronic transport, especially when doped [84, 85]. Structural defects, like dislocations, seem to play an crucial role for both ionic and electronic transport. It is in pure form insulating enough to be used as a dielectric.

LSGM is a high-performance vacancy oxygen anion conductor for SOFC. This material has perovskite structure and is therefore better suited than YSZ with fluorite structure for epitaxy on perovskites. Unfortunately there was not enough time to try these two well-known oxygen anion conductors.

$La_{1.85}Sr_{0.15}CuO_{4\pm x}$ (Sr:LCO) and SRO were used for contacts with high conductivity.

Silver was used to make ohmic contacts to the noble metal SRO and to the p-conducting LCO and LSMO. It has good adhesion to these oxides, especially when

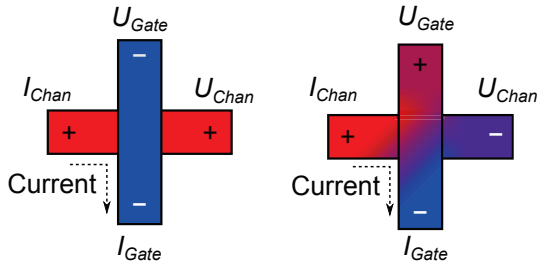


(a) The voltage drop over the dielectric can be measured in four-point geometry if most of the voltage drops over the dielectric.

(b) The voltage drop measured in four-point geometry is reversed if too much voltage drops in the electrodes compared to the voltage drop across the dielectric.

Figure 3.6: Parasitic voltage drop in the electrodes of a crossbar structure measured in four-point geometry with current terminals $I_{chan}$ and $I_{gate}$ distorts the voltage drop over the dielectric measured at the terminals $U_{chan}$ and $U_{gate}$, and can even invert it.

sputtered with oxygen residuals in the sputter gas.

## 3.3 Complexity of the manufacturing process

The devices are built layer-by-layer from different materials. Such a multistep process has to be developed carefully, because the total probability of success $p_{tot}$ is the probability of success $p$ in one of the steps exponentiated by the number of steps $n$: $p_{tot} = p^n$. Fig. 3.9 demonstrates the chances of success depending on success rate per step and number of steps.

In a given time $T$ one has a number of attempts $N = \frac{T}{t \times n}$, with $t$ being the time per process step. The probability $P$ to get at least one working sample in a given time $T$ is therefore

$$P = 1 - (1 - p_{tot})^N = 1 - (1 - p^n)^{\frac{T}{t \times n}} \tag{3.1}$$

The goal is to increase $P$ within a realistic time $T$ by finding a balance between $t$ and $p$, i.e. between speed and diligence. In the case of the samples for this thesis, the number of steps is six. For such a complex process, it is worth to spend more time on process optimization in order to increase $p$, on the expense of increasing $t$ as well. Each process step has to be optimized independently before it makes sense to attempt producing a sample. Things to consider are deposition conditions, lithography parameters, etching methods, cleaning, compatibility tests, mask layout and so on. There are still enough things that can go wrong when the different steps are put together: The last test sample for lithographically defined LCO electrodes ultimately failed after a month of work because the photo masks were not designed for the requirements of LCO processing – which I realized only when the sample was nearly finished – and a workaround in the last but one processing step degraded the device due to an unexpected side effect. That was the end of experimental work for this thesis: I decided that the risk of wasting months of work on making more

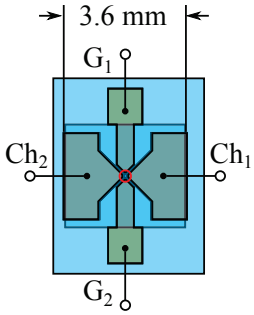


(a) Total view of the device. It is pin-compatible with the first layout (Fig. 3.2).

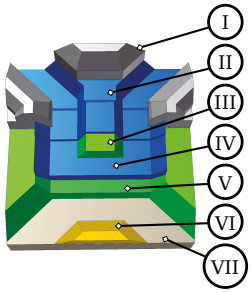


(b) 3D diagram of the crossover area. (artwork: R. Speen)

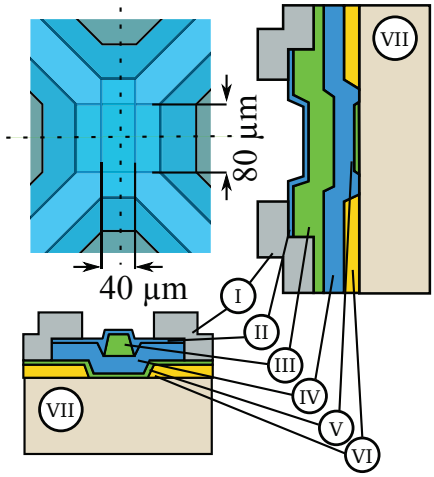


(c) Crossover area with cuts along the indicated axes.

Figure 3.7: The second generation layout is again a crossbar, but with smaller crossover area. It is manufactured with lithography [14]. (I) silver contacts; (II) passivation; (III) gate; (IV) dielectric; (V) channel; (VI) SRO contacts; (VII) substrate.

samples in the short remaining time was too high and focused on writing up the results instead.

## 3.4 Measurements

Measuring the device properties is not trivial. The properties of the electrode-dielectric-electrode junction, both the channel and the gate electrode, and also the contacts have to be explored in a large parameter space of write current and write time. The electrode-dielectric-electrode junction behaves nonlineally, so that characteristic curves have to be recorded instead of taking a single measurement. Simultaneous measurements would be difficult, because a rather high voltage and current is used to change the state of the device, while the properties themselves

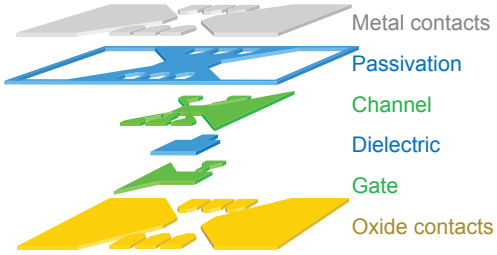


(a) 3D diagram of the layer sequence

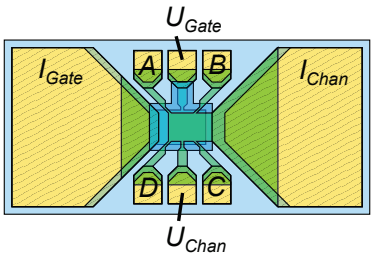


(b) Top view of the layers with terminal names

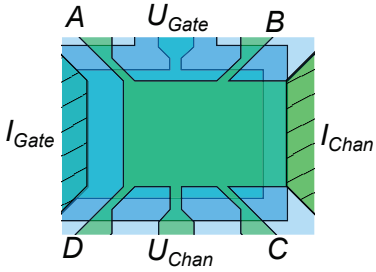


(c) Top view of the central region

Figure 3.8: Device layout for conductance and Hall measurements in van-der-Pauw geometry. $I_{Gate}$: Current terminal of the gate. $I_{Chan}$: Current terminal of the channel. $U_{Gate}$: Voltage terminal of the gate. $U_{Chan}$: Voltage terminal of the channel. $A$, $B$, $C$, $D$: Terminals for van-der Pauw conductance and Hall effect measurements of the channel.

change only slightly, in the permille range. The write current would then disturb the other measurements, unless special techniques like AC measurements in conjunction with a lock-in amplifier are used. A setup with a sufficient number of input and output channels was furthermore not available, and therefore a switch was used to connect the measurement devices to various terminals of the device sequentially. Only non-volatile changes can be detected that way, but that was exactly the scope of this work and thus not a significant obstacle. Care must be taken to not alter the state of the device during measurements. Therefore the voltages and currents used for measuring have to be significantly lower than the lowest write current and write voltage. The used devices (see Section 4.7) were fortunately very suitable for such low-level measurements.

The properties of the contact between metal dots and oxide crossbar electrodes have to be measured carefully, because such contacts are in principle known to change their properties when current passes through them. This is the conventional metal-insulator-metal resistive switching phenomenon. Such changes could be mixed up with changes of the crossbar region itself. It turned out that the contacts were large and conducting enough so that such effects did not play a role in practice. It is however still important to make sure that the electrodes themselves exhibit ohmic resistance without any non-linear effects that could hint at contact influences.

The main types of measurements were the precise determination of characteristic

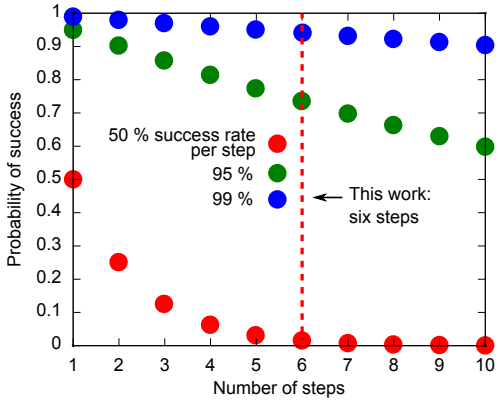


Figure 3.9: The probability that the production of a sample ultimately succeeds decreases with the number of steps. To make samples that require many steps, the success rate per step must be high in order to have a good probability to succeed ultimately.

curves for dielectric, channel, gate and contacts; the response of dielectric, channel, gate, and partially also contacts to write pulses of varying strength and duration; and the drifting behavior of channel and gate after a strong write pulse. They could realistically not be performed or evaluated manually, so computer programs were developed for these purposes (Section 4.8).

Temperature is an important parameter in all the equations for ionic transport and semiconductor junction behavior. It has furthermore a strong influence on the conductivity of the used materials. Some experiments were therefore performed at low temperature, down to liquid helium. The setup was however not suitable to stabilize the temperature at an arbitrary value other than the boiling point of liquid helium or liquid nitrogen. At other temperatures, measurements could only be performed while warming up slowly. Measurements in a physical property measurement system for low temperatures were planned, but not performed because the available time was not sufficient.

# Chapter 4

# Materials and Methods

A significant amount of time was spent on three more technical aspects that were critical for this thesis: Preparation of high-quality films with high-pressure oxygen sputtering (Section 4.1; chemical etching and subsequent surface treatment for perfect epitaxy (Section 4.5); and developing the measurement setup, control software and data analysis software (Sections 4.7 and 4.8). These sections are therefore quite long and contain a lot of original work. The implementation of the software is not described in great detail, because going into the depths of software engineering would be out of the scope of this thesis. The source code and data structures are developed to be easily understandable. An interested reader is therefore encouraged to have a look there.

The methods for film characterization, the substrates and the lithography processes are only described in short for reference, because no particular innovations were necessary here.

## 4.1 Depositing high-quality oxide thin films with high-pressure oxygen sputtering

The oxygen sputter process for oxides is fortunately insensitive to the most common contaminants in vacuum systems – oxygen, nitrogen, water, hydrogen, hydrocarbons. Oxygen and nitrogen are no problem because oxygen is present in excess anyway and nitrogen is hardly incorporated into the film if oxygen is available. The oxides may form hydroxides with water, but at the high deposition temperature these hydroxides decompose and the equilibrium is on the side of water in the gas phase and solid oxide. The same is true for carbon dioxide, with some exceptions of stable carbonates like $BaCO_3$. Hydrocarbons, carbon or hydrogen are quickly oxidized to carbon dioxide and water.

Volatile metal oxides that are deposited on hot parts, like the oven, can however disturb deposition when they recondensate on the substrate. A designated frame around the substrate for such potentially volatile oxides can protect the oven from too much deposition. Frame and oven should furthermore be annealed without a substrate at the maximum temperature possible under high vacuum for an hour. This treatment evaporates the volatiles as far as possible. They are either deposited permanently on the cold chamber walls, or they are pumped out of the vacuum chamber.

The best film quality was obtained when the substrate was heated quickly to the maximum temperature in high vacuum prior to deposition and then cooled to the deposition temperature at a relatively high oxygen pressure of 100 mbar. This is supposed to evaporate all volatile contaminants from the surface and then oxidize eventual carbon residues and resupply oxygen to the substrate or film.

The films can be annealed at higher oxygen pressure after deposition in order to saturate them with oxygen. Care should be taken with hot metal parts in pure oxygen: Metals that passivate on air and remain stable may react violently with pure oxygen, for example titanium [86]. In air, the nitrogen slows down the reaction because it enriches in the reaction zone, takes up reaction heat through its heat capacity and has to be eliminated by diffusion or convection.[1] In pure oxygen and in the case of a solid or liquid reaction product (oxide), the oxygen influx is limited only by the gas pressure and the sound velocity. Once the temperature is hot enough for the passivating oxide to melt or degrade otherwise, the reaction will proceed violently.

The sputter target should only be switched on for pre-sputtering once the substrate has reached the deposition temperature. As the machine has no shutter, traces of material may be deposited on the substrate during presputtering. If the substrate is cold, this layer will be amorphous and can disturb subsequent film growth.

The machines that were used to grow the films are sensitive to cross-contamination of the targets. The burning target may deposit a film on neighboring targets. For the second-generation devices, unused targets were therefore covered with aluminum foil and later target covers. The pre-sputter time until stable deposition conditions were reached could be brought down to only 10 minutes with this measure.

### 4.1.1 Preparing sputter targets

The sputter targets are ceramic discs of 50 mm diameter and a thickness of a few millimeters. They are manufactured with a specified composition by commercial vendors. At first, targets were ordered from SurfaceNet, but this company failed to produce the targets with the correct stoichiometry and purity in several cases. Later, the targets were ordered from Lesker where no such problems occurred so far. After it became apparent that the target composition might be out of specifications, each target was checked with X-ray fluorescence and in some cases with inductively coupled plasma optical emission spectrometry (ICP-OES) by the central department for chemical analysis (ZCH) in the center before the target was mounted.

The target has to be attached mechanically and coupled electrically and thermally with a metallic target holder. Insulating targets for RF sputtering can be coupled capacitively and conducting targets for DC sputtering have to be coupled conductively. This connection between target holder and target disc is critical for the target to operate. It has to be vacuum-safe, stable at somewhat elevated temperature, and resistant to progressing oxidation by the oxygen plasma. This excludes many glues and resins.

The connection also has to be mechanically strong and resistant to fatigue: The target disc is heated on one side by the plasma and thermal radiation from the

[1] Many base metals like for example titanium do form nitrides in an exothermic reaction, but these nitrides are usually not thermodynamically stable at the extreme temperatures of a metal fire.

hot oven with a power of at least 80 W. With the other side it is attached to the water-cooled target holder. This causes the target to expand and shrink relative to the target holder each time the target is switched on and off. If the connection between target and holder is too strong and stiff, the target may crack. If the target does not adhere to the holder strongly enough, it may delaminated progressively. This process reduces the electrical and thermal contact and therefore accelerates the delamination, because the temperature difference between target disc and target holder increases.

Traditionally, the targets were mounted by first sputtering a thin silver layer on one side, then spreading a silver paste on the surface and finally burning in the sputtered layer and silver paste at high temperature to remove the organic binder, sinter the silver particles together and create an intimate connection between ceramic target and metal coating. The silver surface can then be soldered to the metallic target holder with conventional tin-silver solder. It is important to use solder without flux, because the flux may corrode or contaminate the target. This method only works for oxides that have a chemical affinity for silver, namely LCO or YBCO. Most other oxides do not bond firmly with this method, and even LCO is prone to delaminate or crack over time. The tin-silver solder is designed to be mechanically hard to prevent creep of soldered connections in electronic circuits. The melting point of the solder is furthermore above 200 °C. The targets crack therefore easily when bonded with this method, either already during the bonding process or when the target is operating.

RF targets can also be glued with Torr Seal, a high-vacuum glue. It seems to contain a ceramic filler which passivates the surface against oxidation by the oxygen plasma. The adhesion of this glue to metals and ceramics is very good. Only some cracking was observed after longer target operation times.

Finally, the targets can be soldered directly with indium using an ultrasonic soldering iron. The ultrasound breaks the thin passivating oxide skin of the reactive indium melt and brings the indium metal in direct contact with the surface to be soldered. The indium metal then reacts with the exposed oxide or metal and bonds very firmly with virtually all oxides, as well as the gilded target holders. Pure indium and particularly indium oxide have a low vapor pressure and are therefore unproblematic in a vacuum system. Indium is furthermore very, very soft, almost like wax, and creeps rapidly even at room temperature. Mechanical stress between target holder and ceramic disc is thus relaxed. This makes indium soldering in my opinion the ideal target bonding method. So far no target that was bonded with indium has failed during my work.

A new target then needs to be pre-sputtered for many hours until it is conditioned and provides stable deposition parameters. This process can be monitored in the case of DC targets by the sputter voltage relative to current and gas pressure. A new target usually only operates at high voltage at lower pressure (1 mbar) and low current (20 mA). The voltage then drops gradually and consequently pressure and current can be increased. 3 mbar and 200 mA are typical values. The ultimate voltage depends on the target. At 3 mbar, YBCO and LCO targets operate at low voltages (below 300 V), while LSMO reaches about 380 V and SRO is close to 400 V. The sputter voltage is very sensitive to contamination of the plasma: Traces of Ru from evaporating $RuO_2$, or traces of Mn from LSMO contamination on the LCO target were observed to increase the sputter voltage of the LCO target significantly, reaching almost 400 V. My guess is that metal ions with many oxidation states, like

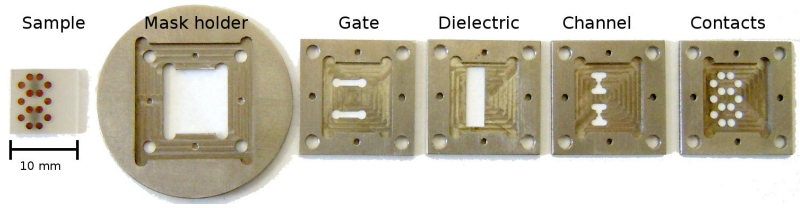


Figure 4.1: Substrate, frame and shadow masks. The masks were not used yet and are therefore still shiny.

Mn or Ru, catch electrons from the plasma and therefore reduce the electron lifetime and ionization yield. A higher voltage is therefore necessary to maintain a constant ionization rate, i.e. a constant sputter current.

The sputter voltage also increases if the contact between target disc and target holder is not good: The current is then usually concentrated in some area of the target and the higher serial resistance causes a higher voltage.

A stable sputter voltage under constant conditions is therefore a good indicator for a stable, clean deposition process.

### Structuring with shadow masks

The substrate can be covered with a mask during sputtering. Material is then deposited only through the openings in the mask. The mask can be aligned with a suitable frame around the substrate and a structure can be built up by depositing different material through a series of different masks (Fig. 4.1). This method works for all materials and does not rely on any etching. The substrate is exposed to ambient conditions only for a few minutes when the mask is changed. This method is therefore also suitable for films that are sensitive to moist air, like LCO. The mask has to be very close to the substrate, but shouldn't touch it to keep the substrate surface clean. The mask material should furthermore be mechanically stable enough and be resistant to oxygen at the high deposition temperature. The first generation of masks were made of titanium, but this metal does not passivate itself reliably at the deposition temperature. The oxide skin grows gradually and releases a lot of particles (scaling).

Kanthal, a family of iron-based alloys for heating elements, is very resistant to scaling on air even at higher temperature up to about 1400 °C, depending on the formulation. The parts have to be passivated by annealing on air at high temperature (1050 °C) once. After this treatment they are stable under sputtering conditions and also in high vacuum. No particles are released. The masks and frames should nevertheless be cleaned on a regular basis in water with isopropanol and dish soap[2], acetone and

[2]Organic solvents are not very suitable to remove inorganic particles. The key is to keep such particles in suspension and prevent them from reattaching. This is achieved by charging the particle surface. They are then repelled by other particles and also surfaces with equal charge. This works better in water, because it solvates ionic species exceptionally well. The charge can either be created by choosing a proper pH where acidic or basic groups on the particle surface are dissociated, or by specific additives that attach themselves to the particle surface. Detergents, like in common household cleaners, are particularly effective for this. An ultrasonic treatment in a mixture of roughly 100 parts water, 10 parts isopropanol and 1 part dish soap is very effective against organic

isopropanol to remove any particulates. The masks should be heated out before the next deposition to remove volatile contaminants from the cleaning process.

The deposition rate through the mask turned out to be up to a factor of three slower than without the mask. The thickness of the structures is furthermore not uniform, but rather mound-shaped with very shallow slopes. It was hard to tell how far the deposition reaches under the mask. The mask would have to be positioned directly on the substrate to prevent this. Shadow masks are therefore not suitable if well-defined structures with several deposition steps are desired. The resolution and alignment precision of this technique is limited. Photolithography was therefore used to create the miniaturized second-generation devices.

## 4.2 AFM

The AFM is an invaluable tool to quickly check the surface topography of a sample non-destructively on the nanoscale. A smooth surface without precipitates indicates a good layer. Large grains hint at bad epitaxy, and particles may result from insufficient cleaning or contamination during/after the deposition process.

The method works by scanning a very sharp tip over a surface at a very close distance. Various different modes are known, of which the "tapping mode" is the most widely used. This mode will be described in the following, because it was used exclusively in the work for this thesis. More details about this well-established technique can be found in many textbooks. Here, only the aspects with relevance for this work are described.

The tip sits at the end of a vibrating cantilever with an intrinsic resonance frequency. An external drive excites the cantilever oscillation. If the tip is getting very close to a surface, the interaction between tip and surface (van der Waals forces and other) shifts the resonance frequency and therefore the vibration amplitude and phase at a given excitation frequency. Minimal plastic deformations of the substrate may also dampen the vibration. These changes of the vibration properties can be detected with high sensitivity. The tip is kept at a constant distance to the substrate (z direction) by a piezo element. The z signal is created by a feedback loop that keeps the vibration amplitude constant. This z signal is recorded as a function of the tip position, yielding a height map of the substrate.

### 4.2.1 Used devices

An SiS Picostation was used for most AFM analysis. An Agilent AFM with an aiming camera was used to take AFM images of specific sample regions, for example to check the result of lithographic structuring.

### 4.2.2 Typical problems

The tip has to come very closely to the substrate, but should never touch it. Otherwise it degrades. The feedback loop has to react very quickly to changes of the amplitude if the scan is fast or if there are steep topographic features on the surface. The two

and inorganic dirt. It may however leave a surface layer of detergent even after rinsing.

control parameters of the feedback loop, integration time and proportional factor, have to be "aggressive" in this case. But this increases noise, and at some point the system may start to oscillate. Scan speed and feedback parameters should therefore be chosen correctly for different samples: Slow scan and aggressive feedback for rough samples, fast scan and slow feedback for smooth samples. The tip is typically scanned forwards and backwards on one line, and the difference between the two traces should be below one nanometer at each point. The tip is in danger and the topography is inaccurate if the two traces differ too much at a sharp feature.

An AFM does not take a true image of the surface, but records a convolution of the tip with the surface. A blunt or deformed tip distorts the image. Shallow features, like atomic terraces, may be blurred out, and sharp, point-like features produce an image of the tip. The same pattern (the tip image) repeats at each sharp feature of the sample. The tip has to be replaced in this case.

## 4.3 X-ray diffraction and X-ray reflectivity

X-ray diffraction (XRD) was used to investigate the crystal structure of materials. X-ray reflectivity (XRR) was routinely used to measure the film thickness and roughness. The sample does not have to be prepared in a specific way, but can be mounted directly and is not damaged in the process. The fundamental details will not be explained here, as the methods are very established and described in many textbooks. Only the aspects relevant for this work will be described.

A Pananalyticsl MRD Pro diffractometer was used. The thickness was measured with XRR by fitting the fringe pattern of a low-angle scan to a physical model of the layer stack. The precision is in the percent range and only the density and composition of substrate and layer(s) are required as input parameters.

XRD was used to verify that a material grew in the desired phase and orientation. Bad epitaxy would manifest itself as roughness in the AFM images and XRR scans, as well as additional peaks from misaligned grains in XRD data. Usually, a $2\Theta$-$\omega$ scan was performed. The substrates were aligned such that a crystal plane of the substrate that was nearly parallel with the substrate surface was in Bragg condition. In almost all cases this was the (0 0 1) plane for cubic resp. the equivalent (1 1 0) plane for orthorhombic perovskite substrates. An epitaxial layer can be expected to be in Bragg condition as well with this alignment, because it follows the crystal structure of the substrate. It is possible to get information on structural defects in the layers by performing an $\omega$ scan at a Bragg peak of the epitaxial layer. Peak broadening means that the crystal planes do not all have the same orientation, but that the orientation varies. This implies a high density of low-angle grain boundaries and dislocations. Such information may be relevant in the future, if the influence of such structural defects on the transport properties is to be investigated.

It would be possible to measure stress and strain in the epitaxial layers with this method, but this did not appear to be relevant for this work at the current level. The primary concern were smooth, uniform epitaxial layers of the correct phase with known thickness. This is at a first level sufficient to fabricate functioning samples with more or less reproducible properties and was difficult enough to achieve in heteroepitaxial multilayer systems with intermittent lithographic structuring. The

influence of crystallographic orientation, strain and structural defects can maybe be investigated in the future (see also Appendix B).

## 4.4 Substrates and substrate termination

STO single crystalline substrates in (100)k orientation from Crystec, Berlin were used for most experiments. $NdGaO_3$ (NGO) substrates from the same vendor were used for some tests. It is more difficult to judge if an etching process is complete due to the strong color of NGO. STO furthermore becomes slightly conductive during ion beam etching and TEM sample preparation, which helps against charging problems. Unterminated substrates were used for the first-generation devices. For the etching tests and second-generation devices, the substrates were terminated with ammonia-buffered hydrofluoric acid (BHF) at a pH of 6.5. The substrates were first cleaned with ultrasound in acetone and isopropanol. Then they were submerged for 3:45 min in the BHF solution. After rinsing twice with deionized water, they were cleaned again with ultrasound in acetone and isopropanol. AFM images confirm the high quality of the surface after this treatment with atomic terraces and without particles.

## 4.5 Chemical etching of LSMO, SRO and LCO

A patent application [13] was filed for the approach to chemical etching of mixed oxides with oxidation or reduction. The exact etching procedures for LSMO and SRO are published in a paper [14].

Heterostructures of epitaxial oxides are nowadays mostly produced by first depositing a multilayer on a substrate and then milling or etching the structure out of this multilayer. In simple cases only argon milling is used, and in more advanced cases also chemical etchants [87]. The metal contacts are finally added with lift-off. An all-oxide crossbar structure like required here is not attainable with this approach. It is mandatory that bottom electrode, dielectric and top electrode are structured separately to get a good edge insulation of the crossbar. This means that epitaxial layers have to be deposited after a layer underneath is structured.

Ion beam etching damages the underlying surface to such a degree that subsequent films do not grow epitaxially or are rich in defects. It is therefore mandatory to use chemical etchants in all cases where high-quality films have to be grown on an etched surface or edge. Chemical etchants can be selective to a specific material or group of materials, but they also have to be developed individually. The different approaches that were tried for LSMO, SRO and LCO will be described together with the respective results in the following. The etchants and etching procedure had to be optimized substantially in order to give surfaces that are ready for epitaxial deposition.

### 4.5.1 Route of attack

As lined out in Sections 2.3 and 2.4 and Table 2.2, the chemistry of a perovskite or related compound is often similar to the chemistry of the pure B-site oxide with the

same oxidation number. For LSMO this would be $MnO_2$, for SRO $RuO_2$ and for LCO CuO. Pourbaix diagrams [88] of the relevant elements can help to understand the chemistry as a function of pH and redox potential. They show which chemical species is predominant under the given conditions. A metal oxide can at least theoretically be etched with a medium in which a soluble form of the metal will be predominant. Such diagrams can be calculated from tabulated thermodynamic data of relevant compounds with a software like Medusa [89]. They have to be interpreted with caution, because the results depend very much on the accuracy and completeness of the database, and they only describe the thermodynamic equilibrium, not the reaction speed.

The general criteria for chemical etchants described in Section 2.4 were used to identify viable attack routes and to choose candidate etching solutions. The best match to these criteria was then chosen for future work.

### 4.5.2 SRO

SRO has in practice not been etched chemically because it is not attacked by acids or by bases. Ruthenium has however a rich chemistry with no less than eight possible oxidation numbers. Entire books are written about ruthenium coordination chemistry. There should be some way to exploit this for etching. Oxidizing could theoretically transform $RuO_2$ to a more soluble ruthenium compound, for example $RuO_4$ or $RuO_4^{2-}$. Etching of SRO by oxidation with ozone has already been patented [90, 91], but using ozone seemed impractical. It turned out that $RuO_2$ is oxidized to $RuO_4$ by a number of strong oxidizers [92]. Those reactions are used to prepare soluble and volatile $RuO_4$ as a reagent for organic chemistry. Reduction seems less promising because the end product could easily be Ru metal according to the Pourbaix diagram (Fig. 4.2).

Several of the candidates listed in the book by Griffith [92] that were expected to not leave residues and are safe enough to handle were tried out with SRO and behaved as expected (Table 4.1). $NaIO_4$ was chosen for later work because it has a suitable etch rate and near-neutral pH. The Pourbaix diagrams of Ru and I suggest that the etchant should work over a wide pH range (Fig. 4.2). The reaction equation is

$$SrRuO_3 + 2\,H_3O^+ + 2\,IO_4^- \longrightarrow Sr^{2+} + RuO_4 + 3\,H_2O + 2\,IO_3^- \qquad (4.1)$$

### 4.5.3 LSMO

For LSMO, several etchants were documented in the literature [93–96], but the etching mechanism were not discussed. Concentrated HCl and 15 % HCl gave very different results: The concentrated acid etches rapidly and without residues, while the half-concentrated acid acts slowly and leaves a brown residue behind, presumably $MnO_2$. The Mn has partly the oxidation number (III) in LSMO, but Mn(III) is unstable in an aqueous environment and disproportionates to soluble Mn(II) and $MnO_2$. This would explain the partial etch with $MnO_2$ residues by a diluted acid. From relating the known etchants to the chemistry of $MnO_2$ it became clear that reduction of Mn(IV) to Mn(II) is the key to attack this material without leaving residues. Concentrated HCl can be oxidized to $Cl_2$ by $MnO_2$ and is therefore in

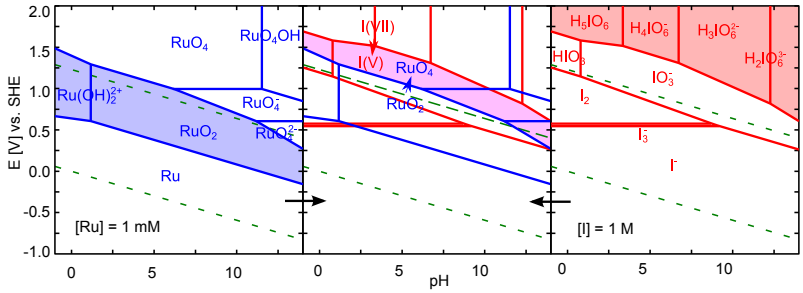


Figure 4.2: Pourbaix diagram of ruthenium and iodine. The oxidation of $RuO_2$ (blue area) to $RuO_4$ by periodate (red area) proceeds in the region marked in the center and is driven by the difference in redox potential. Calculated with Medusa [89].

Table 4.1: Results of experiments to choose suitable etchants for SRO. Solvent is water if not otherwise stated. The etchant printed in bold face was chosen for later work.

| **Etchant** | **Etch rate** | **Remarks** |
|---|---|---|
| 10.9 % $[Ce(NO_3)_6](NH_4)_2$, 4.25 % $HClO_4$ (commercial chromium etchant) | > 100 nm/s | Particles or precipitates on surface |
| 0.4 mol/l $H_5IO_6$ | 20 nm/s | |
| **0.4 mol/l $NaIO_4$** | **2 nm/s** | |
| 0.4 mol/l $NaClO_4$ | No effect | |
| 0.4 mol/l $NaClO_3$ | Very slowly | |
| 0.05 mol/l $H_5IO_6$, 0.01 mol/l 18-crown-6 in ethanol | No effect | Periodate might oxidize ethanol. |

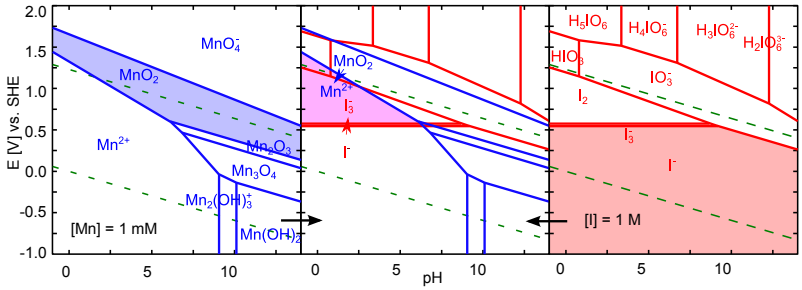


Figure 4.3: Pourbaix diagram of manganese and iodine. The reduction of $MnO_2$ (blue area) to $Mn^{2+}$ by iodide (red area) can proceed in the area marked in the center. The driving force for this reaction increases at lower pH, because the reaction consumes many protons (compare Eq. (4.2)). Calculated with Medusa [89].

principle a suitable etchant. It does however create particles on STO surfaces, presumably by leaching $Sr^{2+}$ and leaving $TiO_2$ or the corresponding hydroxide behind. An etchant that works at higher pH was therefore desirable.

Ascorbic acid as a well-known and safe reducing agent was tried out, but it turned out that the reduction does not progress at a reasonable speed. Instead, the reaction leaves $MnO_2$ residues similar to diluted HCl. The Pourbaix diagram of Mn (Fig. 4.3) reveals that the oxidizing power of $MnO_2$ increases strongly at lower pH. An acidic iodide solution, similar to the one used by Lee and Hwang [94], worked well at an estimated pH of 1 (Eq. (4.2)). An oxidation product of $I^-$, $I_3^-$, caused a brown coloration. Ascorbic acid was therefore added to reduce the $I_3^-$ back to $I^-$, forming dehydroascorbic acid (Eq. (4.3)).

$$\begin{aligned} 3\,La_{2/3}Sr_{1/3}MnO_3 + 18\,H_3O^+ + 6\,I^- \longrightarrow \\ 2\,La^{3+} + Sr^{2+} + 3\,Mn^{2+} + 27\,H_2O + 2\,I_3^- \end{aligned} \tag{4.2}$$

$$2\,I_3^- + 2\,C_6H_8O_6 + 4\,H_2O \longrightarrow 6\,I^- + 2\,C_6H_6O_6 + 4\,H_3O^+ \tag{4.3}$$

The results of various tests with potential LSMO etchants are listed in Table 4.2.

### 4.5.4 LCO

LCO is easily attacked or degraded by acids, including water. Etching it in such a way that no residues are left and the surface is not degraded is therefore difficult: Water-based etchants and rinsing leave hydroxides behind. An aged solution of bromine in ethanol can be used for YBCO [68, 69] and allegedly also works for the chemically similar LCO. This solution does not contain any elemental bromine after aging, but rather hydrobromic acid and acetic acid [70]. Unfortunately, it is quite dangerous to handle pure bromine. A solution of 1 % methanesulfonic acid in ethanol was therefore tried out and etched YBCO as expected. Methanesulfonic acid is like hydrobromic acid a strong acid that also dissociates in many organic solvents and forms salts that have good solubility in water and organic solvents. It is in my opinion much safer and predictable than the aged bromine solution. For etching LCO, a 1:1 mixture by volume of methanesulfonic acid and isopropanol was

Table 4.2: Results of experiments to choose suitable etchants for LSMO. Solvent is water if not otherwise stated. The etch rate is to be understood as an approximate value because at least 15 s over-etching is necessary to remove the last residuals of a layer. The etchant printed in bold face was chosen for later work.

| Etchant | Etch rate | Remarks |
|---|---|---|
| 37 wt-% HCl | 7 nm/s | Precipitates on surface |
| 15 wt-% HCl | Very slow | Brown haze, dirty surface |
| Saturated citric acid at 85°C | 0.2 nm/s | Residuals |
| 0.37 % HCl, 5 mol/l KI | 6 nm/s | Solution turns brown in air ($I^-$ oxidized to $I_3^-$ by $O_2$) |
| 3.7 % HCl, 5 mol/l KI | 28 nm/s | Solution turns brown in air |
| **0.37 % HCl, 5 mol/l KI, 0.1 mol/l ascorbic acid** | **6 nm/s** | **Solution remains clear** |
| 1 mol/l ascorbic acid, 0.01 mol/l EDTA, 1.05 mol/l $NH_3$ (pH 4) | Very slow | Brown haze, poor surface |
| Saturated ascorbic acid, 0.01 mol/l 18-crown-6 in ethanol | No effect | |
| 1 % methanesulfonic acid, 1 % glutaraldehyde, 1 % $H_2O$, 0.01 mol/l 18-crown-6 in ethanol | Very slow | Brown haze, poor surface |

finally used. This mixture does not attack PMMA resist, but etches LCO with about 46 nm/min.

A suitable rinsing procedure for LCO had to be developed as well, as outlined in Section 2.4.3. The sample was rinsed twice with dimethyl sulfoxide (DMSO) to wash off the acid. DMSO solves isopropanol, methanesulfonic acid and water and is generally a good organic solvent for ionic species, such as oxide etching products and other contaminants of the acid. At the same time it does not dissolve PMMA: The very fine and sensitive LCO structure is thus not exposed to the rinsing solution that is contaminated with acid carryover. In the next step, the PMMA was stripped with ample acetone and ultrasonication followed by rubbing. This further dilutes traces of the acid and removes particles. A short ultrasonication and rub in DMSO followed to remove any ionic surface contamination that would not be soluble in acetone. The last rinsing step was rubbing and ultrasonication in isopropanol, because this solvent is particularly suitable to blow the samples dry.

### 4.5.5 Surface quality

The etched surfaces are covered with small particles even if the etching was complete. "$TiO_2$" from leaching of $Sr_2^+$ out of STO, or insoluble impurities of the film are likely culprits. It was tried out to work at near-neutral pH, but even there particles occurred. Tests with etchants based on organic solvents were limited and not successful for LSMO and SRO, because the solvent should not attack PMMA resists. Unfortunately I only found out at the end that DMSO does not attack PMMA resist. DMSO would have been a very promising solvent for ionic species. Normal novolak-based photoresist is less stable than PMMA against organic solvents. The way I took

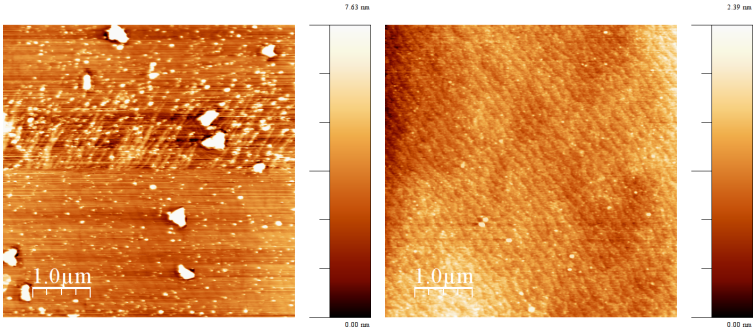


(a) Before rubbing (b) After rubbing

Figure 4.4: Rubbing removes particles from an NGO surface that was degraded by contact with the strongly acidic commercial chromium etch during an SRO etching experiment. Images: Y. Chen

was therefore to remove particles as far as possible and prevent new particles from forming.

The samples were rubbed with a cotton swab inside ethanol directly after etching and rinsing in water. It is important that the sample surface does not become dry between etching and rubbing, because this hardens and attaches the floccose "oxide" particles. They are difficult to remove once they are dried. This is a hint that the particles are at first a hydroxide derivative and then lose water gradually to form an oxide, which crosslinks and hardens the particles. The effect of rubbing is shown in Fig. 4.4.

The samples were treated with ultrasound and rubbed again in acetone and isopropanol directly before being inserted into the chamber to remove last particles or contamination. The heating protocol prior to deposition (Section 4.1) was designed to further remove last traces of contaminants. The next layers then grew on the treated surface like on pristine substrates (Fig. 4.5).

## 4.6 Photolithography

Photolithography was used to create the second-generation devices with smaller structures. The resist AZ 5214E was used for positive and negative tone. The positive process was used for etching and the negative process for metal lift-off. In both cases the metal structures on the photo mask are the final structures on the sample.

Samples were first cleaned with a three-minute ultrasonic treatment in acetone and isopropanol, then baked out for three minutes at 180 °C and cooled for about 30 s on a cold surface. The resist was spun on at 4000 rpm and baked for 5 min at 90 °C. Exposure time for positive-tone processes was about 50 s and for negative-tone 18 s. The samples were baked for 45 s at 120 °C and then flood-exposed for 3 min for image reversal in the case of negative-tone processing.

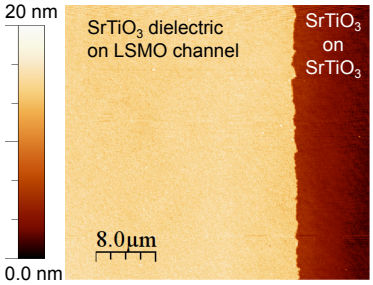


(a) Growth of STO dielectric over the LSMO channel. The step on the edge is abrupt without any irregularities.

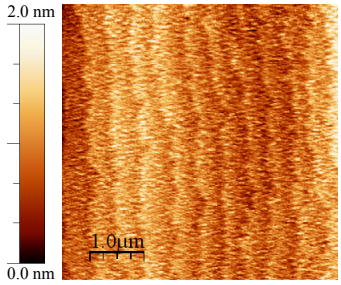


(b) Growth of STO on an STO substrate surface where an SRO and an LSMO layer have been etched away.

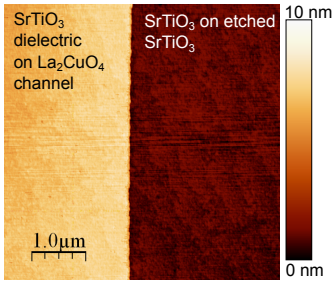


(c) Growth of STO dielectric over LCO channel. Note the atomic terraces on the entire surface, indicating perfect epitaxy on structure, edge and substrate.

Figure 4.5: Growth of the STO dielectric on etched surfaces and structures.

The samples were developed for about 85 s in the TMAH-based developer AZ 326 MIF and rinsed in deionized water. Finally, they were blown dry.

PMMA resist and exposure with UV radiation in the region of 250 nm was used for water-free etching processes. After the same cleaning procedure as for AZ 5214E, the resist Allresist AR-P 639.04 was spun on at 4000 rpm and baked out for 3 min at 180 °C. It was exposed for 120 s at about 7.5 mW/cm² and then developed for 2 min in Allresist AR 600-55. The development was stopped by immersion in isopropanol for 1 min and blowing dry. Resist residuals in the exposed regions were removed prior to chemical etching with 30 s of oxygen plasma in a Tepla 300 plasma processor at 300 W power, 200 sccm $O_2$ flow and a pressure of about 0.7 mbar.

## 4.7 Setup for electrical measurements

The electrical measurements were performed in a custom setup (Fig. 4.6) that I adapted for my samples. A Keithley 6221 DC and AC current source together with a Keithley 2182A Nanovoltmeter were used to generate and measure electrical signals. A Keithley 7001 Switch System with a Keithley 7111-S quad 1x10 multiplexing card were used to switch between different channels and devices. The temperature was monitored with a Correge Pt100 DIN 1/10 class platinum resistance thermometer and a Keithley 195 system digital multimeter in four-point geometry. A reference "dummy" sample (Fig. 4.7) was used to verify the measurement results.

The sample capsule could be inserted into a dewar with liquid nitrogen or liquid helium to measure at low temperatures. Pt100 thermometers are well-characterized down to -200 °C and the standard formula to convert resistance to temperature was used. In order to perform a few measurements below that temperature, the Grüneisen formula for the low-temperature resistivity of metals was used instead. It was calibrated to give the same value and slope as the standard formula for Pt resistance thermometers at -200 °C. The residual low-temperature resistance was estimated by immersing the sample capsule in liquid helium and measuring the lowest resistance attainable. The temperature measurements below -200 °C are therefore not as precise as the measurements above -200 °C.

## 4.8 Software for measurements and data processing

First semi-automatic measurements revealed a systematic conductance change of the channel as a function of write time. These measurements were so complex, error-prone and time-consuming that only a fully automated measurement system would allow to perform all necessary tests with sufficient efficiency and reliability on a larger number of samples.

The data is so complex that it is impractical to evaluate it by hand. A separate data processing program was therefore written to explore the data and present them in a meaningful way. Selected data for publication can be extracted with that software to create high-quality figures with other tools.

More details on the software can be found in Appendix A.

### 4.8.1 Requirements for the measurement software

The software should run unattended and perform the measurements without human interaction. It should automate as many aspects as possible to eliminate human error and save time. The software should constantly save the data to keep results even in case of a failure. The complete raw, unprocessed data from the measurement devices should be saved. The instrument settings and the way the measurements are performed should be clearly documented – including the measurement software itself. The raw data should be saved in a format that is both human-readable and computer-readable. The data format should be easily read on different systems and with different programming languages. It should be flexible enough to accommodate new types of measurements and complex data structures. It should be 100 % clear from the data files which data is stored in which field so that no columns or units can be mixed up. That means the data format should be self-explaining as far as possible.

The software should never accidentally change or delete data. Data should be backed up regularly on a different computer. It should be possible to measure different samples on different systems at the same time without causing a collision. The separate measurements should be easy to merge without any risk of deleting or overwriting data. Any change to the data after the measurements are performed, such as corrections, should be clearly documented and exactly replicable.

### 4.8.2 Requirements for the data processing software

The data produced by the measurement program are rich and detailed, but also complex and voluminous. Interpreting it by hand, in the sense of using a spreadsheet software or generic plotting software, is impractical. Just to illustrate this: At the time that I am writing this, there are data of 542 measurement runs on 46 samples stored in the repository. Each measurement can be huge: One single normal test of the conductance change as a function of write time and write current contains around 50.000 to 150.000 individual numerical values in around 2000 files. The risk of mixing up or deleting data would be high without a stringent management and clear presentation of the data.

A tailored software with a graphical user interface had to be developed to browse and interpret the data with minimum effort. The data should be displayed and processed numerically in many different ways and it should be relatively easy to add new ways of interpreting the data to the software.

### 4.8.3 Choice of programming language and platform

The software was written in Python [97] because this language is free software [98], is supported on a wide range of platforms, has a large user base for scientific and numerical applications, comes with high-quality libraries for various purposes, including fast numerical and scientific libraries (SciPy [99], matplotlib [100]), and allows high-level programming with compact and elegant code and rapid development cycles, as well as low-level system programming. Python is in my opinion the most versatile and well-designed language today.

A programming environment like LabVIEW [101], which is often used to control measurement devices, seems to be a simpler choice. It is however a commercial product from a single vendor. The software would be impossible to use without a LabVIEW license and one is completely dependent of this vendor and it's development and release policy. With Python, one has unlimited access to the source code, including the right to modify and redistribute it under certain terms and conditions, and can install all required software on any system without any restrictions, apart from technical ones. A Python interpreter is in fact pre-installed on virtually all desktop or server Linux systems.

Furthermore, LabVIEW is a single-domain product, only developed to control measurement devices. Other functionality is only implemented rudimentarily. Python is in contrast a general-purpose language. This means that a wide range of standard tasks, like parsing common file formats, network access, graphical user interfaces and so on, are very easy with Python. Furthermore, virtually all things that can be done with a programming language are possible in Python, although some low-level things may be a bit more difficult.

The visual programming paradigm of LabVIEW is rather different from common programming languages and in my opinion not so suitable for larger, complex software. Python is sufficiently similar to other common programming languages. This means I could quickly learn it, although it was new to me. Established "good practices" from other programming languages apply directly to Python. It combines different programming paradigms (procedural, object-oriented, functional, aspect-oriented), is suitable both for simple scripts or even command-line use, and for very large projects of almost any kind. It is therefore the language of choice for me, especially when compared to LabVIEW. Learning Python gives a bigger benefit to me than learning LabVIEW.

I chose Linux as a platform because I am very familiar with it and it is in my opinion more reliable and flexible than Windows. Drivers had to be developed for the various instruments. This was not a big problem because the instrument interfaces were easy to program on Linux and were clearly documented. All raw low-level commands that are issued to the instruments can be logged and controlled from these custom drivers, which helped a lot with debugging.

The source code is managed in a Subversion [102] repository to keep track of all changes and generally help with the source management. The graphical user interface was implemented with with wxPython [103], the Python binding for the wxWidgets GUI toolkit, and with matplotlib [100] to visualize data interactively.

Details about the implementation can be found in Appendix A.

### 4.8.4 Validation and debugging

The setup and software were validated by measuring a "dummy" sample (Fig. 4.7) that imitates the electrical network of a real sample (Fig. 3.3) with a number of high-quality resistors and a capacitor. The values of the resistors and the correct connection of the different channels with the device were checked by using a multimeter and comparing the results with the output of the measurement program. Test runs verified that the dummy sample does not change properties upon reading and writing. The measured results of the dummy sample were always the same within the instrumental resolutions as the results measured with a multimeter.

The the dummy sample was helpful for testing and debugging, too. The operation of the setup and software could be verified after changes without putting a real sample at risk. Particularly temperature-controlled routines could be tested easily with the adjustable resistor that is used in the place of the resistance thermometer of the real sample holder.

### 4.8.5 Evaluation

In conclusion, the measurement software fulfills all requirements and has proven to be most useful. It is flexible enough so that new types of measurements are easy to implement, and no data has been lost or mixed up so far. Once all bugs and quirks were ironed out, it could perform measurements with minimal interaction and choose good default parameters for the measurements automatically. The software would sometimes run for days performing measurements.

The data processing software gives access to the results with ease. Comparing measurements or extracting various relevant information from a measurement is a matter of a few clicks.

The methodical development process by first defining requirements, then choosing tools and platform accordingly, designing the data structure, defining the overall architecture of the software and only in the end implementing and testing the details step-by-step gave predictably a functioning software within a reasonable development time. The software turned out to be easy to debug, maintain, adapt and extend, because it is based on proven, established technology and has a clean, modular structure (see also Appendix A).

(a) Sample holder with outer cover.

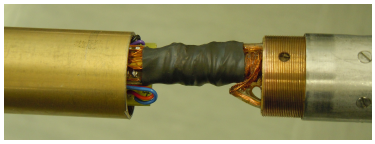

(b) The outer cover is screwed off

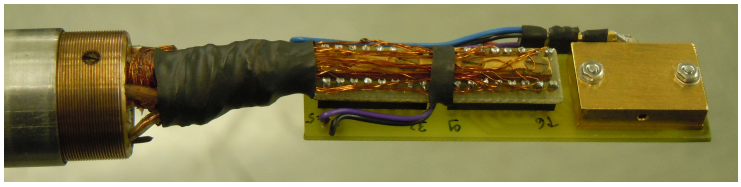

(c) Sample holder with wire connections to the left, plug in the center and covered sample receptacle to the right.

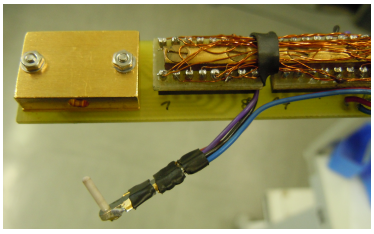

(d) Sample receptacle with Pt100 resistance thermometer removed.

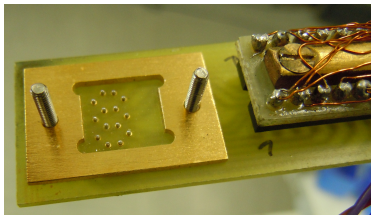

(e) Heat spreader removed: contact pins that match the sample layout.

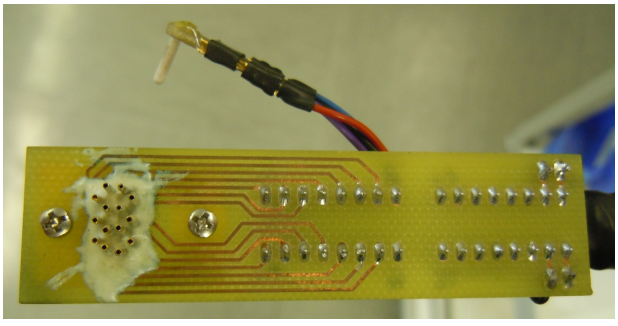

(f) Back side with pins to the left and traces that connect them to the plug.

Figure 4.6: Pictures of the sample holder.

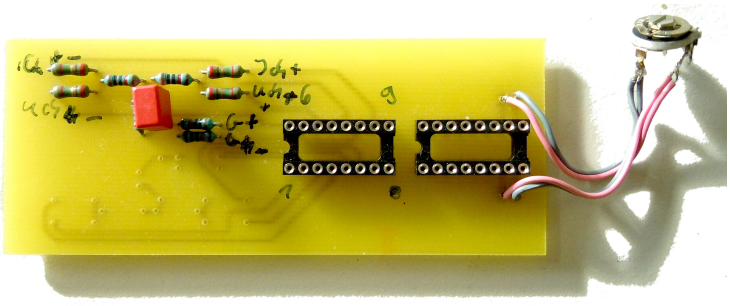

Figure 4.7: Picture of the reference circuit. It largely corresponds to Fig. 3.3. The potentiometer was used to simulate different temperatures.

# Chapter 5

# Results

The results have partly been published in two papers [1, 14].

## 5.1 Device structure

Table 5.1 gives the composition and thickness of some relevant samples. Table 5.2 gives typical deposition conditions. A typical cross-section is shown in Fig. 5.1. Fig. 5.2 shows the structure of a defect in a shadow mask sample. A top view of a lithographically defined sample is shown in Fig. 5.3. Top views of the crossover area of shadow mask samples can be seen in the small figures of Fig. 5.16.

## 5.2 Electrical properties of the electrodes

The conductance of the LCO electrodes (Fig. 5.4) increases with falling temperature down to about 100 K. Below this temperature, the conductance falls steeply. Superconductivity was not observed even at temperatures well below the critical temperature $T_c$ of 33 K for oxygen-loaded LCO [104].

The conductance of the channel contacts is measured by passing a current through the channel with contacts $Ch_{1a}$ and $Ch_{2a}$ and measuring the voltage drop between the contacts $Ch_{1a}$ and $Ch_{1b}$ (compare Fig. 3.3). It follows the same behavior (Fig. 5.4c) as the channel (Fig. 5.4a). That means it is not predominantly an interface effect between silver contact and electrode, but rather caused mostly by the oxide layer between the two contacts. Probably it is just a parasitic effect due to the less-than-ideal geometry (side by side instead of one behind the other) of the contact dots. In any case, it is low enough so that the channel conductance can be measured reliably.

The current-voltage characteristics of the electrodes and the contacts were measured up to voltages of about 50 mV. The electrodes are strictly ohmic within this voltage range at all temperatures. The conductance of the contacts is slightly nonlinear at cryogenic temperatures, but linear at higher temperatures.

Table 5.1: Layer materials and thicknesses for relevant samples

| **Sample** | **Method** | **Gate** | **Dielectric** | **Contacts** | **Channel** | **Passivation** |
|---|---|---|---|---|---|---|
| DW100923-1 | Shadow masks | 28 nm Sr:LCO | 8.9 nm STO | 39 nm Sr:LCO | 7.5 nm LCO | 6.6 nm STO |
| DW101015-1 | | 28 | 18 | 33 | 7.5 | 9.4 |
| DW110118-1 | | 34 | 19 | 42 | 8.25 | 9.4 |
| | | **Contacts** | **Channel** | **Dielectric** | **Gate** | **Passivation** |
| DW120120-1 | Lithography | 26 nm SRO | 9 nm LSMO | 40 nm STO | 67 nm LSMO | 6 nm STO |

Table 5.2: Deposition conditions

| **Material** | **Heater/°C** | **Pressure/mbar** | **Current/mA** | **Voltage/V** | **Rate/$\mathrm{nmh}^{-1}$** | **Anneal** |
|---|---|---|---|---|---|---|
| Sr:LCO | 800 | 2 | 100 | 310 | 12 | no |
| LCO | 800 | 1.2 | 100 | 330 | 15 | no |
| STO | 800 | 3 | RF Power 100 W | | 12 | no |
| SRO | 700 | 3 | 200 | 400 | 22 | no |
| LSMO | 900 | 3 | 200 | 380 | 55 | yes |

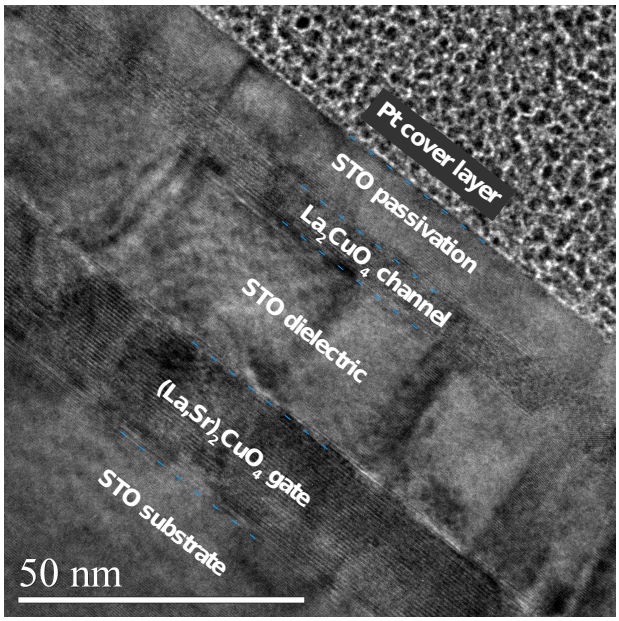


Figure 5.1: TEM cross-section view of DW110118-1 (Preparation: Doris Meertens, TEM: Jin Lei)

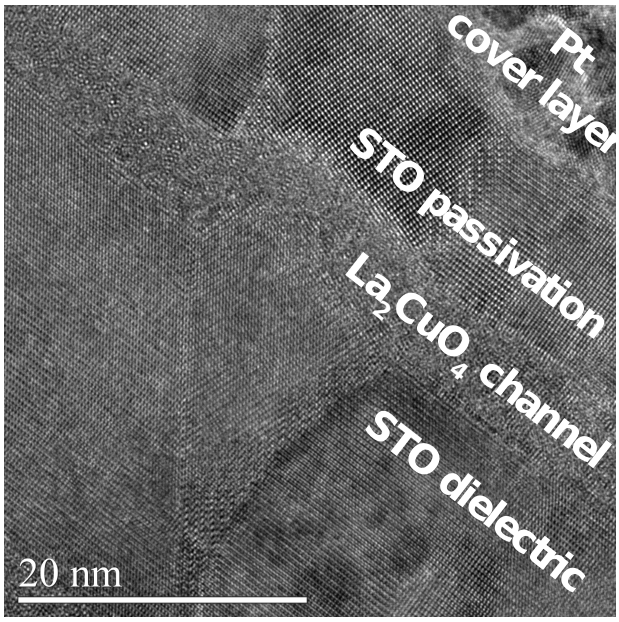


Figure 5.2: TEM cross-section view of DW110118-1: Defect. Such defects appeared at several locations of the sample. (Preparation: Doris Meertens, TEM: Jin Lei)

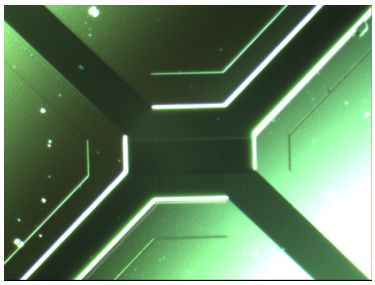

(a) Crossover area with differential interference contrast

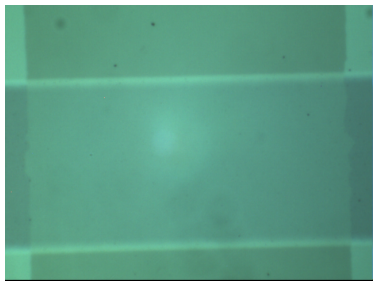

(b) Crossover area

Figure 5.3: Top view of DW120120-1 under an optical microscope. The device is clearly defined. Compare with the shadow mask devices in Fig. 5.16 that have a "cloudy" appearance. See also Fig. 3.7 for dimensions and structural information.

## 5.3 Characteristic curve of the dielectric

The current-voltage behavior of the electrode-dielectric-electrode junction is not linear, but exponential, like in semiconductor-semiconductor or semiconductor-metal junctions.

The characteristic curve of a device with asymmetrically doped electrodes is asymmetric as well (Figs. 5.5a to 5.5d), while the characteristic curve of a symmetric device is symmetric within the measurable precision (Figs. 5.5e and 5.5f). The characteristic curve does however only depend weakly on the thickness. It appears that thicker dielectrics insulate better, but the trend is not very clear because the device properties deviate by one to two orders of magnitude (compare for example Figs. 5.5e and 5.5f as well as Figs. 5.5c and 5.5d) between the two seemingly identical devices that are manufactured in one process on a sample (Fig. 4.1).

For comparison, the current-voltage curve of DW101015-1 device 1 is plotted as a function of $\sqrt{U}$ in Fig. 5.6. The data seem to appear as a straight line, especially in the lower-voltage parts.

The influence of temperature on the dielectric characteristic curve has been investigated in more detail for DW101015-1. Selected curves collected during warming up are plotted with the corresponding fit in Fig. 5.7.

The used instruments do not have the capability to measure the sample capacity. It is however possible to calculate a differential capacity $C$ at a specific voltage $U$ from hysteresis loops with the formula

$$C(U) = \frac{I_1(U) - I_2(U)}{\frac{dU_1}{dt}(U) - \frac{dU_2}{dt}(U)}. \tag{5.1}$$

The current is conceptually split in this calculation into a "resistive" current that is independent on sweep rate, and a "capacitive" current that depends on scan rate and direction $\frac{dU}{dt}$. The measured current is always the sum of both. By comparing the current at a given voltage for two scan rates or scan directions, one can obtain the capacity.

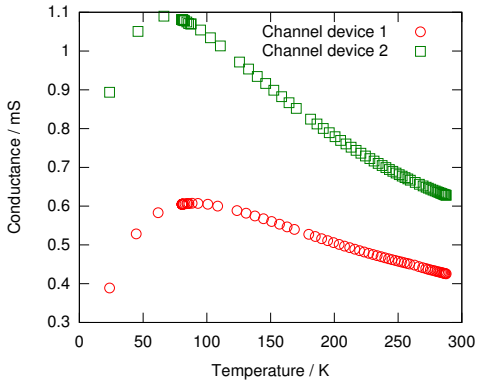


(a) Channel

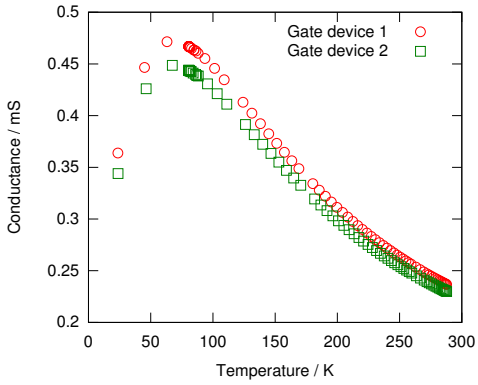


(b) Gate

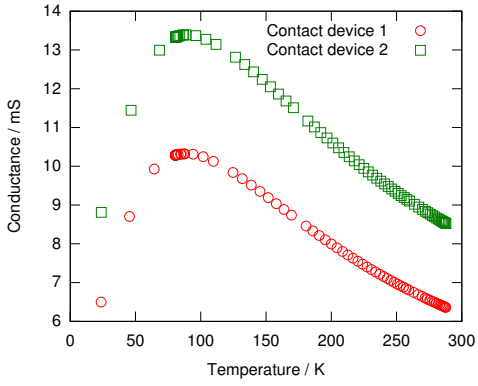


(c) Contact

Figure 5.4: Conductance of channel, gate and contact of sample DW101015-1 as a function of temperature.

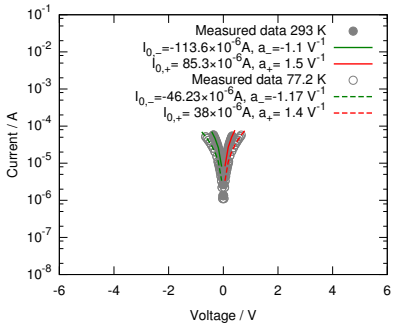


(a) Sample DW100923-1 device 1

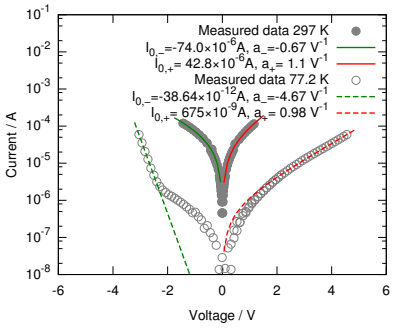


(b) Sample DW101015-1 device 1

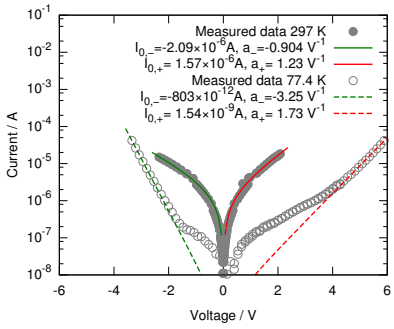


(c) Sample DW110118-1 device 1

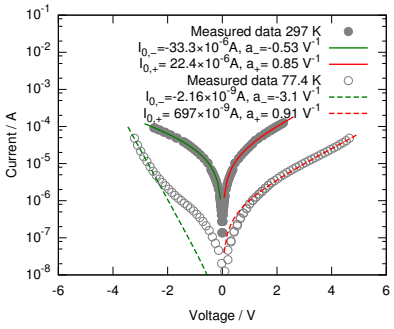


(d) Sample DW110118-1 device 2

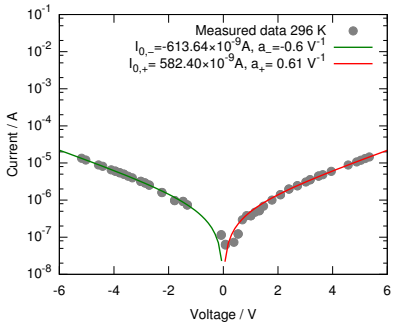


(e) Sample DW120120-1 device 1 (LSMO)

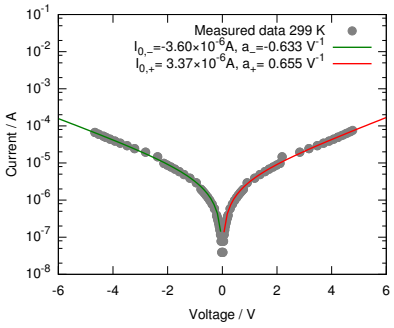


(f) Sample DW120120-1 device 2 (LSMO)

Figure 5.5: Current-voltage curve of the channel-dielectric-gate junction at room temperature and liquid nitrogen temperature for several samples and devices. The solid and dashed lines are a fit of Eq. (6.1) with the indicated fit parameters.

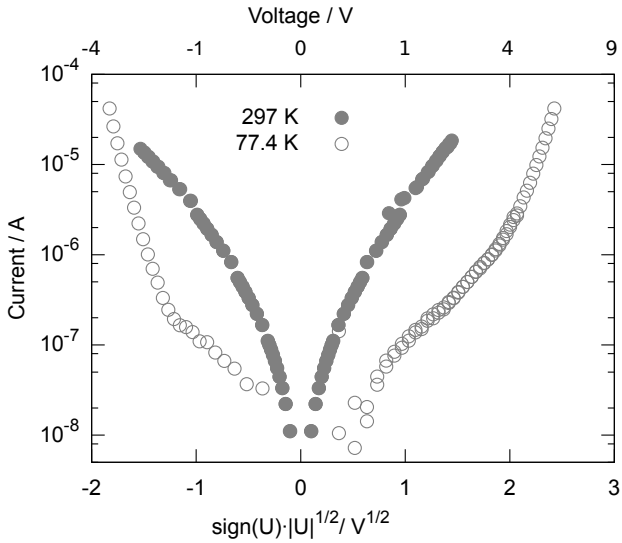


Figure 5.6: Current on a logarithmic scale as a function of the square root of the voltage for DW110118-1. The curve appears more straight than on a linear voltage scale (Fig. 5.5c), especially in the low-voltage region.

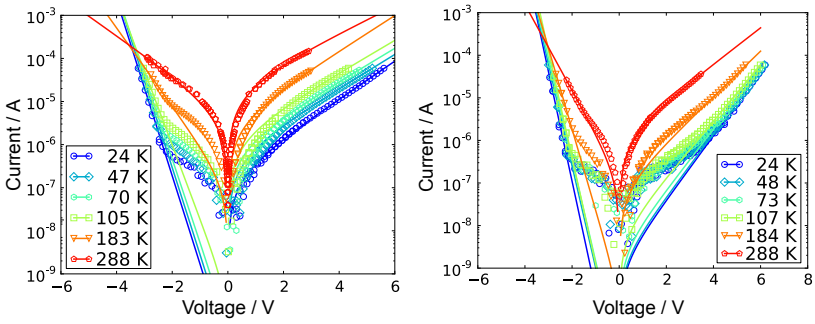


(a) Device 1 (b) Device 2

Figure 5.7: Current-voltage curves of the channel-dielectric-gate junction of DW101015-1 at the indicated temperatures. The solid lines are the corresponding fit of Eq. (6.1).

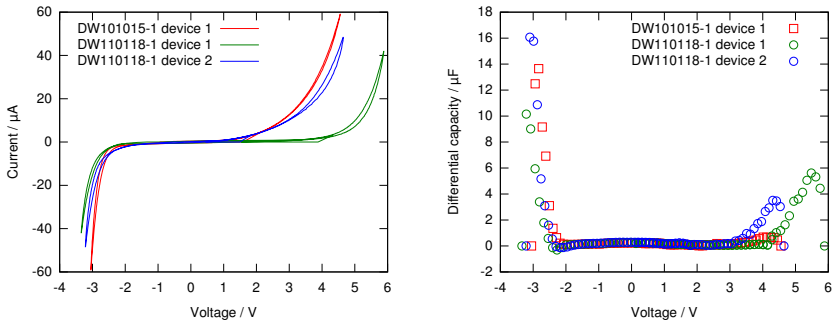


(a) Raw current-voltage hysteresis loops from current sweeps. The scan rate is not constant.

(b) Corresponding calculated differential capacity

Figure 5.8: Differential capacity calculated from hysteresis loops for the indicated samples.

## 5.4 Response to write currents

### 5.4.1 Electrical response

The behavior of the devices is probed with write pulses of varying length, current and polarity over a large parameter space. The measurements are performed by first measuring the conductance, then applying a pulse, measuring the conductance, applying a pulse, and so on.

The data are always presented in two ways: On top, the absolute measured conductances, sometimes with a temperature correction, is plotted for each measurement over the course of the time of the experiment together with the corresponding write current in a subplot below. A clear separation between positive and negative pulses can always be observed. The effect increases with longer pulses and higher current. This plot is meant to give an idea about the overall sequence of the measurement

On the bottom, the relative conductance change $\Delta G/G$, i.e. the conductance difference before and after the pulse, divided by the average of the two conductances, is plotted as a function of pulse duration with double-logarithmic axes. The write currents are encoded with different colors and symbols, and the exact values are given in the legend. This plot allows a more quantitative study of the effect. It turns out that the measured data points more or less align on parallel equidistant lines, in particular for longer write times and higher write currents. A fit of the empirical formula Eq. (6.2) is plotted together with the measured data, and the fit parameters are given in the legend.

A current from the channel to the gate increases the conductance of the channel (Fig. 5.9, Fig. 5.10 and Fig. 5.11) and, to a much lesser degree, decreases the conductance of the gate, and vice versa.

Not only channel and gate, but also the dielectric and the contacts were measured with each cycle. The dielectric did not exhibit any systematic change, but rather a small random shifting with each pulse. The contacts showed some systematic change, but by about a factor of ten weaker than the channel.

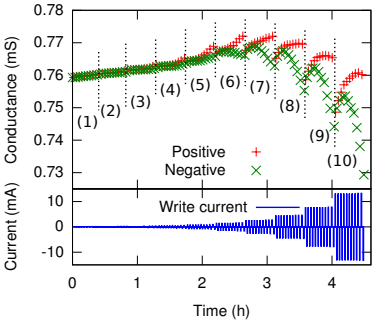


(a) Sample DW100923-1 device 1 at room temperature: Channel conductance over time.

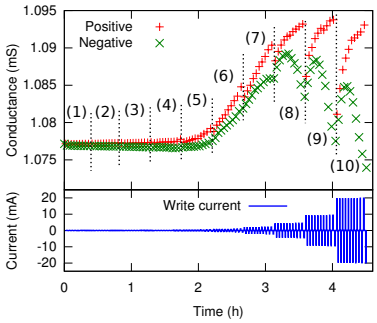


(b) Sample DW100923-1 device 1 in liquid nitrogen: Channel conductance over time. The sample gradually warmed up by about 10 K from half the total time until the end because the coolant was exhausted.

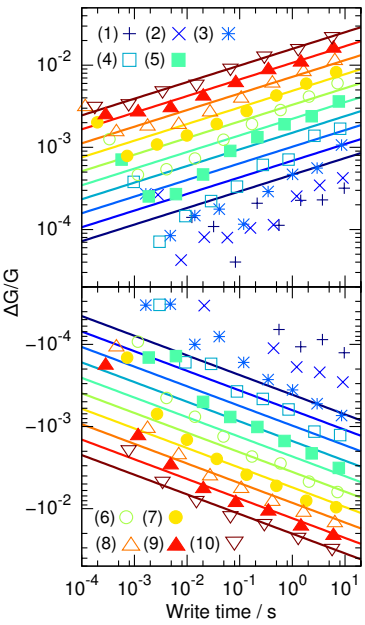


(c) Same measurement as above, processed. (1) 111 µA; (2) 189 µA; (3) 322 µA; (4) 547 µA; (5) 931 µA; (6) 1.58 mA; (7) 2.79 mA; (8) 4.57 mA; (9) 7.77 mA; (10) 13.2 mA. Fit parameters for Eq. (6.2), positive current: C=0.387; A=0.739; B=0.202. Negative current: C=0.689; A=0.815; B=0.240.

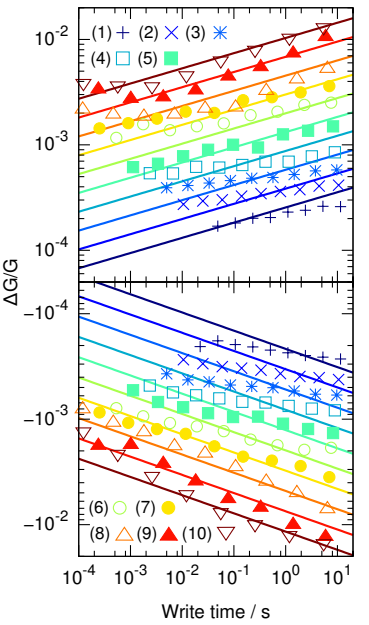


(d) Same measurement as above, processed. (1) 23.8 µA; (2) 50.3 µA; (3) 106 µA; (4) 224 µA; (5) 473 µA; (6) 999 µA; (7) 2.11 mA; 4.45 mA; 9.39 mA; 19.8 mA. Fit parameters for Eq. (6.2), positive current: C=0.0896; A=0.551; B=0.144. Negative current: C=0.119; A=0.593; B=0.173.

Figure 5.9: Conductance change of the channel of sample DW100923-1 device 1 as a reaction to alternating write pulses with varying current and duration at room temperature and in liquid nitrogen.

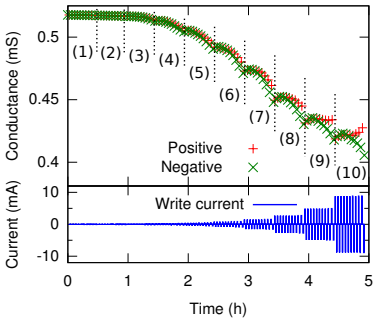


(a) Sample DW101015-1 device 1 at room temperature: Channel conductance over time. The data is compensated for temperature change with a coefficient of -0.0016 $^1/_K$

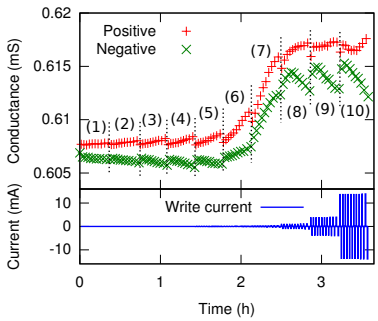


(b) Sample DW101015-1 device 1 in liquid nitrogen: Channel conductance over time.

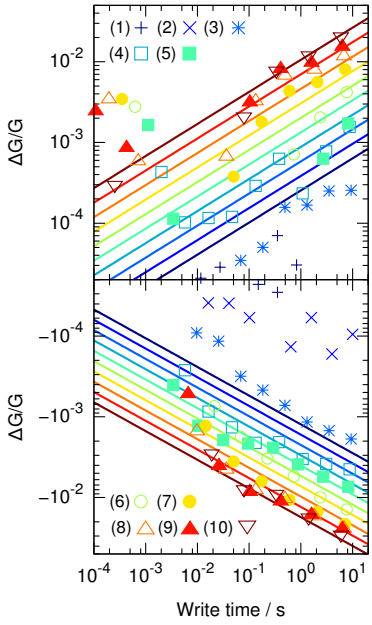


(c) Same measurement as above, processed. (1) 45.5 µA; (2) 81.7 µA; (3) 147 µA; (4) 263 µA; (5) 473 µA; (6) 849 µA; (7) 1.52 mA; (8) 2.74 mA; (9) 4.91 mA; (10) 8.81 mA. Fit parameters for Eq. (6.2), positive current: C=0.302; A=0.708; B=0.398. Negative current: C=0.189; A=0.503; B=0.356.

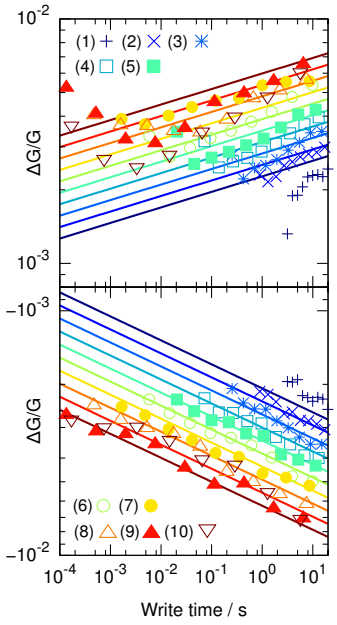


(d) Same measurement as above, processed. (1) 169 nA; (2) 593 nA; (3) 2.09 µA; (4) 7.34 µA; (5) 25.8 µA; (6) 90.8 µA; (7) 319 µA; 1.12 mA; 3.95 mA; 13.9 mA. Fit parameters for Eq. (6.2), positive current: C=0.0863; A=0.0856; B=0.0636. Negative current: C=0.00952; A=0.0977; B=0.0981.

Figure 5.10: Conductance change of the channel of sample DW101015-1 device 1 as a reaction to alternating write pulses with varying current and duration at room temperature and in liquid nitrogen.

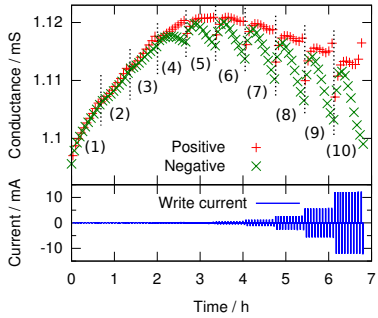


(a) Sample DW110118-1 device 2 at room temperature: Channel conductance over time. The data is compensated for temperature change with a coefficient of -0.003 $^1/_K$

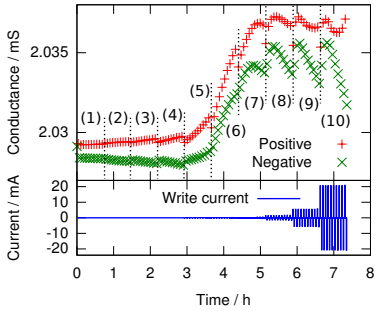


(b) Sample DW110118-1 device 2 in liquid nitrogen: Channel conductance over time.

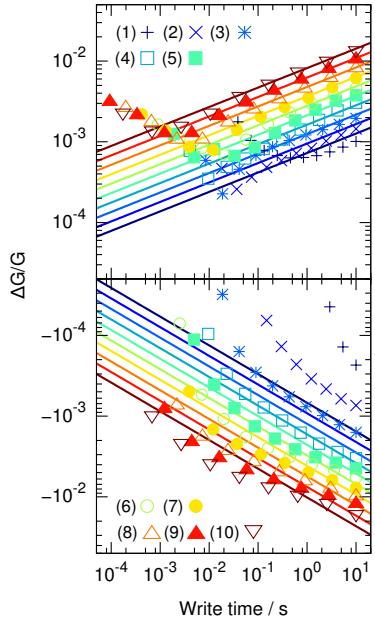


(c) Same measurement as above, processed. (1) 13.8 µA; (2) 29.2 µA; (3) 62.1 µA; (4) 132 µA; (5) 280 µA; (6) 596 µA; (7) 1.27 mA; (8) 2.69 mA; (9) 5.71 mA; (10) 12.1 mA. Fit parameters for Eq. (6.2), positive current: C=0.0396; A=0.357; B=0.217. Negative current: C=0.0589; A=0.398; B=0.241.

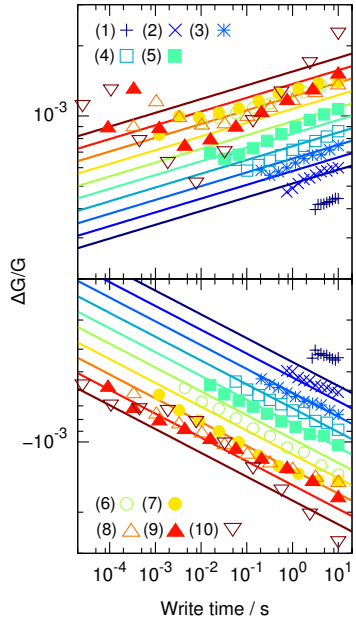


(d) Same measurement as above, processed. (1) 197 nA; (2) 712 nA; (3) 2.57 µA; (4) 9.31 µA; (5) 36.7 µA; (6) 122 µA; (7) 441 µA; (8) 1.59 mA; (9) 5.76 mA; (10) 20.8 mA. Fit parameters for Eq. (6.2), positive current: C=0.00224; A=0.0955; B=0.0590. Negative current: C=0.00282; A=0.118; B=0.102.

Figure 5.11: Conductance change of the channel of sample DW110118-1 device 2 as a reaction to alternating write pulses with varying current and duration at room temperature and in liquid nitrogen.

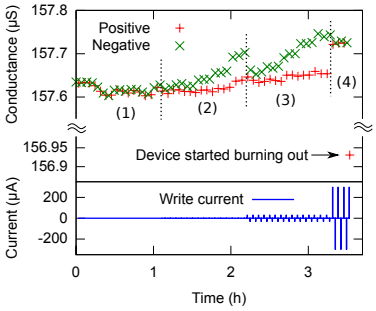


(a) Sample DW120120-1 device 1 at room temperature: Channel conductance over time. The data is compensated for temperature change with a coefficient of -0.023 1/K. (1) 385 nA; (2) 3.54 µA; (3) 32.6 µA; (4) 301 µA.

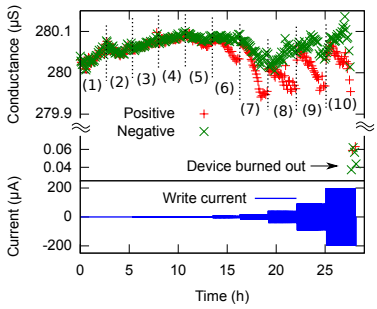


(b) Sample DW120120-1 device 2 at room temperature: Channel conductance over time. The data is compensated for temperature change with a coefficient of -0.019 1/K. (1) 200 nA; (2) 431 nA; (3) 928 nA; (4) 2.00 µA; (5) 4.31 µA; (6) 9.28 µA; (7) 20.0 µA; (8) 43.1 µA; (9) 92.8 µA; (10) 200 µA.

Figure 5.12: Conductance change of the channel of sample DW120120-1 (second generation, LSMO channel).

Several samples with LSMO electrodes were manufactured lithographically. Three samples were prepared with argon ion beam etching and had poorly insulating dielectrics. One sample was etched chemically. The dielectric of this sample was much more insulating (Figs. 5.5e and 5.5f). The switching amplitude was however one order of magnitude lower than for the LCO samples (Fig. 5.12) and the samples burned out at higher current. Numerical analysis of the data did not give clear results, but the samples seem to follow the same law as the previous ones with LCO. The sign of the conductance change was however reversed.

### 5.4.2 Drifting after writing

Drifting was only measured on some shadow mask samples with doped LCO electrodes (Fig. 5.14). The samples change their conductance significantly. The drift is quickest directly after a pulse and then slows down within a time frame in the range of hours. It appears that the channel drifts preferentially towards higher conductances. The measurements have to be corrected for temperature change, because the temperature relaxes in a similar fashion and time frame after a strong write pulse. At the temperature of liquid nitrogen, the samples drift as well, but to a lesser extent (Fig. 5.15).

### 5.4.3 Optical changes

Pulses of 10 min length lead to reversible visible changes (Fig. 5.16). The microscope image turns darker with a positive current and brighter with a negative current on the right and on the bottom of the crossover area, with a maximum in the right lower corner. Longer pulses cause an irreversible degradation of the samples (Figs. 5.17 and 5.18). The microscope image changes brightness instantaneously when a negative voltage is switched on or off (Fig. 5.16). Possible explanations are the electrical field

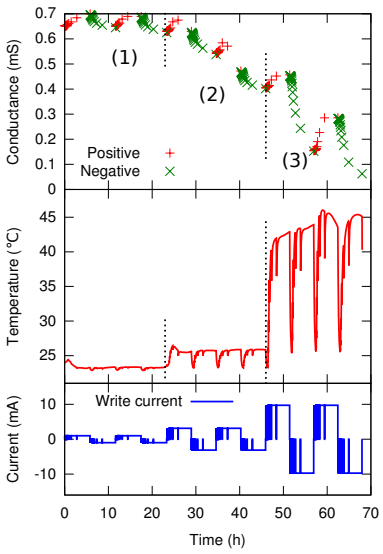


(a) Sample DW110118-1 device 1 at room temperature: Channel conductance, temperature and write current over time. The power of the write pulses increased the sample temperature significantly.

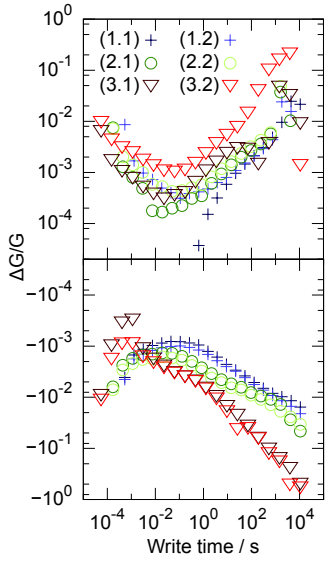


(b) Same measurement as on the left, processed. The individual pulse length and individual relative change per pulse are plotted, not the cumulative time and cumulative change. (1) 1 mA; (2) 3.12 mA; (3) 9.72 mA.

Figure 5.13: The sample DW110118-1 device 1 was written with several series of long pulses with the indicated polarity to test the limits of the time dependence. Two cycles were measured for each current. This degraded the sample (irreversible drop in conductance) and lead to visible changes (Fig. 5.17).

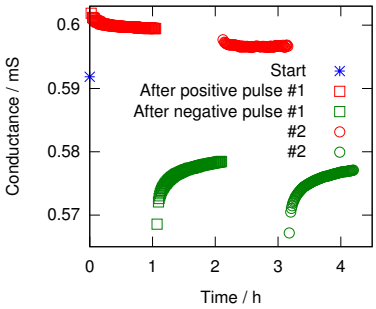


(a) Sample DW100923-1 device 1: Drift after write pulses of ±10.8 mA and a duration of 25 s. The sample drifts much stronger from lower to higher conductances than in the opposite direction. The data is compensated for temperature change with a coefficient of -0.0016 $^1/_\kappa$, determined in other measurements.

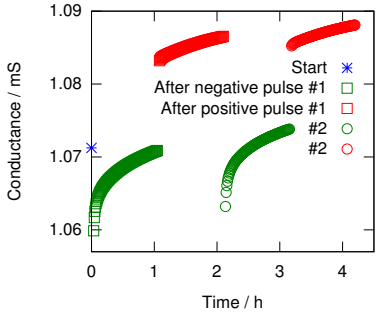


(b) Sample DW110118-1 device 2: Drift after write pulses of ±11.6 mA and a duration of 25 s. The sample continues to drift to higher conductances even after a positive write pulse. The data is compensated for temperature change with a coefficient of -0.003 $^1/_\kappa$, determined in other measurements.

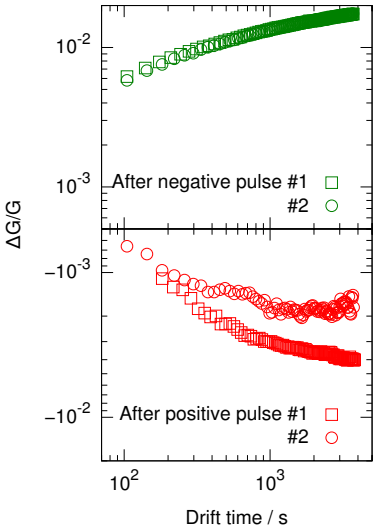


(c) Same measurement as above, double logarithmic plot relative to the first measurement after a write pulse.

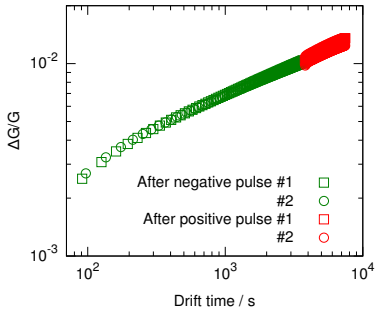


(d) Same measurement as above, double logarithmic plot. The data of the positive pulses is plotted as a continuation of the previous negative pulse by shifting it by the appropriate amounts in x and y direction.

Figure 5.14: Drifting behavior of two different samples.

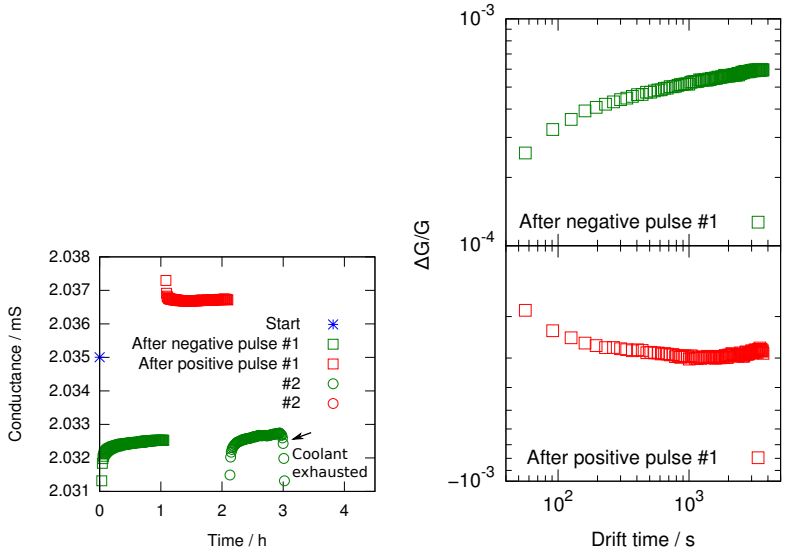


(a) Sample DW110118-1 device 2: Drift after write pulses of ±17.4 mA and a duration of 25 s. The coolant was exhausted towards the end of the measurement.

(b) Same measurement, double logarithmic plot of the first two sections.

Figure 5.15: Drifting behavior at the temperature of liquid nitrogen (DW110118-1).

effect (a change of carrier concentration leads to a change of optical properties), or the Pockels or Kerr effect where an electrical field induces a change of optical properties in dielectrics.

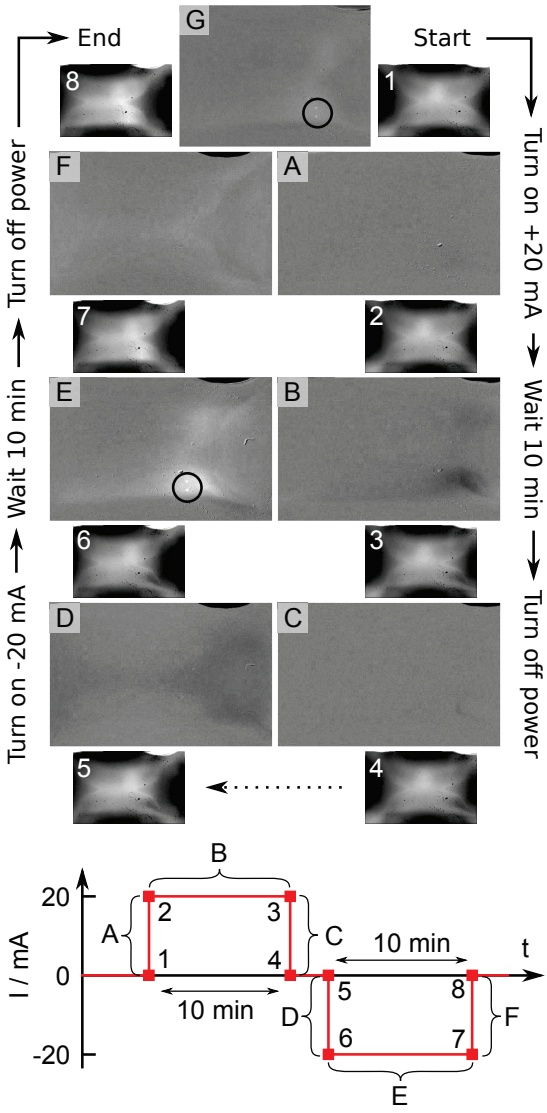


Figure 5.16: Sample DW110118-1 device 2: Reversible changes induced by writing are visible in an optical microscope (reflected light). The larger images show the difference between the adjoining smaller images to highlight the changes. The width of each image is roughly 1.8 mm and it shows the crossing area between channel (vertical) and gate (horizontal). The current flowed between the lower (channel) and the right (gate) side, and the change is localized in the area of maximum field strength in the dielectric. Indicated by a circle are two small "speckles" that are newly forming degradation defects like the ones shown in Fig. 5.17 after much longer writing time.

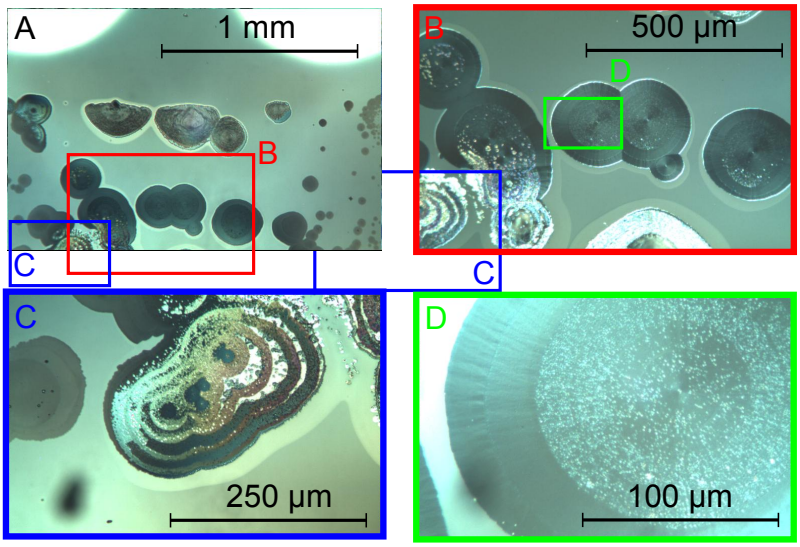


Figure 5.17: Sample DW110118-1 device 1: Visible degradation (optical microscope) after repeated alternating write pulses at full power for up to one hour (compare Fig. 5.13). The channel conductance is irreversibly reduced by more than one order of magnitude.

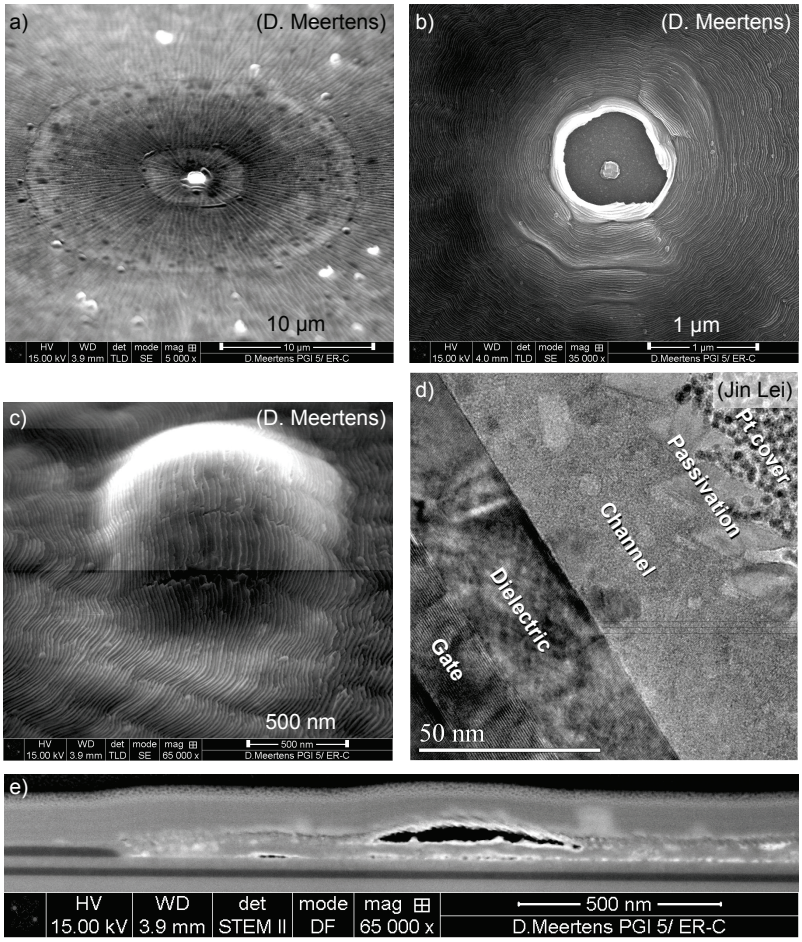


Figure 5.18: The same sample as in Fig. 5.17, characterized with SEM and FIB-prepared TEM cross-sections. a) and b) show the center of one of the circular defects. c) is a bubble in the periphery. d) shows a cross-section in a degraded area. e) is a cross-section on the border between a degraded and an intact area. The channel layer on top has become polycrystalline and expanded during degradation, i.e. it has turned into a different phase and chemically reacted with ambient. A bubble is visible as well. The curious rippled surface texture comes from the passivation layer that breaks in a scaly fashion due to the expansion of the channel while the defect area grows.

# Chapter 6

# Discussion

## 6.1 Behavior of the electrodes

The high conductivity that increases towards lower temperature means that the electrodes are doped: Undoped LCO would have a much lower conductivity that decreases at low temperature [104]. The conductivity drop below 100 K can be explained with charge carriers freeze-out, i.e. they get bound to their donors.

## 6.2 Dielectric characteristic curve

The measured electronic current $I_{el}$ as a function of voltage $U$ can be fit with the Shockley equation for diodes (Eq. (2.2))

$$I_{el} = I_{0,el} \left( \exp \left( a_{el} \times U \right) - 1 \right) \tag{6.1}$$

with fit parameters $I_{0,el}, a_{el}$ being different for the positive and negative current direction.

The strong influence of the electrode doping and the weak influence of dielectric film thickness indicate that the interfaces between electrode and dielectric have a big influence on the current-voltage behavior of the STO dielectrics. The data at room temperature are in good agreement with two anti-parallel Schottky junctions at the electrode-dielectric interfaces. Yajima *et al.* [105] obtained comparable results with $Al/SrTiO_3/La_{0.7}Sr_{0.3}MnO_3/Nb{:}SrTiO_3$ heterojunctions.

It appears that the curves in Fig. 5.7 have two components: One high-voltage part that is hardly dependent on temperature, and a low-voltage part that strongly depends on temperature and dominates at room temperature within the measured range. This hints at two different conduction channels or conduction mechanisms. Fowler-Nordheim field emission would be a conduction mechanism that is independent on temperature [106], while Schottky thermionic emission and Poole-Frenkel hopping conduction strongly depend on temperature [107, 108]. The dielectric of the samples is with 9 nm to 40 nm too thick to allow direct tunneling between channel and gate. An alternative would be direct tunneling from the valence band of the electrodes into the conduction band of the STO dielectric. This possibility was not investigated further.

Schottky thermionic emission and Poole-Frenkel hopping conduction give straight lines in a $\log(I)$ vs. $\sqrt{U}$ plot [107, 108]. Such a plot is shown in Fig. 5.6. The low-voltage part appears less curved in this plot, but the difference is not very clear.

The temperature behavior of the fit parameters was not studied in detail, because the two-component curves were considered too complex to fit reliably with two functions at the same time. Furthermore, the high-voltage part is most likely distorted due to parasitic effects, as lined out in Section 3.1.

To investigate the dielectric properties in more detail, one would need more samples with uniform properties. The current crossbar structure is unnecessarily complex to measure the out-of-plane properties: A common bottom electrode covered by the dielectric and individually contacted electrode dots on the surface would be far easier to produce and could be measured with suitable wafer probers. The most important conclusion in the context of this thesis is that the current through (semi-)insulating oxide thin film heterostructures can behave in a complex, non-linear way as a function of voltage and temperature. The current as a function of voltage behaves roughly exponentially. Interface and size effects play a big role, that means the device behavior cannot be understood from the material's bulk properties.

The properties of seemingly identical devices that were manufactured in one process on the same sample differ by up to two orders of magnitude (compare Figs. 5.5 and 5.7). Either the dielectric contains few randomly distributed defects that carry the majority of the current, or there are subtle differences in the interface properties that have a huge impact on the properties of a junction. Hikita *et al.* [109] reported that the barrier height of LSMO/Nb:$SrTiO_3$ depends sensitively on the surface termination of the interface. The termination was not controlled during sample manufacturing. But in that case the characteristic curve should not be symmetric in any case, but strongly asymmetric depending on the random termination of the interfaces. This makes defects in the dielectric appear as a reasonable explanation for the diverging device properties.

The measured current is always a combination of the influence from both junctions, because one of the two junctions is always in reverse direction and one is in forward direction. The reverse junction has the biggest influence and limits the total current flow. The junctions are not very insulating in reverse direction, according to the obtained data.

## 6.3 Is it really ionic conduction or rather something else?

With respect to time, the changes happen on time scales between milliseconds and hours. This is within the expected range for relatively slow ionic conduction.

The observed gas bubbles (Fig. 5.18) mean that a gas was produced during writing. This is a strong indication for an electrolytic process where the oxygen pressure exceeds the material's mechanical strength. The applied voltages in the range of several volts are high enough to split an oxide into metal on the cathode side and oxygen on the anode side, i.e. they exceed the material's stability window. The ionic transport is therefore only limited kinetically, not thermodynamically, under such conditions.

The writing leads to visible changes (Fig. 5.16). That confirms that the effect really takes place at the crossover area.

The gate changes conductance inversely to the channel. The characteristic curve of the dielectric does not change systematically during writing. This means that the change takes place inversely on both sides of the dielectric and no varying leakage paths between channel and gate are responsible.

If one looks at the transported charge during an experiment, one can conclude that most of the electric transport is electronic: The volume of a typical channel for shadow mask devices is $1\,\mathrm{mm}\times0.5\,\mathrm{mm}\times10\,\mathrm{nm} = 5\cdot10^{-15}\,\mathrm{m^3}$. The unit cell volume of LCO with two formula units is $379\,\mathrm{pm}\times382\,\mathrm{pm}\times1315\,\mathrm{pm} = 1.90\cdot10^{-28}\,\mathrm{m^3}$. That means the channel contains $\frac{5\cdot10^{-15}\,\mathrm{m^3}}{1.90\cdot10^{-28}\,\mathrm{m^3}}\cdot\frac{2}{N_A} = 87.2\,\mathrm{pmol}$ LCO or consequently 384 pmol oxygen. The amount of charge that is transported during the longest writing step in Fig. 5.13 is about $10\,\mathrm{mA}\cdot3600\,\mathrm{s} = 36\,\mathrm{C}$. In molar quantities this is $\frac{36\,\mathrm{C}}{e\cdot N_A} = 373\,\mu\mathrm{mol}$. With a charge of -2 for the oxygen anion, 187 µmol of oxygen anions can be transported with that charge. That means that the amount of transported charge is about six orders of magnitude higher than the upper limit for the amount of oxygen available for transport! Most of the charge is therefore transported electronically. The tiny amount of transported oxygen can however be detected as a small change of channel conductance, independent of the total transported charge.

## 6.4 Empirical formula

The relative conductance change $\frac{\Delta G}{G}$ as a function of write current $I$ and write time $t$ follows the empirical law

$$\frac{\Delta G}{G} = \left(\frac{I}{I_{0,ion}}\right)^A \left(\frac{t}{t_0}\right)^B = CI^A t^B \tag{6.2}$$

over several orders of magnitude with fit parameters $C = (1/I_{0,ion})^A(1/t_0)^B$, $A$ and $B$ being different for positive and negative current direction. The conductance change follows this law also at the temperature of liquid nitrogen, but with different fit parameters for Eq. (6.2) (Fig. 5.9d, Fig. 5.10d and Fig. 5.11d). All three parameters differed from sample to sample and between the two devices on one sample. The data are less accurate for weak currents and short write times due to drifting over the course of the experiment and the charge lost in parasitic capacitances. The time dependence was further investigated with write pulses of up to one hour and up to roughly 10 mA (Fig. 5.13).

## 6.5 Time-domain behavior

A. K. Jonscher [24, 110] observed that dielectrics relax in a universal way following a power law. The behavior can be described equivalently in the frequency domain as a response to a sinusoidal signal of varying frequency, or in the time domain as the response to a step function. Such behavior is regarded as one fingerprint of ionic conduction [111], but is also observed in more complex mixed ionic-electronic systems [85]. The time-domain behavior of the devices here is such a power law (compare Section 5.4 and Eq. (6.2)). This is therefore in good agreement with theory.

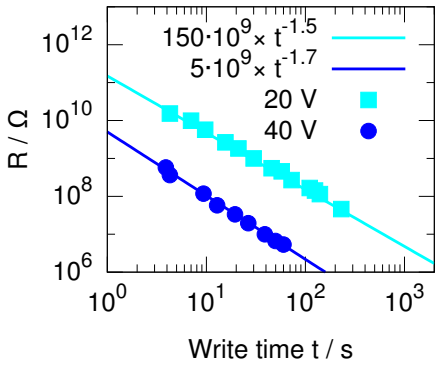


Figure 6.1: Resistance data from Ramesham *et al.* Fig. 2(b)[15], re-plotted on a double-logarithmic scale. The data reveals a similar power law as observed for the devices here. Note that absolute resistance over time are plotted here, differently from the convention in this thesis.

Analysis of data from Ramesham *et al.* [15] reveals that these devices follow a power law with respect to time (Fig. 6.1) as well.

For a relaxation process, like a capacitor that discharges over a resistor, one expects a relaxation current of the form $I(t) = I_0 \exp(-t/t_0)$, with relaxation time $t_0 = RC$ in the case of a discharging capacitor with capacity $C$ and a resistor with resistance $R$. In general, such a law results from a relaxation current back towards an equilibrium state that is proportional to the deviation from equilibrium, with negligible momentum of the system and complete energy dissipation of the relaxation current.[1] In the case of this work, the resistance change within a specific time interval is measured instead of the relaxation current. This is the integral over time of the relaxation current. This would still be an exponential function, but with a different proportional factor and a constant summand. The samples did not display such a behavior. Instead, they seem to follow a power law with varying exponent in the time domain. An exponent of 0.5 could be explained with diffusion laws, but the exponent differs significantly from 0.5. Such a power law results when a spectrum of exponentials with different relaxation times are combined [112]:

$$I(t) = \int_0^\infty I_0(t_0) \exp(-t/t_0)\, dt_0 \tag{6.3}$$

$I_0(t_0)$ now describes the prevalence of reservoirs with a relaxation time $t_0$. A non-trivial example with

$$I_0(t_0) = \begin{cases} {t_0}^{-1.5} & \text{if } t_0 \in [10^{-2}, 10^2] \\ 0 & \text{otherwise} \end{cases} \tag{6.4}$$

is shown in Fig. 6.2. The function plot is parallel to $\sqrt{1/t}$ in the region between the relaxation time cutoffs. This slope depends on the exponent in Eq. (6.4).

Eq. (6.3) resembles the Laplace transform $\mathcal{L}\{f\}(s) = \int_0^\infty f(t) \exp(-s\,t) dt$. The only difference is that in the Laplace transform, $t$ is multiplied, while in Eq. (6.3), $t_0$

[1] If the system has a significant momentum, such as an inductivity in the capacitor example, and comparatively low loss, one obtains a damped harmonic oscillator.

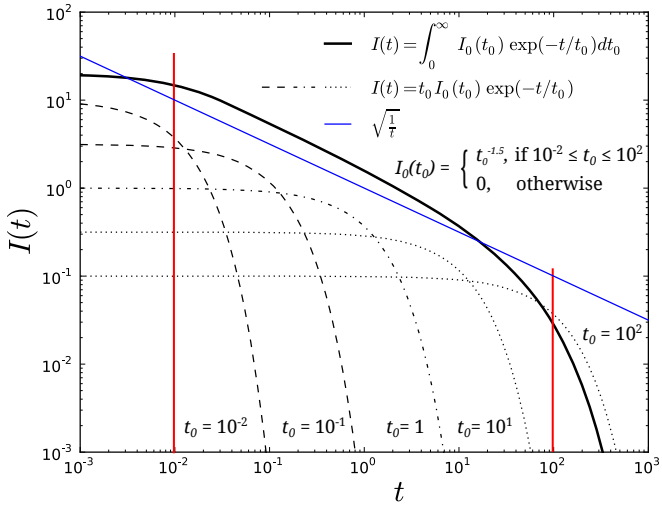


Figure 6.2: Calculated relaxation current $I(t)$ for a system that has a spectrum of relaxation times $t_0$ (thicker solid line) together with relaxation currents for different discrete relaxation times (dotted and dashed lines). The "reservoir" function $I_0(t_0)$ is non-trivial with cut-offs at high and low relaxation times, as indicated in the figure by red vertical lines. The blue line is an exemplary power law with the same slope as the total relaxation current. After [112].

appears in the denominator inside the exponential. When $\phi(t_0) := \frac{1}{t_0}$ and $I_0^*(s)$ with $I_0^*(\phi(t_0)) := I_0(t_0){t_0}^2$ for $t_0 \in [0, \infty]$ are substituted into Eq. (6.3), one obtains with $\lim_{t_0 \to 0+} \phi(t_0) = \infty$:

$$I(t) = \int_{\infty}^{0} I_0(t_0){t_0}^2 \frac{-1}{{t_0}^2} \exp\left(-t/t_0\right) dt_0 \tag{6.5}$$

$$= \int_{\infty}^{0} I_0^*(\phi(t_0))\phi'(t_0) \exp\left(-t\phi(t_0)\right) dt_0 \tag{6.6}$$

$$= \int_{\phi(\infty)}^{\phi(0)} I_0^*(s) \exp\left(-ts\right) ds \tag{6.7}$$

$$= \mathcal{L}\{I_0^*(s)\}(t) \tag{6.8}$$

A minimum or maximum relaxation time would reveal itself in the plots of conductance change over time. For write times well below the minimum relaxation time, the relaxation current is approximately constant. That means that the amount of change should be proportional to the time. In the double-logarithmic plots, this would result in a slope of 1 (exponent is 1), steeper than typical (exponent smaller than one). For times much larger than the maximum relaxation time, the relaxation current would approach zero, which means that the conductance change reaches a constant saturation value. The slope in a double-logarithmic plot would then be zero. Such a behavior was not clearly observed in the data, neither at room temperature nor in liquid nitrogen. It appears that a very wide range of relaxation times play a role. This is in agreement with the findings of Jonscher [24, 110]. The drift after writing seems to follow a similar law.

It is hard to interpret the observed effect with respect to the exact nature of the relaxation process, because the effect is not distributed uniformly over the crossover area. The relaxation spectra of different sample regions (different field strength, thicknesses, defects, conductance changes, temperatures) are convoluted into one measured spectrum, with a lot of noise and drift on top of that. Therefore high-quality, stable and uniform samples with large switching amplitude are an important prerequisite to interpret the data in terms of physical processes. Such samples could unfortunately not be produced within the given time.

## 6.6 Current dependence

The driving force for transport is a potential gradient, not a current. Measurements at a defined voltage would therefore be of advantage. The samples and the setup do however not allow to define or accurately measure the write voltage, but only the write current.

The current-dependence can however be transformed into a voltage dependence with the equation that describes the current-voltage behavior of the dielectric. If the "$-1$" term is omitted from Eq. (6.1) (valid at higher $U$) and the resulting exponential function is inserted into Eq. (6.2), one obtains the equation [1]

$$\frac{\Delta G}{G} = \left(\frac{I_{0,el}}{I_{0,ion}}\right)^A \exp\left(a_{el} \times A \times U\right) \left(\frac{t}{t_0}\right)^B, \tag{6.9}$$

which would indicate that the ionic transport increases exponentially with the applied voltage. This behavior would be expected from the theory on high-field ionic conduction (see 2.5). The maximum voltage during writing could be measured for the lithographically defined sample DW120120-1 as about 6.5 V. The field strength in the dielectric can therefore be estimated as 1.625 MV/cm if a constant field across the dielectric is assumed. This fits very well the expected range for non-linear ionic transport above 1 MV/cmSection 2.5.

## 6.7 Drifting behavior

The channel conductance relaxes following a power law, a logarithmic or an exponential. The time range of the measurements is unfortunately not big enough to make the distinction, because the conductance of the channel can only be measured more than 20 s after the write pulse has finished: The setup has to discharge all cables, switch to the channel and activate the appropriate settings for current source and nanovoltmeter. The sample already drifts by a significant amount before the first measurement can be taken.

This also has an implication for the measurement of the writing response, because here the channel measurement is delayed by the same amount of time. By then, the sample has already drifted. Fortunately, the drift time is nearly constant because the setup is automated.

The samples seem to drift preferentially towards higher conductance. From the measurements it cannot be distinguished clearly if the drift is due to a change of carrier concentration or carrier mobility in the electrodes. Both is thinkable: The concentration change could be driven by transport of oxgyen in a gradient of electrochemical potential that was induced by the write pulse, i.e. by a relaxation process opposed to the previous excitation by the write pulse. It could however also happen that the oxygen in the LCO electrodes orders itself and thus increases the carrier mobility.

If it was a relaxation process, one would expect that the sample relaxes towards an equilibrium state in an asymptotic fashion. In some samples, like particularly DW110118-1 (Figs. 5.14b and 5.14d), the conductance always relaxes towards higher values, even after a write pulse that increases the conductance. It even seems like the relaxation process of the previous negative write pulse continues after a positive write pulse (Fig. 5.14d). I do not have a good explanation for this behavior.

It is also a bit puzzling that the samples drift without an applied voltage at the temperature of liquid nitrogen. The formula Eq. (2.4) and also Fig. 2.3 suggest that at this temperature there is no oxygen transport without a strong field. Perhaps there is another unknown effect playing a role.

## 6.8 Behavior of different materials

The sign of the conductance change was reversed for the lithographic samples with LSMO channel. This material is from an electronic point of view more complicated than a simple semiconductor [113], because the electrons order into a magnetic state with high conductivity at the used doping level [39]. Deviations from this doping

level towards higher or lower values *both* decrease the conductivity, as does moderate heating that brings the sample into an unordered semiconducting state [113, 114].

LSMO samples switch about one order of magnitude less than the LCO samples (compare Figs. 5.11 and 5.12). Unfortunately, no lithographic LCO samples could be measured. It seems that the electrode material has a huge influence on the device performance. Possible explanations are a slow oxygen transport within the LSMO electrode, slow transport across the STO/LSMO interface, or weaker impact of oxygen on the conductivity of LSMO. Li *et al.* [83] found at intermediate temperature a superior performance of LCO-based cathode materials for solid oxide fuel cells compared to LSMO-based cathodes in terms of oxygen exchange and oxygen transport speed. This finding could be related to the observations here.

## 6.9 Asymmetry

The interface between electrode and dielectric behaves like a Schottky junction and should therefore have an asymmetric current-voltage behavior. That means that at the same current, the electrical field at the interface is different depending on the current direction. In the case of p-type electrodes (e.g. LCO) and n-type dielectric (STO), the field at the interface is lower when the electrode is at a positive potential relative to the dielectric (forward direction). This means that the transport of oxygen anions from the dielectric to the electrode should be slower than in the opposite direction at both interfaces. The results in Section 5.4 are in agreement with this: The channel changes preferentially towards lower conductance, that means loss of oxygen. It could however also be possible that the ion transport is asymmetric (see Section 2.3). The effect would be in the same direction in case of the STO/LCO combination. This can therefore not be clearly differentiated by now. It would be interesting to compare material combinations with different current-voltage characteristics (combinations of p-type and/or n-type doping) and different oxygen anion transport mechanisms (interstitial versus vacancy).

## 6.10 Influence of temperature and voltage

Ionic relaxation processes in solids are activated by temperature. The factor $t_0$ in Eq. (6.3) is therefore smaller at higher temperature. One could therefore think of the influence of temperature as shifting of the relaxation time spectrum in Eq. (6.3): Lower temperature shifts to longer times, and higher temperature shifts to shorter times. Measurements at very low or very high temperature could therefore allow to explore processes that are either too fast or too slow to be measured at room temperature with simple means.

Temperature has however also a strong influence on the electrical behavior of the electrode-dielectric-electrode heterostructure as well (Section 5.3). With the current setup and the large first-generation devices, it is not possible to measure the true voltage during writing because of parasitic effects (compare Fig. 3.6). On top of that, the voltage total voltage is probably distributed unevenly between the two interfaces and the bulk (compare Section 6.9) and also unevenly across the crossover area (compare Figs. 3.5 and 5.16). The characteristic curve is at low temperature more complex than a simple exponential (see Section 5.3). It is for all these reasons difficult

to get a realistic pictures of the electric fields that drive the observed processes. More, detailed measurements on devices and on partial device stacks with very uniform properties would be necessary.

The device warms up during writing at high power. The sample reached a dynamic thermal equilibrium during the long writing experiment (Fig. 5.13) with a temperature at the sensor of 45 °C. With a power of $10\,\mathrm{mA} \cdot 34\,\mathrm{V} = 0.34\,\mathrm{W}$, a thermal conductivity $k$ of $12\,{}^{\mathrm{W}}/_{\mathrm{m\cdot K}}$ for STO and $0.025\,{}^{\mathrm{W}}/_{\mathrm{m\cdot K}}$ of the air gap of estimated 1 µm between sample and heat sink, one arrives with $\Delta T = P \cdot \frac{1}{k} \cdot \frac{d}{A}$ at a temperature difference in the order of magnitude of $0.34\,\mathrm{W} \cdot \left( \frac{1}{12} \frac{\mathrm{m\,K}}{\mathrm{W}} \cdot \frac{1\,\mathrm{mm}}{2\,\mathrm{mm}^2} + \frac{1}{0.025} \frac{\mathrm{m\,K}}{\mathrm{W}} \cdot \frac{1\,\mu\mathrm{m}}{8\,\mathrm{mm}^2} \right) = 16\,\mathrm{K}$. That means the sample reaches a maximum temperature of roughly 60 °C. That is significant, but not extreme. A more precise temperature measurement directly in the active region would be desirable for future experiments. That is possible with, for example, a lithographically structured Pt resistance thermometer directly on top of the active region.

The smaller lithographically structured samples can reach a much higher power density and thus a much higher temperature. This might have played a role in the destruction of the samples during writing.

It is astonishing that ionic transport seems to occur also at the temperature of liquid nitrogen. As expected, the transport is slower. But if one looks at Fig. 2.3 more closely, one can see that for an activation energy of 1 eV there should be a difference of 30 orders of magnitude in transport speed at a field strength of $10^9$ V/m between room temperature and liquid nitrogen. The observed difference in conductance change amplitude is only about one order of magnitude. There could be several different explanations:

- The field strength is much higher for the same current at liquid nitrogen temperature (compare Section 5.3).
- There are mobile ions with much lower activation energy than 1 eV present in the sample (compare the 0.4 eV curve with the 1 eV curve in Fig. 2.3 and, for example, [65]).
- The transport is very short-ranged and low-volume, so that individual ions with a low activation energy for a single position change play a role, as opposed to bulk long-distance transport.
- The temperature in the transport zone is higher than expected.
- The high electronic current and field strength activate ionic jump processes in different ways than expected.

It should be noted that temperature is actually ill-defined if electronic carriers with high mobility encounter a strong electric field inside a semiconductor: They can be accelerated way out of their "thermal" energy range between inelastic collisions [115]. That means they can provide activation energy, for example for chemical processes, tunneling or impact ionization. This phenomenon is called "hot carrier injection". It could be that such hot electrons or also hot phonons [115] generated from collisions with hot electrons activate ionic jump processes. This normally does not play a role for ionic conduction for four reasons:

1. The electrical field is usually not strong enough.
2. Up to now, a very weak ionic current parallel to a strong electronic current was hardly measurable.
3. Typical ionic conductors have a low electronic mobility.
4. In particular, the mobility is very low at elevated temperature

In that sense one can expect surprises in ultra-thin high-quality epitaxial oxide films at high field strength and very low temperature, because the carrier mobility in materials like STO can be high under such conditions [116].

For processes with very fast relaxation times, i.e. with low activation energy, the electrical field strength can become strong enough to provide *all* the activation energy. This situation can be seen in Fig. 2.3 at the point where the calculated relative mobility reaches 1. Above this field strength, the relaxation process is triggered quasi-instantaneously, independent of temperature. The time limit is probably in the range of typical lattice vibrations, that means picoseconds. At lower temperature, higher fields can be reached because thermally-assisted processes that carry a lot of current at room temperature are quenched. The relaxation processes with lower energy drift back much more slowly than at room temperature, and processes with higher activation energy than the field strength are slowed down as well, i.e. they contribute less. That means it is very promising to continue exploring the device behavior at very low temperature to investigate relaxation processes with low activation energy.

The reaction of the device is for fields that exceed the activation energy not dependent on time, but only on the voltage. Such a behavior was perhaps observed at the temperature of liquid nitrogen in two samples with very insulating dielectric (Figs. 5.10d and 5.11d), where the $B$ exponent of Eq. (6.2) is very small, i.e. where time has little influence (Fig. 6.3). Strained STO becomes however ferroelectric at lower temperatures [117]. The device could therefore function like a ferroelectric field-effect transistor. Such a device has a very low response time as well. The data at 77 K has to be interpreted with care for that reason. Measurements of the polarization and generally of the dielectric properties were not possible in satisfactory quality with the used measurement devices. A very rough measure of the differential capacity as a function of voltage was derived from current sweeps (Fig. 5.8) and showed peaks towards high voltages. This could be ferroelectric behavior, but it could also be the result of a memristive behavior of the dielectric or a timing difference between current and voltage. Only a temperature effect can be excluded, because the sweep towards higher absolute voltage has a higher absolute current than the sweep towards lower voltage when they pass the same voltage. Heating would have the opposite effect (compare Fig. 5.7). The setup is not suited to investigate dielectric behavior in detail and this was therefore not further pursued.

## 6.11 Towards quantitative measurements of oxygen transport

In principle, the methods described here could be used to measure oxygen transport quantitatively. The requirements for such measurements are lined out in this section.

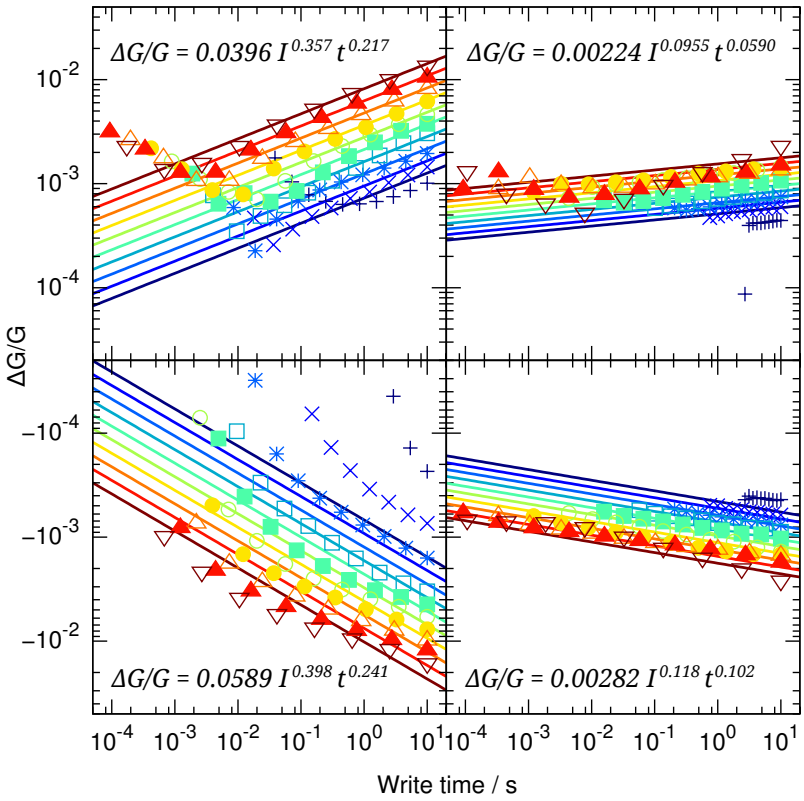


Figure 6.3: The data sets of DW110118-1 device 2 at room temperature and in liquid nitrogen (Fig. 5.11), plotted on the same scale. The switching amplitude in liquid nitrogen depends much less on time and current than at room temperature.

The first important step is to make sure that the conductivity change is homogeneous over the measured area. Otherwise it is not reliably possible to relate measured conductance with conductivity. Fortunately, the conductivity change is associated with a change of optical properties (Fig. 5.16). That means it is easily possible to see how the change is distributed across the junction area.

Furthermore, the samples should have uniform properties, only depending on factors that are under control. If the samples have large random variations, it is not possible to relate a difference in preparation with the measured properties.

The sample properties should scale correctly when the lateral size of the samples is changed, down to the lithographic resolution limit. This test can confirm that the effects happen in the crossover area and not on edges or defects.

Then it is necessary to determine the change in carrier density. At least as a control it would be necessary to measure the Hall effect and separate the conductivity into mobility and carrier density. There are many effects that have an influence on one or the other and it is reasonable to assume that ionic rearrangements influence the mobility (Table 2.1). It would also be extremely interesting to see if the observed drift

is caused by a change in mobility (ionic ordering) or by a change in carrier density (ionic transport). The measurements would have to be very sensitive and would only be possible if the conductance change is large enough. A material combination with strong switching amplitude would be necessary

If the change in carrier density is known, the amount of oxygen can be deduced. In a first approximation it could be assumed that one oxygen contributes two holes. But at least in LCO that is not the case and a number of 1.3 is used in a paper by Hor and Li [118]. The relation between oxygen concentration change and carrier concentration change for each electrode material would have to be found in the literature or measured.

When all these information are combined, oxygen transport as a function of time, voltage and temperature can be measured quantitatively with extremely high sensitivity.

# Chapter 7

# Conclusions and Outlook

Interesting properties of oxide heterostructures under extreme conditions can be explored with the methods presented here. The approach to detect ionic transport and dielectric relaxation processes at high field strength via the conductance change of ultra-thin semiconducting electrodes was newly developed. It gives access to low-level ionic transport and relaxation processes via simple electrical measurements that can be performed in a wide parameter and temperature range. No other method can do that, as far as I know. Quantitative measurements are theoretically possible on high-quality samples (see Section 6.11 for details).

It turned out to be quite challenging to make samples with sufficient quality. First-generation devices fabricated with shadow masks gave qualitative results, but suffered from parasitic effects. A technique to make complex heterostructures of nanometer-thick high-quality epitaxial films with lithographic methods was developed for better samples. This consumed a lot of time, and in the end there was not much time left to actually use this technology for samples beyond proof-of-concept. But the technique will hopefully find applications beyond this thesis to manufacture high-quality devices in the emerging field of oxide electronics.

The results encourage further work (see also Appendix B). It is already apparent that other mechanisms and laws than in bulk high-temperature ionic conduction rule the transport in the world of nanoionics. The devices have to be understood as semiconductor heterostructures from an electronic point of view. The results here do in principle match the theoretical expectations for this parameter range. The temperature dependence of the effect is however different from first expectations. Transport mechanisms that are apparently related to dielectric relaxation processes start to play a role. Interface effects on the ionic transport have to be considered as well. This region is still hardly explored and could perhaps give many more interesting results in the future. A better understanding of such electronic and ionic transport mechanisms can help in the development of new types of computer memory.

# Chapter 8

# Acknowledgements

I thank all my coworkers at the PGI for the pleasant and productive time that I spent there with them, as well as all the many people who – directly or indirectly – contributed to this work. I am also thankful that I could use the infrastructure of the neighboring institute PGI-7 extensively. I especially would like to thank the following people and institutions:

**Tania Claudio Weber (JCNS-2)** Review, discussion, graphics design

**René Borowski (PGI-7)** Cleanroom, RIBE, metal deposition

**Mirka Grates (PGI-7)** Cleanroom, assistance with lithography

**Paul Meuffels (PGI-7)** XRD instrument officer

**Christian Lenser and Marcel Reiners (PGI-7)** AFM instrument officers

**Yuehua Chen** Film deposition, XRD, AFM

**Yi Zeng** Film deposition, XRD, AFM

**Róza Vőfély** Film deposition, XRD, AFM, chemical etching

**Rolf Speen (PGI-5)** Technician, technical drawings, 3D artwork

**Karl-Heinz Graf (PGI-5)** Technician

**Doris Meertens (PGI-5)** SEM, FIB

**Jin Lei (PGI-5)** TEM

**Juri Barthel (PGI-5)** EELS

**Lothar Houben (PGI-5)** EELS

**Andras Kovacs (PGI-5)** Biasing TEM sample

**Michael Faley (PGI-5)** Sputtering and structuring

**Yuri Divin (PGI-5)** Sputtering and structuring

**Hans Lustfeld (PGI-1)** Discussion, ideas for measurements, theory

**Roger de Souza (IPC, RWTH Aachen)** SIMS

**Manuel Angst (PGI-4)** Communication about electronic structure

**Janet Carter-Sigglow (ZB)** Proofreading of articles

**Fabian Kiendl (R-P)** Patent applications

**Hannelore Lippert and Jennifer Bachhausen (ZEA-3)** Chemical analysis of targets

**Knut Peters, Crystec** Insights into substrate polishing and surface treatment

**Konrad Pelzer (ZEA-2)** Help with PCB production

**Ralf Schleichert (IKP-2)** Help with ceramic PCB

**Norbert Wolters, Ralph Otto (ICS-TAE)** PCB production in very short time

**Artur Glavic and Ulrich Rücker (PGI-4)** Officers for AFM with aiming camera

**Elbau GmbH** Production of ceramic PCB in very low quantity

**Joachim Maier, Giuliano Gregori, Rotraut Merkle, MPI Stuttgart** Very in-depth and fruitful discussions

**Knut Urban (PGI-5)** Critical review

**Yulia Mourzina (PGI-8/ICS-8)** Chemical etching, review and discussion

**Rafal Dunin-Borkowski (PGI-5)** Support, advice

**Ulrich Poppe (PGI-5)** Supervisor

**Rainer Waser (PGI-7)** Doctoral supervisor

# Bibliography


[1] Dieter Weber and Ulrich Poppe. Non-volatile gated variable resistor based on doped $La_2CuO_{4+\delta}$ and $SrTiO_3$ heterostructures. *Journal of Applied Physics*, 111(5):056101, 2012. DOI: 10.1063/1.3691599.

[2] Rainer Waser, Regina Dittmann, Georgi Staikov, and Kristof Szot. Redox-based resistive switching memories – nanoionic mechanisms, prospects, and challenges. *Advanced Materials*, 21(25-26):2632–2663, 2009. DOI: 10.1002/adma.200900375.

[3] Rainer Waser and Masakazu Aono. Nanoionics-based resistive switching memories. *Nature Materials*, 6(11):833–840, November 2007. DOI: 10.1038/nmat2023.

[4] Dmitri Strukov and R. Williams. Exponential ionic drift: Fast switching and low volatility of thin-film memristors. *Applied Physics A: Materials Science & Processing*, 94(3):515–519, March 2009. DOI: 10.1007/s00339-008-4975-3.

[5] ITRS. International technology roadmap for semiconductors. Technical report, ITRS, 2011. URL `http://www.itrs.net/Links/2011ITRS/Home2011.htm`.

[6] David R. Lamb. *Electrical Conduction Mechanisms in Thin Insulating Films*. Methuen and Co, 1967.

[7] R. Meyer, L. Schloss, J. Brewer, R. Lambertson, W. Kinney, J. Sanchez, and D. Rinerson. Oxide dual-layer memory element for scalable non-volatile cross-point memory technology. In *Non-Volatile Memory Technology Symposium, 2008. NVMTS 2008. 9th Annual*, pages 1 –5, 2008. DOI: 10.1109/NVMT.2008.4731194.

[8] Joachim Maier. *Festkörper – Fehler und Funktion: Prinzipien der physikalischen Festkörperchemie*. Teubner, Stuttgart, 2000.

[9] J.P Lacharme and J.O Isard. Ionic jump processes and high field conduction in glasses. *Journal of Non-Crystalline Solids*, 27(3):381 – 397, 1978. DOI: 10.1016/0022-3093(78)90021-2.

[10] M.M. Lohrengel. Thin anodic oxide layers on aluminium and other valve metals: high field regime. *Materials Science and Engineering: R: Reports*, 11(6):243 – 294, 1993. DOI: 10.1016/0927-796X(93)90005-N.

[11] M Bojinov, G Fabricius, T Laitinen, K Mäkelä, T Saario, and G Sundholm. Coupling between ionic defect structure and electronic conduction in passive films on iron, chromium and iron–chromium alloys. *Electrochimica Acta*, 45 (13):2029 – 2048, 2000. DOI: 10.1016/S0013-4686(99)00423-5.

[12] Ulrich Poppe, Dieter Weber, Yuriy Divin, and Mikhail Faley. Ionisch gesteuertes Dreitorbauelement, 2012. URL `http://worldwide.espacenet.com/publicationDetails/biblio?CC=WO&NR=2012003821A1&KC=A1&FT=D&ND=&date=20120112&DB=&locale=en_EP`.

[13] Dieter Weber, Róza Vőfély, Yuehua Chen, and Ulrich Poppe. Ätzverfahren für Metall-Mischoxide.

[14] Dieter Weber, Róza Vőfély, Yuehua Chen, Yulia Mourzina, and Ulrich Poppe. Variable resistor made by repeated steps of epitaxial deposition and lithographic structuring of oxide layers by using wet chemical etchants. *Thin Solid Films*, 2013.

[15] R. Ramesham, S. Thakoor, T. Daud, and A. P. Thakoor. Solid-state reprogrammable analog resistive devices for electronic neural networks. *Journal of the Electrochemical Society*, 137(6):1935–1939, 1990. DOI: 10.1149/1.2086834.

[16] Toshitsugu Sakamoto, Noriyuki Iguchi, and Masakazu Aono. Nonvolatile triode switch using electrochemical reaction in copper sulfide. *Applied Physics Letters*, 96(25):252104, 2010. DOI: 10.1063/1.3457861.

[17] Tsuyoshi Hasegawa, Yaomi Itoh, Hirofumi Tanaka, Takami Hino, Tohru Tsuruoka, Kazuya Terabe, Hisao Miyazaki, Kazuhito Tsukagoshi, Takuji Ogawa, Shu Yamaguchi, and Masakazu Aono. Volatile/nonvolatile dual-functional atom transistor. *Applied Physics Express*, 4(1):015204, 2011. DOI: 10.1143/APEX.4.015204.

[18] F.-Q. Xie, L. Nittler, Ch. Obermair, and Th. Schimmel. Gate-controlled atomic quantum switch. *Physical Review Letters*, 93(12):128303, Sep 2004. DOI: 10.1103/PhysRevLett.93.128303.

[19] S. Thiel, G. Hammerl, A. Schmehl, C. W. Schneider, and J. Mannhart. Tunable quasi-two-dimensional electron gases in oxide heterostructures. *Science*, 313 (5795):1942–1945, 2006. DOI: 10.1126/science.1131091.

[20] Hiromichi Ohta. Electric-field thermopower modulation in $SrTiO_3$-based field-effect transistors. *Journal of Materials Science*, pages 1–9. DOI: 10.1007/s10853-012-6856-6.

[21] Marten Armgarth, Miaoxiang Chen, David A. Nilsson, Rolf M. Berggren, Thomas Kugler, and Tommi Remonen. Electrochemical device, October 2004. URL `http://www.google.com/patents/US6806511`.

[22] Thomas Kugler. Electrochemical thin-film transistor, May 2011. URL `http://www.google.com/patents/US7952090`.

[23] David Nilsson, Thomas Kugler, Per-Olof Svensson, and Magnus Berggren. An all-organic sensor–transistor based on a novel electrochemical transducer concept printed electrochemical sensors on paper. *Sensors and Actuators B: Chemical*, 86(2–3):193 – 197, 2002. DOI: 10.1016/S0925-4005(02)00170-3.

[24] Andrew K Jonscher. Dielectric relaxation in solids. *Journal of Physics D: Applied Physics*, 32(14):R57, 1999. DOI: 10.1088/0022-3727/32/14/201.

[25] Rainer Waser, Tudor Baiatu, and Karl-Heinz Härdtl. DC electrical degradation of perovskite-type titanates: I, ceramics. *Journal of the American Ceramic Society*, 73(6):1645–1653, 1990. DOI: 10.1111/j.1151-2916.1990.tb09809.x.

[26] Rainer Waser, Tudor Baiatu, and Karl-Heinz Härdtl. DC electrical degradation of perovskite-type titanates: II, single crystals. *Journal of the American Ceramic Society*, 73(6):1654–1662, 1990. DOI: 10.1111/j.1151-2916.1990.tb09810.x.

[27] Tudor Baiatu, Rainer Waser, and Karl-Heinz Härdtl. DC electrical degradation of perovskite-type titanates: III, a model of the mechanism. *Journal of the American Ceramic Society*, 73(6):1663–1673, 1990. DOI: 10.1111/j.1151-2916.1990.tb09811.x.

[28] Mingzhen Xu and Changhua Tan. An analytical expression for predicting wearout lifetime of thin gate and tunneling oxide. *Solid-State Electronics*, 46 (1):115 – 121, 2002. DOI: 10.1016/S0038-1101(01)00266-0.

[29] X. Lu, M. Wang, and M. Wong. A two-stage degradation model of p-channel low-temperature poly-Si thin-film transistors under positive bias temperature stress. *Electron Devices, IEEE Transactions on*, 58(10):3501 –3505, October 2011. DOI: 10.1109/TED.2011.2160949.

[30] J.L. Barton. The effect of high fields on the conduction of glasses containing iron. *Journal of Non-Crystalline Solids*, 4:220 – 230, 1970. DOI: 10.1016/0022-3093(70)90044-X. International Conference on Amorphous and Liquid Semiconductors.

[31] B. Ma, U. Balachandran, J.-H. Park, and C.U. Segre. Determination of chemical diffusion coefficient of $SrFeCo_{0.5}O_x$ by the conductivity relaxation method. *Solid State Ionics*, 83(1–2):65 – 71, 1996. DOI: 10.1016/0167-2738(95)00227-8.

[32] J-C. Grenier, A. Wattiaux, N. Lagueyte, J.C. Park, E. Marquestaut, J. Etourneau, and M. Pouchard. A new superconductor obtained by electrochemical oxidation of $La_2CuO_4$. *Physica C: Superconductivity*, 173(3–4):139 – 144, 1991. DOI: 10.1016/0921-4534(91)90360-B.

[33] B. O. Wells, R. J. Birgeneau, F. C. Chou, Y. Endoh, D. C. Johnston, M. A. Kastner, Y. S. Lee, G. Shirane, J. M. Tranquada, and K. Yamada. Intercalation and staging behavior in super-oxygenated $La_2CuO_{4+\delta}$. *Zeitschrift für Physik B Condensed Matter*, 100:535–545, 1996. DOI: 10.1007/s002570050158.

[34] A. Daridon, H. Siegenthaler, F. Arrouy, E. J. Williams, E. Mächler, and J. P. Locquet. Growth and electrochemical oxidation of MBE-grown c-axis $La_2CuO_4$ thin films on different substrates. *Journal of Alloys and Compounds*, 251(1-2): 118 – 122, 1997. DOI: 10.1016/S0925-8388(96)02804-6.

[35] Frédéric Arrouy, Jean-Pierre Locquet, Erica J. Williams, Erich Mächler, Rüdiger Berger, Christopher Gerber, Christophe Monroux, Jean-Claude Grenier, and Alain Wattiaux. Growth, microstructure, and electrochemical oxidation of MBE-grown *c*-axis $La_2CuO_4$ thin films. *Phys. Rev. B*, 54:7512–7520, Sep 1996. DOI: 10.1103/PhysRevB.54.7512.

[36] M. Hücker, V. Kataev, J. Pommer, J. Harraß, A. Hosni, C. Pflitsch, R. Gross, and B. Büchner. Mobility of holes and suppression of antiferromagnetic order in $La_{2-x}Sr_xCuO_4$. *Phys. Rev. B*, 59:R725–R728, Jan 1999. DOI: 10.1103/PhysRevB.59.R725.

[37] Nicola Poccia, Michela Fratini, Alessandro Ricci, Gaetano Campi, Luisa Barba, Alessandra Vittorini-Orgeas, Ginestra Bianconi, Gabriel Aeppli, and Antonio Bianconi. Evolution and control of oxygen order in a cuprate superconductor. *Nature Materials*, advance online publication:–, August 2011. DOI: 10.1038/nmat3088.

[38] D. G. Schlom, L. Q. Chen, C. B. Eom, K. M. Rabe, S. K. Streiffer, and J. M. Triscone. Strain tuning of ferroelectric thin films. *Annual Review of Materials Research*, 37:589–626, 2007. DOI: 10.1146/annurev.matsci.37.061206.113016.

[39] Y. Tokura and N. Nagaosa. Orbital physics in transition-metal oxides. *Science*, 288(5465):462–468, 2000. DOI: 10.1126/science.288.5465.462.

[40] T.I. Selinder, U. Helmersson, Z. Han, J.-E. Sundgren, H. Sjöström, and L.R. Wallenberg. Yttrium oxide inclusions in $YBa_2Cu_3O_x$ thin films: Enhanced flux pinning and relation to copper oxide surface particles. *Physica C: Superconductivity*, 202(1–2):69 – 74, 1992. DOI: 10.1016/0921-4534(92)90297-P.

[41] Scott A. Chambers. Understanding the mechanism of conductivity at the $LaAlO_3/SrTiO_3(001)$ interface. *Surface Science*, 605(13–14):1133 – 1140, 2011. DOI: 10.1016/j.susc.2011.04.011.

[42] Q. He, C.-H. Yeh, J.-C. Yang, G. Singh-Bhalla, C.-W. Liang, P.-W. Chiu, G. Catalan, L. W. Martin, Y.-H. Chu, J. F. Scott, and R. Ramesh. Magnetotransport at domain walls in $BiFeO_3$. *Phys. Rev. Lett.*, 108:067203, Feb 2012. DOI: 10.1103/PhysRevLett.108.067203.

[43] Calvin H. W. Cheng and Mark C. Lonergan. A conjugated polymer pn junction. *Journal of the American Chemical Society*, 126(34):10536–10537, 2004. DOI: 10.1021/ja046880p.

[44] H.G.L. Coster. A quantitative analysis of the voltage-current relationships of fixed charge membranes and the associated property of "punch-through". *Biophysical Journal*, 5(5):669 – 686, 1965. DOI: 10.1016/S0006-3495(65)86745-5.

[45] J. Roqueta, M. Burriel, A. Apostolides, J. Chaigneau, and J. Santiso. Epitaxial $La_2NiO_4$ films on $SrTiO_3$ substrate: A possible oxygen diode. Presentation at the E-MRS Spring Meeting Symposium C No. 10 2, May 2012.

[46] J. Maier and G. Schwitzgebel. Conductance measurements on orthorhombic and on $TiO_2$-stabilized tetragonal lead oxide. *Materials Research Bulletin*, 17 (8):1061 – 1069, 1982. DOI: 10.1016/0025-5408(82)90133-7.

[47] J. Verbeeck, O. I. Lebedev, G. Van Tendeloo, and B. Mercey. $SrTiO_3(100)/(LaMnO_3)_m(SrMnO_3)_n$ layered heterostructures: A combined EELS and TEM study. *Phys. Rev. B*, 66:184426, Nov 2002. DOI: 10.1103/PhysRevB.66.184426.

[48] B. Förg, C. Richter, and J. Mannhart. Field-effect devices utilizing $LaAlO_3$-$SrTiO_3$ interfaces. *Applied Physics Letters*, 100(5):053506, 2012. DOI: 10.1063/1.3682102.

[49] Werner Dietsche, Benjamin Förg, Cameron Hughes, Carsten Woltmann, Thilo Kopp, Florian Loder, Jochen Mannhart, Natalia Pavlenko, Christoph Richter, Ulrike Waizmann, and Jürgen Weis. Exploration of electronic systems at oxide interfaces. In *Frontiers in Electronic Materials*, 2012.

[50] Inorganic crystal structure database (ICSD) collection code 80873, . URL `http://www.fiz-karlsruhe.de/icsd.html`.

[51] Inorganic crystal structure database (ICSD) collection code 69311, . URL `http://www.fiz-karlsruhe.de/icsd.html`.

[52] Inorganic crystal structure database (ICSD) collection code 16636, . URL `http://www.fiz-karlsruhe.de/icsd.html`.

[53] T. Zhao, A. Scholl, F. Zavaliche, K. Lee, M. Barry, A. Doran, M. P. Cruz, Y. H. Chu, C. Ederer, N. A. Spaldin, R. R. Das, D. M. Kim, S. H. Baek, C. B. Eom, and R. Ramesh. Electrical control of antiferromagnetic domains in multiferroic $BiFeO_3$ films at room temperature. *Nat Mater*, 5(10):823–829, October 2006. ISSN 1476-1122. URL `http://dx.doi.org/10.1038/nmat1731`.

[54] K. van Benthem, C. Elsasser, and R. H. French. Bulk electronic structure of $SrTiO_3$: Experiment and theory. *Journal of Applied Physics*, 90(12):6156–6164, 2001. DOI: 10.1063/1.1415766.

[55] A. Amtout and R. Leonelli. Optical properties of rutile near its fundamental band gap. *Phys. Rev. B*, 51:6842–6851, Mar 1995. DOI: 10.1103/PhysRevB.51.6842.

[56] Takayoshi Takeda and Sōji Ōhara. Magnetic structure of the cubic perovskite type $SrMnO_3$. *Journal of the Physical Society of Japan*, 37(1):275–275, 1974. DOI: 10.1143/JPSJ.37.275.

[57] M. Regulski, R. Przeniosło, I. Sosnowska, and J.-U. Hoffmann. Incommensurate magnetic structure of $\beta - MnO_2$. *Phys. Rev. B*, 68:172401, Nov 2003. DOI: 10.1103/PhysRevB.68.172401.

[58] J. M. Ginder, M. G. Roe, Y. Song, R. P. McCall, J. R. Gaines, E. Ehrenfreund, and A. J. Epstein. Photoexcitations in $La_2CuO_4$: 2-eV energy gap and long-lived defect states. *Phys. Rev. B*, 37:7506–7509, May 1988. DOI: 10.1103/PhysRevB.37.7506.

[59] J. Ghijsen, L. H. Tjeng, J. van Elp, H. Eskes, J. Westerink, G. A. Sawatzky, and M. T. Czyzyk. Electronic structure of $Cu_2O$ and CuO. *Phys. Rev. B*, 38: 11322–11330, Dec 1988. DOI: 10.1103/PhysRevB.38.11322.

[60] F. P. Koffyberg and F. A. Benko. A photoelectrochemical determination of the position of the conduction and valence band edges of p-type CuO. *Journal of Applied Physics*, 53(2):1173–1177, 1982. DOI: 10.1063/1.330567.

[61] Stephen J. Skinner and John A. Kilner. Oxygen ion conductors. *Materials Today*, 6(3):30 – 37, 2003. DOI: 10.1016/S1369-7021(03)00332-8.

[62] J. A. Hirschfeld and H. Lustfeld. First-principles study and modeling of strain-dependent ionic migration in $ZrO_2$. *Phys. Rev. B*, 84:224308, Dec 2011. DOI: 10.1103/PhysRevB.84.224308.

[63] O. Yamamoto, Y. Arachi, H. Sakai, Y. Takeda, N. Imanishi, Y. Mizutani, M. Kawai, and Y. Nakamura. Zirconia based oxide ion conductors for solid oxide fuel cells. *Ionics*, 4:403–408, 1998. ISSN 0947-7047. DOI: 10.1007/BF02375884.

[64] A.E. Paladino, L.G. Rubin, and J.S. Waugh. Oxygen ion diffusion in single crystal $SrTiO_3$. *Journal of Physics and Chemistry of Solids*, 26(2):391 – 397, 1965. ISSN 0022-3697. DOI: 10.1016/0022-3697(65)90168-X.

[65] Krzysztof Szot, Wolfgang Speier, Gustav Bihlmayer, and Rainer Waser. Switching the electrical resistance of individual dislocations in single-crystalline $SrTiO_3$. *Nature Materials*, 5(4):312–320, April 2006. DOI: 10.1038/nmat1614.

[66] Makoto Aoki, Yet-Ming Chiang, Igor Kosacki, L. Jong-Ren Lee, Harry Tuller, and Yaping Liu. Solute segregation and grain-boundary impedance in high-purity stabilized zirconia. *Journal of the American Ceramic Society*, 79(5): 1169–1180, 1996. ISSN 1551-2916. DOI: 10.1111/j.1151-2916.1996.tb08569.x. URL `http://dx.doi.org/10.1111/j.1151-2916.1996.tb08569.x`.

[67] Joachim Maier. Defect chemistry and ionic conductivity in thin films. *Solid State Ionics*, 23(1–2):59 – 67, 1987. ISSN 0167-2738. DOI: 10.1016/0167-2738(87)90082-8.

[68] M. I. Faley, U. Poppe, H. Soltner, C. L. Jia, M. Siegel, and K. Urban. Josephson junctions, interconnects, and crossovers on chemically etched edges of $YBa_2Cu_3O_{7-x}$. *Applied Physics Letters*, 63(15):2138–2140, 1993. DOI: 10.1063/1.110565.

[69] C. L. Jia, M. I. Faley, U. Poppe, and K. Urban. Effect of chemical and ion-beam etching on the atomic structure of interfaces in $YBa_2Cu_3O_7/PrBa_2Cu_3O_7$ Josephson junctions. *Applied Physics Letters*, 67(24):3635–3637, 1995. DOI: 10.1063/1.115342.

[70] Paul T. Bowman, Edmond I. Ko, and Paul J. Sides. A potential hazard in preparing bromine-methanol solutions. *Journal of the Electrochemical Society*, 137(4):1309–1311, 1990. DOI: 10.1149/1.2086655.

[71] Nils Wiberg, Egon Wiberg, and Arnold Frederik Holleman. *Lehrbuch der anorganischen Chemie*. DeGruyter, Berlin, 101st edition, 1995.

[72] F. S. Goucher, G. L. Pearson, M. Sparks, G. K. Teal, and W. Shockley. Theory and experiment for a germanium p-n junction. *Phys. Rev.*, 81:637–638, Feb 1951. DOI: 10.1103/PhysRev.81.637.2.

[73] John O. M. Bockris and Amulya K. N. Reddy. *Modern electrochemistry. Fundamentals of electrodics*. Modern electrochemistry ; 2A. Kluwer Academic /Plenum Publ., New York, NY, 2nd edition, 2000.

[74] Allen J. Bard and Larry R. Faulkner. *Electrochemical methods: fundamentals and applications*. Wiley, New York, NY, 2nd edition, 2001.

[75] Laura M. Grupp, John D. Davis, and Steven Swanson. The bleak future of NAND Flash memory. In *Proceedings of the 10th USENIX conference on file and storage technologies*, 2012. URL `http://cseweb.ucsd.edu/users/swanson/papers/FAST2012BleakFlash.pdf`.

[76] Shin Hwa Li. *Chemical mechanical polishing in silicon processing*. Semiconductors and semimetals ; 63. Academic Press, New York, NY, 2000.

[77] S. Wicklein, A. Sambri, S. Amoruso, X. Wang, R. Bruzzese, A. Koehl, and R. Dittmann. Pulsed laser ablation of complex oxides: The role of congruent ablation and preferential scattering for the film stoichiometry. *Applied Physics Letters*, 101(13):131601, 2012. DOI: 10.1063/1.4754112.

[78] W. Ramadan, S. B. Ogale, S. Dhar, S. X. Zhang, D. C. Kundaliya, I. Satoh, and T. Venkatesan. Substrate-induced strain effects on the transport properties of pulsed laser-deposited Nb-doped $SrTiO_3$ films. *Applied Physics Letters*, 88 (14):142903, 2006. DOI: 10.1063/1.2187439.

[79] Ulrich Poppe, Jürgen Schubert, and Wilhelm Evers. Verfahren zur Herstellung dünner Schichten aus oxydischem Hochtemperatur-Supraleiter, 1993. URL `http://worldwide.espacenet.com/publicationDetails/biblio?CC=EP&NR=0328757B1&KC=B1&FT=D&ND=1&date=19930428&DB=&locale=en_EP`.

[80] Knut Urban, Ulrich Poppe, and Karsten Tillmann. Field effect transistor based on channel doping by electric-field driven oxygen intercalation "Ionic FET". Proposal for doctoral thesis.

[81] Vladislav V. Kharton, Alexandre Viskup P., Eugene Naumovich N., and Fernando M. B. Marques. Oxygen ion transport in $La_2NiO_4$-based ceramics. *Journal of Materials Chemistry*, 9(10):2623–2629, 1999. DOI: 10.1039/A903276B.

[82] M. L. Wilson, J. M. Byers, P. C. Dorsey, J. S. Horwitz, D. B. Chrisey, and M. S. Osofsky. Effects of defects on magnetoresistivity in $La_{0.7}Sr_{0.3}MnO_3$. *Journal of Applied Physics*, 81(8):4971–4973, 1997. DOI: 10.1063/1.365016.

[83] Qiang Li, Hui Zhao, Lihua Huo, Liping Sun, Xiaoli Cheng, and Jean-Claude Grenier. Electrode properties of Sr doped $La_2CuO_4$ as new cathode material for intermediate-temperature SOFCs. *Electrochemistry Communications*, 9(7): 1508 – 1512, 2007. DOI: 10.1016/j.elecom.2007.02.013.

[84] Markus Vollman and Rainer Waser. Grain boundary defect chemistry of acceptor-doped titanates: Space charge layer width. *Journal of the American Ceramic Society*, 77(1):235–243, 1994. DOI: 10.1111/j.1151-2916.1994.tb06983.x.

[85] Markus Vollmann, Rainer Hagenbeck, and Rainer Waser. Grain-boundary defect chemistry of acceptor-doped titanates: Inversion layer and low-field conduction. *Journal of the American Ceramic Society*, 80(9):2301–2314, 1997. DOI: 10.1111/j.1151-2916.1997.tb03121.x.

[86] Jonas Hink and Erik Jansen. Titanium in a hyperbaric oxygen environment may pose a fire risk., 2003. URL `http://www.biomedsearch.com/nih/Titanium-in-hyperbaric-oxygen-environment/14692477.html`.

[87] M. Biasotti, L. Pellegrino, E. Bellingeri, C. Bernini, A.S. Siri, and D. Marrè. All-oxide crystalline microelectromechanical systems. *Procedia Chemistry*, 1 (1):839 – 842, 2009. DOI: 10.1016/j.proche.2009.07.209. Proceedings of the Eurosensors XXIII conference.

[88] Marcel Pourbaix. *Atlas of electrochemical equilibria in aqueous solutions*. National Association of Corrosion Engineers,, Houston, Tex., 2nd english edition, 1974.

[89] Ignasi Puigdomenech. Chemical equilibrium diagrams, 2010. URL `http://www.kemi.kth.se/medusa/`.

[90] Hiroshi Tomita and Soichi Nadahara. Etching method and etching apparatus method for manufacturing semiconductor device and semiconductor device, Aug 2002. URL `www.google.com/patents/US6436723`.

[91] K. Hieda, K. Eguchi, J. Nakahira, M. Kiyotoshi, M. Nakabayashi, H. Tomita, M. Izuha, T. Aoyama, S. Niwa, K. Tsunoda, S. Yamazaki, J. Lin, A. Shimada, K. Nakamura, T. Kubota, M. Asano, K. Hosaka, Y. Fukuzumi, Y. Ishibashi, and Y. Kohyama. Low temperature $(Ba, Sr)TiO_3$ capacitor process integration (LTB) technology for gigabit scaled DRAMs. In *Electron Devices Meeting, 1999. IEDM '99. Technical Digest. International*, pages 789 –792, 1999. DOI: 10.1109/IEDM.1999.824268.

[92] W.P. Griffith. *Ruthenium Oxidation Complexes: Their Uses as Homogenous Organic Catalysts*. Catalysis by Metal Complexes. Springer, 2010. ISBN 9781402093760. URL `http://books.google.co.uk/books?id=ybUU8yBy5mAC`. pp. 11.

[93] R. M. Stroud, J. Kim, C. R. Eddy, D. B. Chrisey, J. S. Horwitz, D. Koller, M. S. Osofsky, Jr. R. J. Soulen, and R. C. Y. Auyeung. Fabrication of $YBa_2Cu_3O_{7-\delta}/SrTiO_3/La_{0.7}Sr_{0.3}MnO_{3-\delta}$ junctions for the control of supercurrent by spin-polarized quasiparticle current injection. *Journal of Applied Physics*, 83(11):7189–7191, 1998. DOI: 10.1063/1.367676.

[94] Sang-Suk Lee and Do-Guwn Hwang. Magnetoresistive $La_{0.8}Sr_{0.2}MnO_{3-\delta}$ biepitaxial films grown on $Al_2O_3$ (1120) substrates. *Journal of the Korean Physical Society*, 37(3):283–286, Sep 2000. URL `http://www.kps.or.kr/jkps/abstract_view.asp?articleuid=8803F186-AFBF-4AC3-988C-7E3F65D7C343`.

[95] Joo-Hyung Kim, Alexander M. Grishin, and Velislava Angelova Ignatova. Wet etching study of $La_{0.67}(Sr_{0.5}Ca_{0.5})_{0.33}MnO_3$ films on silicon substrates. *Journal of Electronic Materials*, 37:361–367, 2008. DOI: 10.1007/s11664-007-0343-x.

[96] R. Rajagopal, S.N. Kale, N.A. Raorane, R. Pinto, and V.R. Rao. Fabrication of $La_{0.7}Sr_{0.3}MnO_3$-Si heterojunctions using a CMOS-compatible citric acid etch process. *Electron Device Letters, IEEE*, 32(3):402 –404, march 2011. DOI: 10.1109/LED.2010.2102331.

[97] Python programming language – official website. URL `http://www.python.org/`.

[98] What is free software? URL `http://www.fsf.org/resources/resources/what-is-fs`.

[99] Scientific tools for Python. URL `http://www.scipy.org/`.

[100] Matplotlib: Python plotting. URL `http://matplotlib.sourceforge.net/`.

[101] LabVIEW system design software. URL `http://www.ni.com/labview/`.

[102] Apache Subversion. URL `http://subversion.apache.org/`.

[103] wxPython. URL `http://www.wxpython.org/what.php`.

[104] R. Hojczyk. *Untersuchung von oxidischen Isolationsmaterialien in heteroepitaktischen Bauelementen auf der Basis von Hochtemperatursupraleitern*. PhD thesis, RWTH Aachen, 1999.

[105] Takeaki Yajima, Yasuyuki Hikita, and Harold Y. Hwang. A heteroepitaxial perovskite metal-base transistor. *Nature Materials*, 10(3):198–201, Jan. 2011. DOI: 10.1038/nmat2946.

[106] R. H. Fowler and L. Nordheim. Electron emission in intense electric fields. *Proceedings of the Royal Society of London. Series A*, 119(781):173–181, 1928. DOI: 10.1098/rspa.1928.0091.

[107] John G. Simmons. Poole-Frenkel effect and Schottky effect in metal-insulator-metal systems. *Phys. Rev.*, 155:657–660, Mar 1967. DOI: 10.1103/PhysRev.155.657.

[108] Peter Mark and Thomas E. Hartman. On distinguishing between the Schottky and Poole-Frenkel effects in insulators. *Journal of Applied Physics*, 39(4): 2163–2164, 1968. DOI: 10.1063/1.1656519.

[109] Yasuyuki Hikita, Mitsuru Nishikawa, Takeaki Yajima, and Harold Y. Hwang. Termination control of the interface dipole in $La_{0.7}Sr_{0.3}MnO_3$/Nb:$SrTiO_3$ (001) Schottky junctions. *Phys. Rev. B*, 79(7):073101, Feb. 2009. DOI: 10.1103/PhysRevB.79.073101.

[110] A. K. Jonscher. The 'universal' dielectric response. *Nature*, 267(5613):673–679, June 1977. DOI: 10.1038/267673a0.

[111] J. Garcia-Barriocanal, A. Rivera-Calzada, M. Varela, Z. Sefrioui, E. Iborra, C. Leon, S. J. Pennycook, and J. Santamaria. Colossal ionic conductivity at interfaces of epitaxial $ZrO_2$:$Y_2O_3$/$SrTiO_3$ heterostructures. *Science*, 321(5889): 676–680, 2008. DOI: 10.1126/science.1156393. (The claims of this paper are challenged [119, 120]).

[112] Rainer Waser. *Nanoelectronics and information technology: Advanced electronic materials and novel devices*. Wiley, Berlin, 2nd, corr. edition, 2005.

[113] A. Urushibara, Y. Moritomo, T. Arima, A. Asamitsu, G. Kido, and Y. Tokura. Insulator-metal transition and giant magnetoresistance in $La_{1-x}Sr_xMnO_3$. *Phys. Rev. B*, 51:14103–14109, May 1995. DOI: 10.1103/PhysRevB.51.14103.

[114] Hiroyuki Fujishiro, Manabu Ikebe, and Yoshiyuki Konno. Phase transition to antiferromagnetic state in $La_{1-x}Sr_xMnO_3$ ($x \geq 0.5$). *Journal of the Physical Society of Japan*, 67(5):1799–1800, 1998. DOI: 10.1143/JPSJ.67.1799.

[115] G. Gonzalez de la Cruz and Yu. G. Gurevich. Carrier heating and electron-phonon energy exchange effects on nonlinear transport phenomena in semiconductor films. *Journal of Applied Physics*, 113(2):023504, 2013. DOI: 10.1063/1.4773345.

[116] Junwoo Son, Pouya Moetakef, Bharat Jalan, Oliver Bierwagen, Nicholas J. Wright, Roman Engel-Herbert, and Susanne Stemmer. Epitaxial $SrTiO_3$ films with electron mobilities exceeding $30,000\,cm^2V^{-1}s^{-1}$. *Nature Materials*, 9(6): 482–484, June 2010. DOI: 10.1038/nmat2750.

[117] J. H. Haeni, P. Irvin, W. Chang, R. Uecker, P. Reiche, Y. L. Li, S. Choudhury, W. Tian, M. E. Hawley, B. Craigo, A. K. Tagantsev, X. Q. Pan, S. K. Streiffer, L. Q. Chen, S. W. Kirchoefer, J. Levy, and D. G. Schlom. Room-temperature ferroelectricity in strained $SrTiO_3$. *Nature*, 430(7001):758–761, August 2004. DOI: 10.1038/nature02773.

[118] Pei-Herng Hor and Zugang Li. A study of the 15 K superconducting transition in $La_2CuO_{4+\delta}$. *Physica C: Superconductivity*, 341–348, Part 3(0):1585 – 1586, 2000. DOI: 10.1016/S0921-4534(00)01432-5.

[119] Matthias Gerstl, Gernot Friedbacher, Frank Kubel, Herbert Hutter, and Jurgen Fleig. The relevance of interfaces for oxide ion transport in yttria stabilized zirconia (YSZ) thin films. *Physical Chemistry Chemical Physics*, 15:1097–1107, 2013. DOI: 10.1039/C2CP42347B.

[120] Xin Guo. Can we achieve significantly higher ionic conductivity in nanostructured zirconia? *Scripta Materialia*, 65(2):96 – 101, 2011. DOI: 10.1016/j.scriptamat.2010.09.019.

[121] Introducing JSON. URL `http://www.json.org/`.

# Curriculum vitae

**Family name, given name** Weber, Dieter

**Born** 13.08.1983 in Preetz, Holstein

**Citizenship** German

**2009–2013** PhD student at the Jülich Research Centre, Peter Grünberg Institute PGI-5

**2009** Graduation as Diplom-Ingenieur

**2004–2009** Student for Materials Science and Engineering at the Christian Albrechts University Kiel

**2003** Abitur at the Max-Planck-Schule in Kiel

# Appendix A

# Software Description

The software and all measurement data are included in digital form or are available on request from the author (`mailto:d.weber@materials-scientist.com`).

## A.1 Data structure

The data is stored in a directory structure with defined format. Metadata and measurements are stored in XML files with a custom schema. While I developed the program I came to the conclusion that JSON [121] would have been a better choice, because it is easier to transform JSON data into native Python data structures. Both XML and JSON are text-based, human-readable and machine-readable, and supported in a large number of programming languages.

XML parsing can be cumbersome because XML is more complex and does not quite fit with the way how structured data is handled in Python and many other programming languages. The final data structure that emerged is now a mixture of XML elements and XML attributes that contain JSON data, which is not ideal from a design point of view, but fulfills all requirements.

The measurements are stored in a hierarchical tree of sample, sequence (corresponding to one program run), test (corresponding to a specific test routine), and step (corresponding to a measurement). Each sequence, test, and step is identified by a cycle number that is automatically incremented to avoid collisions. A short human-readable name is included in each filename so that a human can find specific data when browsing the directory manually.

Each entry has a timestamp with microsecond resolution in a human-readable format, including the timezone to make the timestamp unambiguous. The program uses UNIX timestamps internally, but this format is hard to read for humans. The MKS system of units and the common letters for physical quantities are used for all data. All available data, including instrument settings, the status of the switch, and the Subversion revision number of the software, are saved with each measurement.

This directory and file structure is kept in a Subversion repository. New data is added and committed to the repository after each measurement run. All changes are then clearly documented and can be undone at any time. The data can furthermore be synchronized between the central repository and several different machines, like different measurement computers or a workstation to process the data. Data from

different samples can be merged into the repository and eventual collisions are automatically detected by Subversion.

## A.2 Layout of the measurement software

The main executable "measure" parses the command line, passes these information to TestSequence and then hands over control to TestSequcence. The command line options are documented in "measure" and are available through "`measure --help`".

The configuration file "`~/.measure`" contains basic information, like the default location of the repository, and the mapping of switch channels to named device parts for several possible configurations. Internally, the program uses only these names to switch to specific parts of the device, like gate, channel or dielectric. This improves clarity and avoids typos in the channel numbers. The code can furthermore run on different setups with different cabling without being modified, and changes in the cabling are easily accommodated.

TestElement.py handles generic aspects of the data repository and its structure. It defines the parent class of TestSequence and all Tests and Steps where specific test routines and measurements are implemented. TestSequence.py is the root element of the current measurement run and sets up the environment for the measurement. A test script determines which tests are to be run. It is itself a Python script and it is executed in a specific environment that is provided by TestSequence. It is designed to be adapted for each measurement run. A few common script templates emerged over time. A copy of the used script is automatically included with the measurement data.

The hardware drivers kinterfaces.py, k6221.py, k7001.py and k195.py are at the lowest abstraction level. The devices are connected to the measurement computer through ethernet (current source), with a serial cable to the current source as intermediate (nanovoltmeter), or via GPIB (switch, multimeter). Source, voltmeter and switch have a line-based interface based on SCPI. This is rather easy to program. The multimeter has a character- and byte-based interface that is a bit more difficult. The drivers make the functionality of the devices available with a function call interface and perform input, output and error checking. The drivers are not complete because functions were implemented as needed. A few functions were implemented, but never used and are therefore to be regarded as untested. All program activity, including the raw commands sent to the devices, are logged in a file.

## A.3 Layout of the data processing software

Fig. A.1 shows a screenshot. Internally, the software is split into three components: a GUI framework that allows to browse and select data; a series of classes that parse the data in the repository and processes them numerically, independent of display; and a series of report classes that take the numerical data, do some postprocessing and plot them on the screen. This separation makes it relatively easy to include a new way to process and display the data, or a new type of measurement.

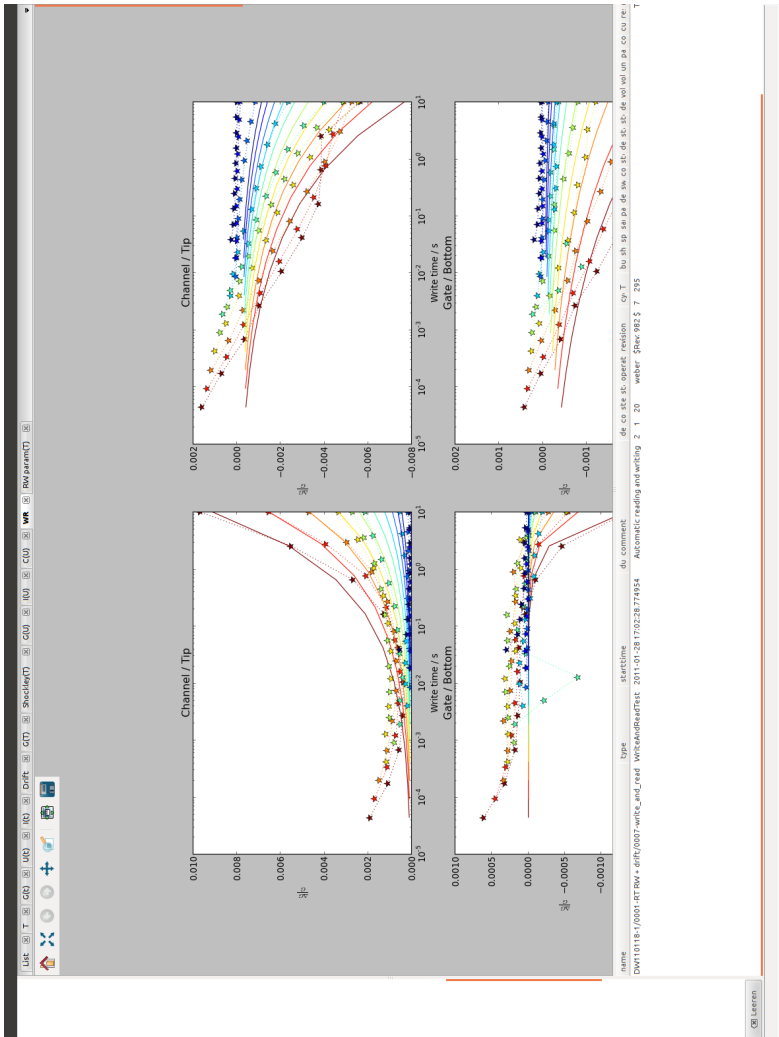


Figure A.1: Screenshot of the data processing software with exemplary report on a write and read experiment (compare Section 5.4).

# Appendix B

# Failures, Planned Experiments and Future Challenges

## B.1 Attempts on reaching a steady state

Hans Lustfeld suggested to bring the sample to a steady state where the writing current just balances the drift back. This would make it easier to model the behavior of the device, because it would eliminate the time variable. The sample changes conductance very slowly, especially at low voltage. The applied voltage should stay below one volt to not exceed the stability window of the involved materials. Only at such low voltages can the sample be thermodynamically stable, just like any electrochemical cell. It would be impractical to apply a constant current resp. keep the sample at constant voltage and wait until a steady state is reached.

As it is not possible to measure the channel conductance while a write current is flowing with the given setup, it was attempted to first measure the channel conductance in short intervals and stabilize the sample with relatively short pulses. Then the pulse length and measurement intervals should slowly increase, until the conductance would be stable over long pulse times with a nearly constantly applied write current.

These attempts failed. The sample could be stabilized with short pulses, but the conductance would start to diverge when the pulse length was increased. A significant effort was made to develop control algorithms that would adapt the write current and intervals, but inevitably they would spin out of control. Either they would "overrreact" and apply too strong currents that lead to wildly changing, oscillating conductance values, or they would not converge because the sample drifts faster than it is changed back. The writing and drifting behavior is apparently highly nonlinear and combines very slow dynamics on the scale of hours and days with very fast dynamics in time scales that are shorter than the switching time so that the sample already drifted back significantly before any measurement could be made.

## B.2 Failed samples with insufficient insulation

Samples with $BaTbO_3$ dielectric and others with YBCO electrodes were manufactured, but the dielectric was not insulating enough to be measured. Experiments with other

electrodes and dielectrics were postponed in favor of work towards lithographically defined samples.

## B.3 Secondary ion mass spectroscopy with $^{18}O$ tracer

Naturally, oxygen consists mainly of the lighter isotope $^{16}O$ with a content of only 0.2 % $^{18}O$. The transport of oxygen in a sample can be traced when part of the oxygen is enriched with the isotope $^{18}O$. The different isotopes are easy to separate with mass spectroscopy and can be detected with lateral and depth resolution using secondary ion mass spectroscopy (SIMS).

Unfortunately, $^{18}O$ is expensive. That means experiments have to be well-planned and can only consume very small amounts. Sputter deposition in an $^{18}O$ atmosphere is for this reason out of the question. Instead, it was attempted to load the channel layer after deposition with the isotope in a small plasma chamber. The channel was after that passivated with amorphous STO sputtered at low temperature instead of epitaxial STO, because the oxygen would be distributed and exchanged with the environment upon heating.

The samples behaved differently from unloaded ones: The channel conductance didn't increase, but decreased during positive pulses, and vice versa.

SIMS analysis revealed that they had inadvertently been loaded with fluorine. Previous experiments with $SF_6$ in the plasma chamber are a likely fluorine source.

The experiments were therefore not continued: There was no proven protocol for loading, the plasma chamber was not an option due to contamination, only a limited amount of the isotope was available, the samples were altered during the loading process, the sample analysis is destructive, and the small observed conductance change implies that there is not much transport to be observed in any case. The method is in principle promising to detect low-level oxygen transport, because it can in some circumstances single out rather small amounts of oxygen if they are transported across a sufficient distance. Unfortunately, there were not enough time and resources to follow up on that. In my opinion, it would amount to another PhD project.

## B.4 EELS to detect oxygen stoichiometry change

Lothar Houben and Juri Barthel tried to detect differences in the oxygen stoichiometry with EELS between lamellae from two devices on one samples that were written into opposite directions. This was not successful. If there is any change, it is very weak. The influences from sample preparation are probably too large. Reversible in-situ observation might improve this, because the exact same sample region can be observed and maybe a clear correlation with the polarity of write pulses can be established. Work in this direction was started, but not continued because a suitable sample holder could not be procured in time (see Appendix B.10).

## B.5 Higher and lower temperature

The measurement setup could be immersed in a dewar, but the temperature could only be stabilized at the boiling point of nitrogen. Measurements in a physical property measurement system that can stabilize any temperature between roughly 4 K and 400 K would allow to explore the influence of temperature much better. Measurements at higher temperature up to about 900 K would allow to make a connection with the well-characterized region for solid oxide fuel cells. I started to develop a setup for this, but then focused on the lithographic structuring.

The equations for ionic and also electronic transport contain temperature terms. By analyzing the influence of temperature on the different properties, it would be possible to learn more about the values of certain factors in these equations.

## B.6 Influence of atmosphere and water

Many oxides are permeable for protons. An $OH^-$ group occupies the place of an oxygen anions ($O^{2-}$) in that case and the attached proton then jumps from oxygen to oxygen. An oxide with oxygen vacancies can be hydrated, i.e. take up water via $H_2O + O^{2-} \longrightarrow 2\,OH^-$.

The samples were measured and stored in air. That means they could perhaps take up water from the ambient through the thin STO passivation layer. There might also be an electric field between the channel and the outer sample surface that could help to transport protons. To exclude such effects, the samples should be dried with an annealing step in vacuum and then measured in a dry atmosphere or in vacuum. This would have been possible with the high-temperature setup.

## B.7 Material combinations

Different materials were considered for experiments:

**Channel** Weakly Sr-doped LCO, $SrFeO_3$, $La_2NiO_4$, doped STO, YBCO

**Gate** $SrFeO_3$, doped STO

**Dielectric** LSGM, doped STO, YSZ, doped $BiFeO_3$

The superconducting properties of cuprates like YBCO and LCO depend on the oxygen content. It might therefore be possible to change the superconducting properties of such a channel.

A thick layer of a good ionic conductor could be combined with a thin blocking layer. The thick ionic conductor would help to suppress the electronic current, while an extremely high electrical field strength can be achieved across the thin blocking layer. The situation would then be similar to the anodization of aluminum, where the electronic current is blocked by the electrolyte. The gate electrode could also be replaced with a liquid electrolyte, such as an ionic liquid. STO field effect devices with a solid electrolyte gate have been demonstrated already [20].

## B.8 Canted layered structures

LCO, the channel material that has worked best so far, is a layered structure. Ionic and electronic transport parallel to the layers is much faster than out-of-plane transport. Therefore it was intended to grow the devices in inclined substrates so that a component of the electrical field is parallel to the planes. This could enhance the transport speed.

## B.9 Carrier density versus carrier mobility

In order to obtain quantitative results and to exclude effects from ordering processes in the LCO electrodes, the change in carrier density and the change in carrier mobility have to be measured separately. This is possible with a combination of conductivity and Hall effect measurements. A sample structure for this has already been designed (Fig. 3.8). These experiments were also planned for a physical property measurement system, because it incorporates a strong electromagnet for the Hall effect measurements.

## B.10 TEM study on internal potentials of oxide junctions

It was attempted with Andras Kovacs to image the internal potential and perhaps the ionic transport in oxide heterostructures under an applied bias voltage with electron holography. A method for sample preparation was developed, but a suitable sample holder could unfortunately not be procured in time. The change of the internal potentials under an applied bias would have given important information on the local fields within the sample. This information is necessary to model the transport on a local scale.

## B.11 Ellipsometry

Changes were visible under an optical microscope. With imaging or scanning ellipsometry it could be possible to quantify these changes and to assign them to a specific layer. A multispectral ellipsometer with good lateral resolution would be necessary for this.

With ellipsometry in the far infrared region it is possible to measure the properties of free charge carriers in semiconductors. This might be an interesting alternative to electrical measurements, because an ellipsometer can perhaps resolve the conductivity change laterally and vertically within a layer.

## B.12 Defects versus bulk

It is up to now not clear if the ionic transport occurs in the bulk, at defects, or both. The optical micrographs of changing samples (Fig. 5.16) appear smooth, but the

resolution is very low with respect to the defect density. Transport along defects versus bulk transport is an important issue for the nanoionics community [65].

Once samples with reproducible properties can be made, it should be analyzed how the sample properties scale relative to size. This can exclude edge effects. The statistical distribution of sample properties at various sizes can give information on defect densities. A lot of different devices on one sample have to be made and measured for this purpose.

One could try to introduce defects on purpose in samples with a low and controlled "natural" defect density in order to investigate their influence. The distribution of defects and property changes can perhaps be investigated with local current AFM.

## B.13 Ultra-fast dynamics

It seems that parts of the sample response are very fast, especially at higher voltage. At elevated temperature, one can expect that the samples drift back so quickly after an excitation that the changes cannot be measured with the switching setup. The conductance change of the channel would have to be measured during the write pulse. One could then measure the "normal" field effect as well. Such simultaneous measurements could use lock-in techniques in order to avoid an influence of the strong writing current on the low-level conductance measurements.

Band / Volume 19
**Flächenkontakte zu molekularen Schichten in der Bioelektronik**
N. Sanetra (2012), XIII, 129 pp
ISBN: 978-3-89336-776-4

Band / Volume 20
**Stacked device structures for resistive memory and logic**
R. D. Rosezin (2012), 137 pp
ISBN: 978-3-89336-777-1

Band / Volume 21
**Optical and electrical addressing in molecule-based logic circuits**
M. Manheller (2012), XIV, 183 pp
ISBN: 978-3-89336-810-5

Band / Volume 22
**Fabrication of Nanogaps and Investigation of Molecular Junctions by Electrochemical Methods**
Z. Yi (2012), 132 pp
ISBN: 978-3-89336-812-9

Band / Volume 23
**Thermal Diffusion in binary Surfactant Systems and Microemulsions**
B. Arlt (2012), 159, xlvi pp
ISBN: 978-3-89336-819-8

Band / Volume 24
**Ultrathin Gold Nanowires - Chemistry, Electrical Characterization and Application to Sense Cellular Biology**
A. Kisner (2012), 176 pp
ISBN: 978-3-89336-824-2

Band / Volume 25
**Interaction between Redox-Based Resistive Switching Mechanisms**
C. R. Hermes (2012), iii, 134 pp
ISBN: 978-3-89336-838-9

Band / Volume 26
**Supported lipid bilayer as a biomimetic platform for neuronal cell culture**
D. Afanasenkau (2013), xiv, 132 pp
ISBN: 978-3-89336-863-1

Band / Volume 27
**15th European Workshop on Metalorganic Vapour Phase Epitaxy (EWMOVPE XV) June 2-5, 2013, Aachen, Germany**
A. Winden (Chair) (2013)
ISBN: 978-3-89336-870-9

Band / Volume 28
**Characterization, integration and reliability of $HfO_2$ and $LaLuO_3$ high-κ/metal gate stacks for CMOS applications**
A. Nichau (2013), xi, 177 pp
ISBN: 978-3-89336-898-3

Band / Volume 29
**The role of defects at functional interfaces between polar and non-polar perovskite oxides**
F. Gunkel (2013), X, 162 pp
ISBN: 978-3-89336-902-7

Band / Volume 30
**Parallelisation potential of image segmentation in hierarchical island structures on hardware-accelerated platforms in real-time applications**
S. Suslov (2013), xiv, 211 pp
ISBN: 978-3-89336-914-0

Band / Volume 31
**Carrier mobility in advanced channel materials using alternative gate dielectrics**
E. Durğun Özben (2014), 111 pp
ISBN: 978-3-89336-941-6

Band / Volume 32
**Electrical characterization of manganite and titanate heterostructures**
A. Herpers (2014), ix, 165 pp
ISBN: 978-3-89336-948-5

Band / Volume 33
**Oxygen transport in thin oxide films at high field strength**
D. Weber (2014), XII, 115 pp
ISBN: 978-3-89336-950-8

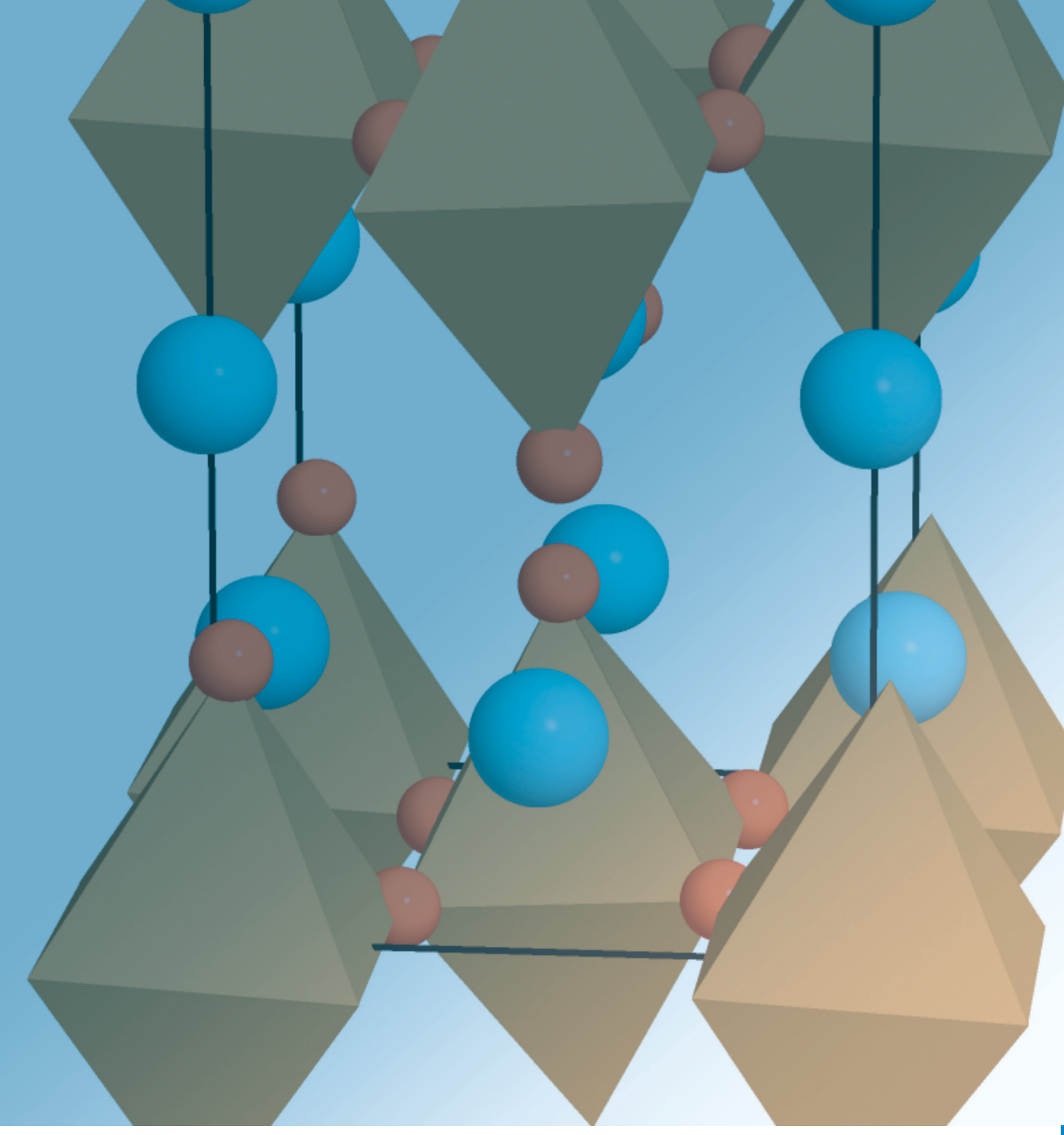

Information / Information
Band / Volume 33
ISBN 978-3-89336-950-8

JÜLICH
FORSCHUNGSZENTRUM